Author's response

We would like to thank all the reviewers for their comments, which we have responded to and made appropriate changes in the manuscript.

Below can be found a combined response to all the reviewers (identical to the response to each individual reviewer), followed by the tracked changes made in the manuscript.

The main changes to the manuscript are:

- More thorough explanations of data processing and error handling, including choices relating to sizing metrics for different instruments, which certain choices were made, and what impact this has on the uncertainty to the final size distribution.
- All errors in Figure and Table number cross-references have been corrected.
- Shorter sentences to improve clarity where possible, and clearer explanations regarding the dependence of SSA on imaginary part of the refractive index and/or effective diameter.
- More comparisons against existing literature and observations.
- Better explanations of the flight maneouvers used in the 'Flight Patterns' section and consistent terminology throughout the manuscript.
- Addition of Section 2.6 'Calculation of Optical Properties' for better explanation of the methodology.
- Addition of an appendix for instrument acronyms.
- Figure 14 now has a second panel included with data for the FULL PSD.

Response to Reviewers

K. Kandler (Referee #1)

The manuscript describes airborne measurements of mineral dust size distributions close to the source. Representation of aerosol size distributions inside atmospheric transport models is still based on many assumptions, and new data for evaluations and input is highly welcome. The manuscript adds new data for the region close to the source at the beginning of the trans-oceanic transport. It also adds additional evidence to the importance of studying particles larger than 10 m, which are frequently omitted in aerosol research, and which are difficult to study. Furthermore, optical properties for the dust aerosol are reported, which can also serve the community, e.g., as model input or for remote sensing interpretation. The authors show that variation in physical as well as compositional parameters can have a considerable impact on the optical properties, and that in their samples, the compositional variation is dominating the variation in single scattering albedo.

The topic is suitable for ACP. The paper is well-written and clearly structured. References are mostly made where appropriate, some additional comparison with previous work would enhance the general significance. Some issues - particular on the error handling - should be addressed and questions answered before publication.

We would like to thank Konrad Kandler for this detailed review and comments which we hope have led to an improved, clearer paper. We have added information regarding the different sizing metrics used, additional explanations of error handling, and expanded on comparisons to previous work, all of which are detailed below. We apologize for incorrect cross-referencing of tables and figures, which have all now been corrected.

==========

Remarks and questions

P3 L32: Are really any inlet size restriction removed? Given the high speeds at which particles are collected, a minimal deviation from perfect alignment might easily introduce boundary layers and re-circulations.

It is true that variations in the airspeed and flow angle through the sample area may occur due to distortions of the airflow about the wing probe housing and arms (Korolev et al. (2013), Weigel et al. (2016), McFarquhar et al. (2017)). We do not attempt to correct for these factors, and now state so in Section 2.3.2, and mention them in the introduction.

In terms of the alignment, the canisters are set at a set vertical angle to accommodate the 'normal' angle of attack (AoA) of the aircraft. There will be up to several degrees of misalignment as the AoA changes with altitude. The average and standard deviation of the canister angles is 3.25±0.14 deg (negative is nose-down). The range of AoA is 3.5-6 degrees nose up so there will generally be a couple of degrees misalignment between the probes and the airflow assuming no aircraft perturbation of the flows. Korolev et al. (2013) show that the velocity between the arms of the CIP has an unperturbed region of approximately half the arm width. This suggests that a small misalignment (only several degrees) is unlikely to narrow this unperturbed region sufficiently to impact the size-dependent concentrations.

Measurements behind inlets will systematically omit a portion at the upper size range of the PSD, and while wing probes may be subject to various uncertainties relating to local flow distortion, they are at least able to measure the full size range of dust particles because no inlet is used. Additionally, the bigger the particle the less they are effected by flow distortion because of their larger momentum. This is the opposite of the pipe bend problem which imposes a cut size.

P6 L32: Should this diameter then considered as optical equivalent diameter? Please state.

Not in this case, since various 'types' of diameter are considered throughout the paper. However, we have added, "Hence particle sizes determined from the PCASP and CDP represent optically equivalent diameters," to section 2.3.2 where this is discussed.

P7 L10: Have experimental or theoretical approaches been used to characterize the losses?

Both – Trembath (2012) performed OPC measurements behind different inlets on the aircraft, and followed these up by theoretical calculations of pipe losses. We added "experimental and theoretical" to this sentence.

P8 L6 and Figure 2: It looks like the sizing uncertainties from the number size distribution were not propagated into the volume size distribution (e.g., the CDP point at 20µm seems to have a factor of 3 uncertainty in size, which should propagate to around a factor of 10 in volume, but a much smaller error bar is shown in the volume plot). Instead it looks like the same vertical error bars are shown in both plots. Please explain or modify.

The error processing takes place in two stages, which may be easier to follow separately. 1) Uncertainties are calculated for each SLR. 2) Uncertainties for the campaign average PSD are calculated, which are shown in Figure 2. We explain each of these steps below.

Additionally, the horizontal error bars on Figure 5 represent the minimum and maximum bin edges possible, using the bin centre and bin width uncertainties. Hence the actual uncertainty on the diameter centre point (which would be used in a typical progression of uncertainties from number concentration to volume concentration as stated by the reviewer), is much smaller than that shown on the plot. We show error bars to incorporate both bin centre and bin width in order to provide a realistic reflection of the real uncertainty in the sizing.

1) For each SLR, dN/dlogD uncertainties (vertical error bars) already includes bin width uncertainty *and* bin centre uncertainty, since they both contribute to the calculation of dlogD. dV/dlogD additionally takes account of the bin centre uncertainty again through the diameter cubed, as well as incorporating the uncertainty in dN/dlogD. Below is an example from one SLR, b932 R2, in the SAL.

In the figure below, we take the reviewer's data point close to 20 µm (diameter 18.7 µm). Here the uncertainties are as follows:

Bin centre uncertainty = 0.74 µm

Bin width uncertainty = 0.71 µm

Fractional uncertainty in dN/dlogD=0.28

For the uncertainty in dN/dlogD, the uncertainty from the bin width is 4 times larger than that from the uncertainty in the measured number concentration, so that the bin width error dominates the total error.

Fractional uncertainty in dV/dlogD=0.29

For the uncertainty in dV/dlogd, the uncertainty from the bin centre is around half that of the uncertainty propagated from dN/dlogD (which also already incorporates both bin width uncertainty and bin centre uncertainty). As a result, the fractional uncertainties in dN/dlogD and dV/dlogD are not very different in the two plots below, since they are both dominated by uncertainties in the bin size.

In contrast, for the CDP data point centred at 3.9 µm, the fractional uncertainties in bin centre and bin width are much larger (0.12, 0.05), which results in the much larger vertical error bar in both dN/dlogD and dV/dlogD.

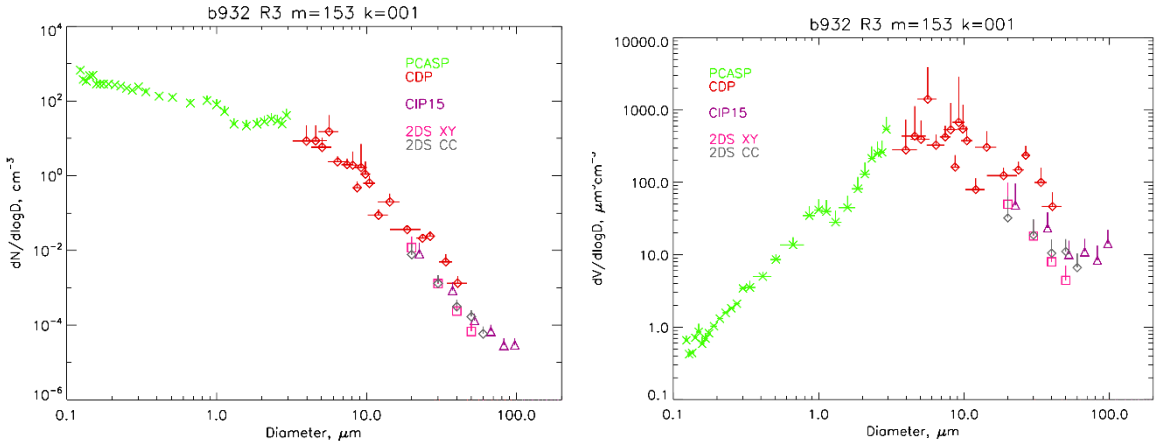

Figure: dN/dlogD (left) and dV/dlogD (right) for an individual SLR (b932 R3) in the SAL.

2) Secondly, uncertainties are combined to provide the SAL and MBL average PSD, e.g. as shown in Figure 2.

In order to do this, the random and systematic errors from each SLR are processed separately, as recommended by Baumgardner et al. (2017). This is because the systematic error (from sample area uncertainty and bin size uncertainty) does not reduce by increasing the sample size, while the random errors (from counting and discretization uncertainties) can be reduced by increasing the sample size. This is done by standard analytical error propagation. It turns out that for the CDP, beneath 20 µm diameter, the total uncertainties are dominated by the bin size uncertainties, while above this size the counting error becomes significant as well.

We have added information to the caption for Figure 2, “Horizontal error bars represent maximum bin width due to uncertainties in both bin centre and bin width.” We have also added the following text to Section 2.3.2:

“For the CDP at d < 20 µm bin size uncertainty was found to dominate the total uncertainty in dN/dlogD and dV/dlogD. Horizontal error bars in Figure 2 represent the maximum uncertainty in bin edges, derived from uncertainties in both bin centre and bin width. Uncertainties in bin size contribute to uncertainties in both dN/dlogD and dV/dlogD, and therefore the relative uncertainties do not change significantly between the two panels.”

Figure 2 is hard to understand also from another aspect: Either the measurement points are all at the lower boundary of the error, or the error always includes zero. If they are at the lower boundary, please explain why. In particular with a non-zero counting error (which is necessarily two-sided), this seems impossible. If the error

always includes zero, then the statement in P9 L27, “agree within the error bars” is meaningless, as all data could be zero.

In Figure 2 (and also Figure 5), only upper error bounds are shown, since for several points the lower error bars exceed the minimum on the log scale axis and impede visibility of the data points. This is now stated in the caption for both figures.

P8 L31 and P9 L4: if a particle was not counted for the given reasons – how was this underestimation of the concentration then accounted for? Decreasing proportionally the sample volume?

Yes, it is accounted for. The effective array width (EAW) changes depending on whether the all-in or centre-in approach is used. The EAW is used in calculation of the sample area (McFarquhar et al., 2017), and therefore the number concentration and its uncertainties. We added, “The sample area is adjusted for the effective array width, which is different depending on whether ‘all-in’ or ‘centre-in’ is used (McFarquhar et al., 2017), and therefore the calculated number concentrations account for this.”

P9 L6: For what reason the projected area equivalent diameter was not used, which appears to be a common standard in shadowing techniques (i.e. light microscopy)?

With hindsight, and ample data processing time and computation time, it would have been interesting to additionally process the OAP data using projected area equivalent diameter. However, a limitation of using this metric with the OAPs is that particles can sometimes appear hollow (e.g. due to being out of focus). Under these circumstances using projected area equivalent diameter would be a significant underestimate, and therefore it is not clear that this is the ‘best’ metric for the OAPs. We have added the words, “Area-equivalent diameters were not calculated because particles can sometimes appear hollow on the OAPs (McFarquhar et al., 2017) which would lead to undersizing.”

P9 L11-21: Please be more explicit on the error handling. Was is done by analytical error propagation, by Monte Carlo simulation, ...? What were the distribution assumptions(Poisson?)? How was the counting error treated, if measurement points with only 4 particles were regarded? If error bars are given: do they show a certain confidence interval, one (or more) standard deviations, or maximum errors?

Error handling was done by standard analytical error propagation. Counting error was calculated as $n^{1/2}$, where n is number of particles counted in the SLR. Size bins containing less than 4 particles in the whole SLR were disregarded, and therefore counting error was not calculated for these points. Error bars show maximum errors. This paragraph now reads:

“Uncertainties in number concentration for all size probes are propagated from 1Hz measurements, through to means over SLRs, through to the AER-D campaign averages. For all probes, random errors (due to counting and discretization error) and systematic errors (due to sample area uncertainty and bin size centre and width from Mie singularities) were accounted for in their contribution to total number concentration errors, and propagated by standard analytical error propagation. I.e. random error can be minimized by increasing the sample size (averaging across the campaign), while systematic error remains constant. For the CDP at $d < 20$ µm bin size uncertainty was found to dominate the total uncertainty in dN/dlogD and dV/dlogD. Horizontal error bars in Figure 2 represent the maximum uncertainty in bin edges, derived from uncertainties in both bin centre and bin width. Uncertainties in bin size contribute to uncertainties in both dN/dlogD and dV/dlogD, and therefore the

relative uncertainties do not change significantly between the two panels. All error bars represent maximum uncertainty."

P9 L30-35: Are there any arguments beyond consistency with previous measurements for disposing (if I understood correctly) the CIP15 CC data? It is stated that the 2DS XY metric is better – better in terms of what? Please explain.

Yes, as stated on p9 L29, the "the CC metric will oversize a non-spherical particle," since the circumscribing circle, by definition, does not take any account of a particles' non-sphericity. We refer specifically to the metric, and not the instrument here.

P10 L1: This type of effective diameter seems usually (Hinds 1999) to be called the Sauter mean diameter (apparently defined by Sauter 1926) or mean volume-surface diameter (Hinds 1999). As different effective diameters exist, I suggest referring to one of the mentioned denominations and referring in addition to a more fundamental paper (McFarquhar et al. 1998).

We have changed the effective diameter reference to Hansen and Travis (1974), and added the Hinds (1999) reference as well as adding 'volume-surface diameter.'

P10 L4-7: Given the high counting uncertainty associated with a single count of the maximum-sized particle, wouldn't there be a better option, e.g., fitting a log-normal distribution or power law into the data? At least, both mentioned approaches should be compared to allow for consistent comparison.

Since we disregard SLRs where fewer than 4 particles were detected, our counting uncertainty will be a maximum of 50% if 4 particles are detected, and reduce accordingly when more are detected. Actually, only 2 SLRs detected fewer than 6 particles in the maximum size, so the errors are substantially less. Fitting a lognormal or a power law to the data is not necessarily useful as the size distribution shape will not necessarily follow these fits.

P11 L12 (and below): As magnifications are relative to the used screen, a measure like nm per pixel or pixels per smallest particle would be more meaningful.

Values are: x2,000: 55.9 nm/pixel, x10,000: 11.0 nm/pixel. These have been added to the manuscript.

P11 L14-19: Wouldn't it make more sense using the same metrics as described for the shadowing instruments above?

In an ideal world, yes. The OAP software processing is computationally intensive, and ellipse fitting to the time-of-flight data is not currently an option. Since more realistic metrics could be derived from the filter samples, we chose to use these (rather than a less appropriate metric consistent with the OAP data), hoping to inform knowledge on dust properties for the dust aerosol community. In the future, with the benefit of hindsight, processing the OAP data differently would be considered. See also response to P9 L6 above.

We tested the impact of processing the filters PSDs differently, mimicking the XY and CC metrics as much as possible. However it should be noted that even when processing the filters data like this, the two are still not equivalent. This is because the 2DS and CIP15 data are 2-D projections of a 3-D particle orientations in the atmosphere. While the filters data are also 2-D projections, the particles likely fall with their largest axis parallel to the filter sample. Despite this, using the XY metric for the filters data did not produce any noticeable changes in the PSD. Contrastingly, the CC metric processing produced PSDs with a mode shifted towards larger particles,

and often detected a maximum particle size one size bin greater than that shown in Figure 7. These effects on the PSD mimic the differences seen between the 2DS CC and 2DS XY in Figure 2.

We have added a sentence to Section 2.4 to indicate this:

"Additionally, we tested the sensitivity of the filters PSD to using the mean XY and CC sizing methods applied to the OAP data (not shown). Using a mean XY method on the filters data did not produce significantly different results, while using the CC method was found to shift the PSD towards larger particles, similar to the findings from the OAP size metric comparisons."

P11 L25-29: Please state where you draw the lines between thenardite/sulfate and gypsum/sulfate.

No quantitative separation is used since the percentages vary depending on the contribution from the other oxides. However, typically when Thenardite (Gypsum) is classified, percentages of Na_2O and SO_3 (CaO and SO_3) are within 10% of each other. We have added information about the classification of Thenardite to section 2.4 which was missing, and added information on the oxide percent.

P16 L18-20: This behavior was described and a similar explanation was given for the same geographical region and season a while ago (Jaenicke et al. 1978), and also some model approached seem to predict that (Garrett et al. 2003), so maybe a short comparison with previous finding would make sense here and enhance the general significance of the findings.

Thank you for these interesting references. We have added to this section the following, "This has also been suggested by Jaenicke and Schutz (1978) from aerosol surface observations at Sal, Cape Verde, where giant particles ($d > 40$ µm) were observed to arrive at the site a day after that of coarse dust particles ($6 < d < 60$ µm)." Garrett et al. (2003) appears to be more relevant to the introduction, since that work found that concentrations of d>10um particles were under predicted by models for transport across the Atlantic, so we have added that there.

P16 L28-30: This finding is surprisingly similar to the volume distributions shown for Cape Verde in winter time, comparing dusty and marine situations (Kandler et al.2011), so a comparison could show a broader relevance.

Thank you for this reference. Actually this finding is a little different from those of Kandler et al. (2011). In Kandler et al. (2011), for the dust case mean, the volume distribution peaks sharply at around 10 microns, whereas for our 'giant dust in the MBL' cases the volume distribution peaks at ~5 µm and ~30 µm. For the 'maritime' cases the PSDs shapes appear quite different too.

We have added a paragraph to Section 3.2 comparing the PSDs to those in the literature. We are also about to submit a follow-up paper which includes a thorough comparison of the AER-D PSDs to those in the literature, drawing together the latest results.

P17 L14-18: This would mean that the flow through the filter would have been ten times as high as the one used for calculating the size distributions – is this still in a physical probable range? Can there exist any aerosol concentration effects due to high velocity gradients during sampling?

Firstly, yes, this is plausible. There is nearly a factor of 10 difference in flow rate measured between different SLRs. Therefore it is possible that problems here could have strongly impacted the retrieved size distributions.

Secondly, non-isokinetic sampling can artificially increase number concentrations in certain size ranges. E.g. if the aspiration speed is larger than the aircraft speed then the submicron fraction will be artificially enhanced, and vice-versa. However, this is not consistent with the filters PSD being offset across all size ranges compared to the wing probes.

P17 L22: Smoothness of the curves could be related to different size intervals. The wing probes seem to have more size intervals (with higher counting uncertainties) in Figure 7.

This is true. We have added, "in part due to the broader size bins used" to this sentence.

P18 L23-32: Probably a median aspect ratio, instead of a modal value, would make interpretation less dependent on a single interval. In particular, as in the following the values are compared with median values from other sources, which otherwise can't be compared.

Thank you for this suggestion. We have calculated median values of the aspect ratios and added them to the panels in Figure 9. We have incorporated them into the discussion in this paragraph and re-written it. Although calculation of the median reveals higher values than the modal values, our values still appear a little lower than those from SAMUM1, 2 and AMMA, ranging from 1.16 to 1.54 for the full PSD.

P20 L24-25: How about sea-salt reacted with sulfuric acid?

Yes, this has been added.

P21 L7-12: How would black carbon have been identified in this work? Were all particle images manually inspected for fractal-like structures (doesn't come clear from the method section).

Yes, all images were manually inspected during the scanning procedure. Out of 6500 particles analysed, only one single black carbon particle was observed, in a chain, or fractal-like structure.

We have adjusted this text to reflect this more accurately, which now reads, "Additionally, in contrast to Liu et al. (2018), we do not detect any black carbon on the filter samples **in significant quantities**, which they find present predominantly between sizes of 0.1 to 0.6 µm. **During the analysis of 6500 particles, only one black carbon chain structure was observed.**" We also added the following sentence to the methodology section 2.4 for clarification, "Only one black carbon chain-like structure was observed during the analysis of over 6500 particles, and therefore this aerosol category is not included."

P22 L20: In particular for the internal mixing, there is plenty of room with respect to complexity for calculating an effective value (Nousiainen 2009; Lindqvist et al. 2014).

These citations have been mentioned in this sentence now.

P24 L6: In addition, also measured refractive indices show the dependency on iron (Moosmüller et al. 2012; Caponi et al. 2017), so it appears to be consistent in general.

We have added these citations to this section.

Figure S2: Where does the 'step function' of the imaginary part at 700 nm wavelength derived from?

This 'step function' at 700 nm originates from the refractive index dataset of hematite, which drops sharply from ~0.2 to ~0.0013 in the imaginary part at this wavelength.

==========

Corrections

General: The order of the figures does not correspond with the order of their references in the text.

General: The table numbers in the text don't fit with the table numbers at the end.

Apologies for these errors, these have now all been corrected.

P3 L8-11: including into calculation/model?

This was calculated – the wording has been changed.

P4 L22: Why time-of-flight? Wasn't it an SP2 instrument?

We have changed the wording to 'real time measurements,' which is more accurate. (Yes, it was an SP2).

P4 23-25: While the link to the optical property measurement is clear, the reference to the ice nucleation measurements and to the modeling work doesn't seem to add something useful here.

We believe it is useful to tie together the papers relating to the same flights since the impacts of dust in the atmosphere are multiple. However, we have deleted the reference to the paper in preparation since it is not yet submitted.

P4 26-30: I suggest removing the paragraph, as the structure is standard.

Done

P5 L15-22: If results from SAVEX and CATS are not discussed here, these explanations should be removed.

These flights and results are discussed here. Certain flights covered multiple objectives. We prefer to retain this information since it explains the choice of location for each of the flights presented in this article and may be used in subsequent publications.

P8 L2: "ambiguities" instead of "singularities"?

Changed.

P9 L9: What does "Instead, ... sizing metric" refer to? Aren't the previous sentences the section about the sizing metric?

Here we intended to refer to the sizing metric of XY versus CC, pointing out that the choice of XY vs CC is the main controller of PSD in this case, as opposed to the choice of an 'all-in' versus a 'centre-in' approach. We have clarified this by adding, '(i.e. XY versus CC)' to this sentence.

P10 L8-9: "do not have a minimum detection concentration level, but at low particle concentrations the sampling statistics simply become poor": In fact, this is the detection limit. With poor sampling statistics the (counting)

error becomes high in comparison with the signal. If it is decided to omit data below a certain signal/error ratio, the detection limit is introduced (which is a common procedure).

This is actually what we intended to say. To clarify, we have added to this sentence, ", introducing an effective detection limit."

P10 L14: "PSD' size distribution" – doubling "size distribution"

Removed

P12 L10: "low SEM signal" low image contrast?

By 'low signal' here we refer to the energy, or number of photons emitted, not the image contrast. Since this is dependent on particle volume, for smaller particles the number of photons emitted is lower, or non-existent for very small particles, and the analysis and interpretation becomes difficult. We have added, "(fewer photons emitted for smaller volume particles)" to this sentence.

P15 L5: increased?

Changed

P16 L24: There seems to be no (b) in Figure 6.

Changed

P18 L5: In Figure 7, in most cases the volume maximum is below 10 m, in one above (filter size distribution). "Dominating" therefore doesn't seem to be appropriate for the largest particles with respect to the mass.

This has been changed to, "can contribute substantially to"

P18 L12: Sentence ends with a comma.

Changed.

P24 L28: Most of section 4 is rather a summary than conclusions, so the section should be termed accordingly.

We have followed the guidelines from ACP at https://www.atmospheric-chemistry-and-physics.net/for_authors/manuscript_preparation.html for manuscript composition, which indicates that 'Conclusion' should be used. Also in our final paragraph we make some broader recommendations and comments.

Table 1: Different reference formats. Maybe explain instrument abbreviations, e.g., as addition in Table 3?

The reference formats have been corrected. We have created an appendix containing the instrument acronyms, and added this to the caption of Table 1.

Table 3: Check caption

This has been corrected.

Table 4: different time formats between table 2 and 4 (?)

Table 4 has been changed to comply with the given ACP date and time terminology guidelines.

Table 5: 'IT' number format (E+01 etc.)

These have been changed to the 1.16×10^{1} format.

Figure 2: Both y axes should have the same number format.

The axis for the right hand panel has been changed to be consistent.

Anonymous Referee #2

Ryder et al. discuss airborne measurements of Saharan dust performed between Cabo Verde and the Canary Islands in August 2015 with focus on several aspects of the dust, for example the coarse mode size distribution. I think the paper is interesting and fits well into the scope of ACP. Overall, the paper is in a useful shape but there are many, mainly minor, things the authors should improve before the paper is ready for final publication.

We thank reviewer 2 for their comments and are pleased that they find the paper interesting. We have responded to the minor comments below and corrected or altered them in the manuscript. In particular the question about why we did not process the CIP15 data with the XY metric has led to additional reprocessing of some of this data, which has been informative to the manuscript. Further details are given below. We apologize for incorrect cross-referencing of tables and figures, which have all now been corrected. We have added clarification to our flight patterns section to better explain the data.

General comments:

Abstract: Maybe one sentence with results for the MBL could be added.

We have added, "Within the MBL, mean effective diameter (d_{eff}) and volume median diameter (VMD) were 4.6 µm and 6.0 µm respectively, giant particles with a mode at 20-30 µm were observed, and composition was dominated by quartz and alumino-silicates at d > 1 µm."

On p3l6 you define coarse and giant mode dust. However you do not follow this definition, e.g. at p7l15, p9l32, p12l27, p25l25. Please make sure that the paper is self consistent.

We have changed the introduction to reflect the references throughout the rest of the text. It now reads, "Coarse and giant mode dust (defined here as d>2.5 µm and d>20 µm, respectively)…"

Often the citation type, e.g. '(Ryder et al., 2013)' vs. 'Ryder et al. (2013)', is not correct.

These have been corrected throughout the manuscript.

You did not define the flight legs. At p11l5 you mention 'R2' for the first time, but you did not introduce this properly. In Fig. 4 an undefined 'P2' etc appears, probably also refering to flight legs. I suggest to add a proper introduction of the nomenclature and to add a table (maybe in the supplement) with more details about the flight legs considered in the paper (e.g. name of leg, start time, end time, duration, height, etc.).

We refer the reviewer to Section 2.1, 'Flight Patterns,' where in the final paragraph profiles and straight-and-level flight legs are explained and defined. We have added an explanation of R and P which refer to straight and level runs (SLRs) and profiles respectively, as suggested by the reviewer. We have also changed the terminology throughout the paper to use SLR rather than 'flight leg,' since SLR relates more closely to the 'R' abbreviation and is also the abbreviation used by the UK research aircraft community. Full time and altitude information for profiles and SLRs can be accessed online. We have added, "Full information about profile and SLR times and altitude are available from the Centre for Environmental Data Analysis (see Data Availability)."

You write SSA in the text but use omega_0ˆ550 in the figures. Please use only one of these.

We prefer to use or ω_0 for the figures, so have added this to the first appearance of SSA in the introduction, "decreasing the single scattering albedo (SSA or ω_0)."

Sometimes for the imaginary part values a 'i' was added after the value, sometimes not. This should be made consistent, perferably removing 'i' everywhere because the 'imaginary part' is a real value; see also your definition at p8l18.

The 'i's' have been removed from the text.

Often, the main text refers to the wrong table number.

We apologize for this and have changed the cross-references.

Specific comments:

p1l24: In my view 'during' should be replaced by 'at'.

Changed

p1l28: 'constituting up to 40% of dust mass': As you mention this number in the abstract, it should also be mentioned in Sect. 3.3.

We have added to Section 3.3, "In the extreme, up to 90% of dust mass can be found at sizes greater than 5 µm and up to 40% at sizes greater than 20 µm."

p2l3f.: It is unclear what 'this complex evolution' refers to. Suggestion: '... to capture correctly both the dust composition and the size distribution including their changes during transport in order ...'

We have rephrased this sentence.

p3l27: 'preceeding the AER-D flights' comes a bit surprisingly. Please reformulate without refering to AER-D which is introduced only later.

We have removed the mention of AER-D and rephrased the sentence.

p3l33: I think 'however' could be removed here.

Done

p4l1: 'Mie theory conversion': it is not very clear what is meant. Please reformulate.

This has been changed to, "the scattering cross-section to particle size relationship is non-monotonic."

p5l7f.: 'The dust events sampled 550 nm AODs from 0.4 to 0.8' should be reformulated.

This now reads, "The dust events revealed AODs at 550 nm from…"

p5l19: 'aerosol structure' is a bit unclear. You probably mean the vertical distribution (structure) of the aerosol.

Correct, we have changed this

p5l20: 'nearer the ...' could be replaced by 'closer to the'.

Done

p5l26: 'Figure 1b' does not exist.

Changed to Figure 1

p5l28: 'flight' could be added before b920 and b924.

Done

p7l3: The wavelength list may be a bit confusing. Maybe you can just write the wavelengths in parentheses after the instruments?

This now reads, "Scattering measurements were made by a TSI 3563 integrating nephelometer (at wavelengths of 450, 550 and 700 nm). Absorption measurements were made by a Radiance Research Particle Soot Absorption Photometer (PSAP) at 567 nm."

p7l25: 'aerosol' should be replaced by 'particle' to make the sentence more general. Particles with 6.2mm are usually not aerosol particles but much more likely some kind of hydrometeors.

Done

p8l18: PCASP and CDP do not operate at 550nm. This should be mentioned here including your assumption that the refractive index does not change between 550 nm and the instrument's wavelengths.

We have altered this paragraph which now reads, "Bin sizes also depend on the choice of refractive index applied. In this work, a complex refractive index ($n^{550} = m^{550} - ik^{550}$) of 1.53-0.001i was used to determine the PCASP and CDP bin sizes, as determined from Section 2.5 for 550 nm. Since the PCASP and CDP operate at wavelengths of 633 and 658 nm, we assume a constant refractive index across these wavelengths. This is supported by the relatively flat spectral refractive index shape at these wavelengths indicated in Figure S2."

p8l28: You could write ' ... in two different ways, resulting in different sizing metrics.' This would help the readers in the subsequent paragraph.

This has been changed to, "Thus to investigate some of these uncertainties, the 2DS data was processed in two different ways, using two different sizing metrics."

p9l3f.: Were the particles rotated such that one dimension is minimized and the other maximized? Or were x and y measured for each imaged particle without such rotation?

No, the particles are not rotated. We added the sentence, "The x and y dimensions are measured along the probe array, i.e. the particle is not rotated to minimize or maximize either dimension."

p9l6: '... though diameters will be lower than an area-equivalent diameter for example, if the particle is an ellipse.' looks wrong. For example, assume x=1 and y=2. Then D_XY=(x+y)/2=1.5. The area-equivalent diameter however is D_area=(1*2)^0.5=1.414 which is smaller than 1.5. This could be a reason why also the mean XY method somewhat overestimates the 'real' particle size.

This was a typo, 'lower' should have been 'larger.' We have added and changed this paragraph as follows: "The mean XY method is considered to give a more representative diameter for non-spherical particles than the CC

metric. If the particle image is an ellipse, the mean XY diameter will be larger than an area-equivalent diameter, as used by the filter sample data. However, the OAP images capture 2-D image projections of the particles in their atmospheric orientation, while the filter samples are will be collected with their largest surface lying parallel to the filter sample, and therefore may be oversized in this context."

p9l8: I wonder if there is a reason why you don't use the mean XY method (instead of the CC method) for the CIP15 in this discussion paper?

This is a good point, and we would have done so initially in an ideal world. Unfortunately much of the OAP processing was initially done by different institutions for each OAP, and used institutional conventions, often selected for consistency between different fieldwork campaigns and optimized for ice/cloud particles, which allowed the whole of the ICE-D data to be processed with one assumption (over half the ICE-D flights were cloud flights).

However, we have now run additional processing on the CIP15 data using a centre-in, mean XY metric, although unfortunately it has not been possible to do this for all the AER-D flights analysed in this article. Two contrasting examples are shown below.

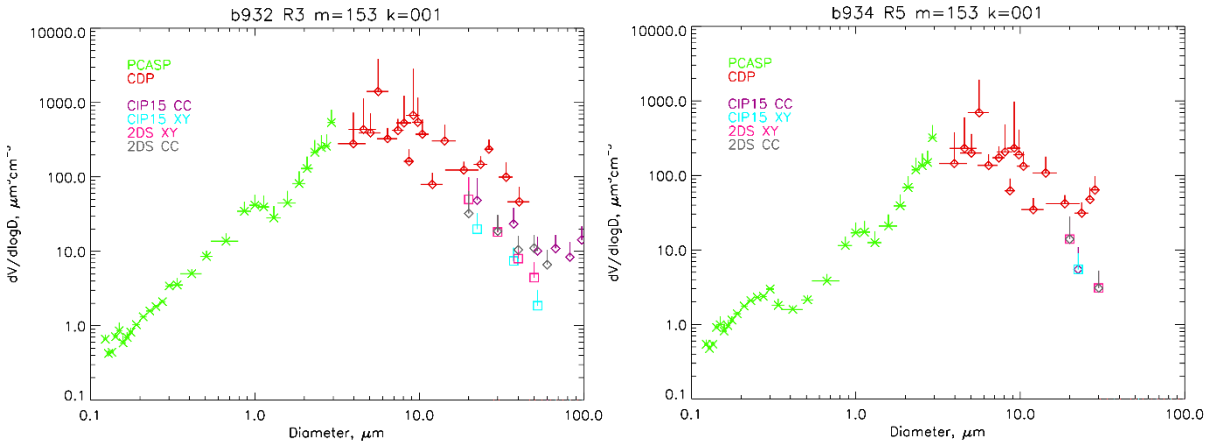

It is clear that the biggest difference in the OAP size range stems from the choice of size metric (XY vs CC), rather than the instrument (2DS vs CIP15). The difference is not noticeable when the giant mode is smaller (right hand panel). The difference in mean d_{eff} from all SLRs analysed between the 2DS XY and the CIP15 XY is under 1%. Differences for the CIP15 CC are 4.5%, and for the 2DS XY under 1%. These uncertainties, and particularly that for the XY metric, are smaller than the 5% error already applied due to the uncertainty due to choice of refractive index for the OPCs.

However, the impact of OAP metric and instrument on d_{max} is larger. Differences from the 2DS XY d_{max} to CIP15 XY d_{max} are +6%, to the CIP15 CC +37%, and to the 2DS CC +21%. The upper error of 6% (based on the instrumental differences using the more realistic XY metric) is now incorporated in the upper error bars on d_{max} shown in Figure 8b. These are small relative to the existing error of 5µm when d_{max} is around 20 µm, but comparable to the error when d_{max} is larger, and can be seen for example in the now asymmetric error bar for the points at d_{max} = 80 µm.

New Figure 8b:

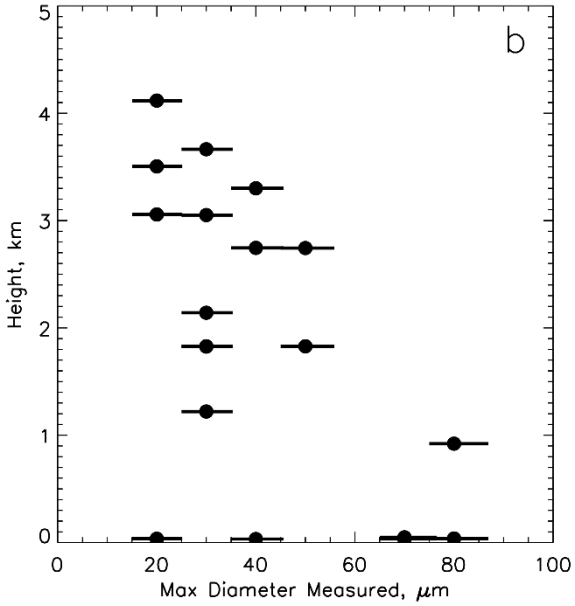

The following text has been added to section 2.3.2, "Some CIP15 AER-D data were also processed using a centre-in, mean XY metric, but unfortunately it was not possible to process data for all the SLRs with this method. Therefore this data was used to inform on instrumental differences between the 2DS and CIP15 when processed with the same size metric (XY mean). It was found that the impact on the full PSD was very small (d_{eff} differed by under 1%), but that d_{max} was up to 6% larger with the CIP15 XY compared to the 2DS XY. The upper uncertainty of 6% in d_{max} was therefore propagated in combination with the other uncertainties in d_{max}."

p9l12: Which flight leg length do these 10ˆ-5 cmˆ-3 correspond to, approximately?

This number concentration corresponds to a flight leg length of 132 km or approximately 20 mins of flight time on the FAAM aircraft. This information has been included.

p9l20: It is unclear what '... errors due to bin size from ...' means. Please reformulate this sentence.

This sentence has been deleted.

p9l28f.: 'as expected when the particles are non-spherical (section 3.2)' could be replaced by 'as excepted for dust'.

This sentence has been re-worded.

p10l9f.: This looks quite similar to p9l10ff. Maybe you could bring both together or at least refer here to the previous text (e.g. 'Therefore, we remove, as mentioned, cases where fewer ...').

Done

p10l17: 'of around 0.2 to 1 m' should be replaced by 'smaller than 2-3m' when considering Fig S1.

Done

p11l5: 'R2', 'R5' are not defined.

These are now explained by the additions to the 'Flight Patterns' section.

p11l15: The areas of the ellipses were larger than the areas of the particle 2D projections because you used circumscribed ellipses. How large is this difference? Why didn't you use the area of the projection itself to determine the area-equivalent diameter?

We did not use image contrast and brightness levels with automatic processing since this would have meant that not all particles would be detected, since not all particles had similar contrast and brightness. This technique would have allowed measurement of projected area. Instead images were analysed manually by circumscribing an ellipse to the particles. This method was selected in order to maximise the number of particles analysed, and as it is operator independent, systematic and reproducible. However, the particles were not notably jagged at their edges.

Secondly, p11 L17-19, ("Note that this technique may oversize the particle volume, particularly where the shape is a platy silicate with a tendency to fall with its largest surface parallel to the substrate; e.g. Chou et al. (2008) found the height of dust particles examined under SEM to be around one third of their major axis length.") is an *additional* process which may lead to the filters PSD being oversized compared to the wing probes, which relates to the orientation in which plate-like particles fall flat on a filter substrate.

This paragraph now reads, "It was not possible to use automated image contrast to calculate projected particle area because of a high degree of variability in particle contrast. Our filters sizing this technique may oversize the particle size for two reasons. Firstly, the area of a fitted ellipse may be larger than a projected particle area, though the particles were not noticeably jagged around their edges. Secondly, our method may oversize particle volume where the shape is a platy silicate and has a tendency to fall with its largest surface parallel to the substrate. For example, Chou et al. (2008) found the height of dust particles examined under SEM to be around one third of their major axis length."

p12l29: Shouldn't '0.0001' be replaced by '0.0005'? Otherwise I don't understand this description.

This has been rewritten to better explain, and now reads, "a Mie scattering code is used to generate optical properties at 550 nm, using the ACC PSD, with refractive index of m^{550}=1.53 and k^{550} incrementing in steps of 0.0005 from 0.0005 to 0.006, but with an additional smallest value of 0.0001 which was required for the MBL SLRs."

p13l1: 'Figure 8b' shows something else.

This sentence has been deleted. The correct figure is referred to in the next sentence (Figure 3).

p13l9: 'between 0.0015i to 0.0025i' doesn't fit to the mode value of 0.001.

Thank you for pointing this out, there was a typo and it now reads '0.0005 to 0.0025.'

p13l11: Why do you use 'volume fraction' here and 'number fraction' for the external mixing case (p13l30)? How big is the difference between both cases?

Volume fraction is appropriate for the internal mixing assumption since the volume of each mineral determines its contribution to the total refractive index. For the external calculations, our scattering code requires input in the form of number concentration. Internally, the code calculates the surface area, since this determines the aerosol scattering properties. If the internal mixing assumption is used, but with number fraction, the results are very different because the smallest sized particles dominate the number concentrations, and have a greater contribution from different compositions such as sulfate and salt (as shown in Figure 11).

p15l16: I suggest to briefly discuss the difference from Marenco et al., who find maximum AODs of 2.0.

We have added, "Note that lidar-derived AODs and extinction shown by Marenco et al. (2018) are slightly lower than those shown here, which may be due to different extinction properties of the dust at the lidar wavelength of 355 nm, and the Rosemount inlet enhancement effects shown in Figure S2, or the differences between a lidar curtain and sloped aircraft in-situ profile."

p15l28: 'each flight leg': As Fig. 5 shows only a single leg inside the SAL for each flight I assume that there was only one flight leg in the SAL for each flight? However, then Fig. 2 and 5 seem to not fit to each other as mentioned in a separate point below. In general, the legs should be described better.

This is not the case. Successive flights included 2, 1, 6, 2 and 3 legs in the SAL. Much of the data overlies itself for some parts of Figure 5b so that it might be inferred that fewer legs were performed. We do not intend for the reader to be able to distinguish each individual flight leg from panel a, and the points discussed in the text can seen. We have added information to the caption of Figure 5 to state how many SLRs are shown. With the addition of information to the 'Flight Patterns' section, the legs should be more understandable.

p15l33: I do not really understand this sentence. Would the absense or presence of the coarse mode not always have an effect on the overall shape of the size distribution?

Here we intended to explain that during AER-D, when dust concentrations were higher, the coarse and giant mode particle concentrations increased together, as well as the concentration of particles in the accumulation mode, which meant that the overall shape of the PSD remained the same. This contrasts to Fennec, where coarse and giant particles often increased in concentration but without the smaller particle concentration increasing. In that case, the shape of the size distribution *did* change. A few changes and additions have been made to this paragraph to state this more clearly, and also in the conclusion.

p16l1: 'peak volume concentration' is unclear. I suggest to write 'The peak of the volume distribution during ...'.

Done

p16l8f: 'Figure 5b; green, orange and red'

Changed

p17l3: ' may be aligned horizontally in the atmosphere ... ': I suggest to add here a reference to Ulanowski et al. (2007), DOI:10.5194/acp-7-6161-2007, who made some simulations on this topic (see e.g. Fig. 9 of that paper).

Done

p18l10: How does 'Particles sized over 20 m diameter were detected in 100%' fit to Fig. 8b which shows that there are cases with D_max=20m?

This has been changed to '20 um or larger.'

p18l14: 'Figure 8c' does not exist.

Changed to Figure 8b

p19l4: particles

Changed

p19l10: 4643 has probably too many significant digits. I suggest 'around 4600'.

Done

p19l12: 'decreases' is maybe the wrong word here. I suggest 'is lower'.

Now reads, "is around a factor of ten lower than the total mass"

p19l15: 'PM2.5' in not defined. As it is used nowhere else, I suggest to just write 'the accumulation mode'.

Done

p20l16: 'as they only include iron when detectable as single-iron particles': As far as I understand this sentence, 'they' should be replaced by 'we' and 'detectable as single iron particles' by something like 'iron was the dominant component of a particle'.

Done

p22l17: There is one 'is' too much.

Changed

p22l28: 'coarse mode present' could be replace by 'coarse particles'.

Done

p22l29: 'so' could be removed.

Done

p23l1f: The sentence could be improved by removing 'same' and adding 'also' after 'mode'.

We thank the reviewer for this suggestion. After further consideration, we think that the sentence sounds better as it was and prefer to leave this unchanged.

p23l4: 'as dominate' is unclear.

'as' changed to 'which'

p23l7: 'RI' is not defined.

Now defined in Section 2.3.2, first occurrence of refractive index.

p23l10: Suggestion: 'The variability of the optical properties of dust in the SAL is probably mainly determined by …'.

The wording here has been changed.

p23l14: 'the variability of the' should be inserted before 'optical'.

Done

p23l26: I suggest to write 'the variation of the SSA as function of composition, represented by k550', because this order is more logical and also better fits to Fig. 13 considering that the vertical axis usually shows the dependent variable (y=f(x)).

Done.

p24l1: 'optical property' could be replaced by 'SSA' to be more specific.

Done

p24l13ff: It is not clear how this fits to p13l29f where you write that you use the same size distribution (only number-weighted) for all components. In addition, you could consider a size dependency not only in case of external mixtures but also in case of internal mixtures.

Regarding number-weighting – see response to point above (p13l11).

Actually, we have calculated the size dependency of SSA for both the internal and external mixing cases, but perhaps this was not clearly described. These points can be seen as the large diamonds in Figure 13b. We have added a second panel to figure 14 to show the same values but for the full PSD, for the iterated RI, internal mixing RI and external mixing RI, and now discuss this in the text.

p24l21: 'In contrast to Fennec observations of the full PSD and associated optical properties over the Sahara,' could be removed. Maybe the information about the location could be added somewhere on line 22.

Done

p24l30: I suggest to delete 'during August 2015' and to add instead a new sentence like 'The flights were performed in August 2015 between Cape Verde and the Canary Islands.'.

Done

p25l7: 'to be' could be removed.

We prefer to leave the wording here.

p25l14: 'Deff for the SAL the mean (minimum, maximum) was' should be reformulated.

Done

p25l26: 'giant MBL mode particles' could be reformulated.

'MBL mode' has been deleted.

p25l30: calculate

Changed

p26l6: 'slightly lower' is an understatement because the 'base value' of the aspect ratio is 1.0. Then your value is only about half of the literature value.

We have deleted 'slightly.'

p26l6: 'and quartz' could be removed when considering Fig. 11.

We changed the wording to, "alumino-silicate particles dominated the composition at sizes above 0.5 µm, followed by quartz."

p26l28: 'was extremely scattering' should be replaced by 'was only very weakly absorbing'.

These two statements are essentially the same, therefore we leave the wording as it is.

p26l33: I suggest to start a new sentence after 'dust' and to write 'Particles larger than expected from sedimentation processes alone are found.'.

Done

Table 1: The reference style is not consistent.

Changed

Table 1: During 'SALTRACE' also the 'CAS-DPOL' instrument was used, measuring up to 50m (Weinzierl et al., 2017).

This has been corrected.

Table 2: The 'General Flight Aims and Conditions' do not very well fit to Table 1 of Marenco et al. Furthermore, you write 'b923', and Marenco et al. 'B923'. Maybe this could be more harmonized between both papers.

We have added 'CATS underflight' to Table 2 to b920, and changed 'SAVEX' to 'SAVEX-D' to align better with Marenco et al. Table 1. Other than this the details reflect the same information. We use 'b' lowercase as this is the official terminology used by FAAM for flight numbers, and will consider adjusting the text in Marenco et al.

Table 4: Negative latitude values don't make sense here.

These were errors and have been corrected.

Table 4: Longitude and latitude values for b923/b924 do not fit to Fig. 1.

These have been corrected.

Table 6: Sometimes you write 'D_eff' and sometimes 'd_eff'.

Corrected to d_{eff}.

Table 6: With 'derived RI' you mean the refractive index you iterated to fit the optical measurements? If yes, 'iterated RI' would be more specific.

Changed

Table 7: What means 'assuming internal mixing' here? In my understanding, the mixing state (internal/external mix) is only relevant for optical calculations but not for the derivation of the refractive index from filter samples.

In order to calculate the refractive index from the filter sample composition, only the internal mixing assumption can be used. In the external mixing assumption, the calculations step straight from the refractive index of the individual mineral components to their optical properties, and then to the optical properties of the total aerosol sample. They do not provide a refractive index for the total aerosol sample as an intermediate step. This is why the external mixing case cannot be shown on Figure 13b.

Figure 4: What is 'SLRs'?

As stated above, we now explain SLR in Section 2.1, 'Flight Patterns,' and use SLR throughout the manuscript instead of 'flight leg.'

Figure 5a: The dV/dlogD value for b924 (green) at the largest three size bins is more than ten times higher than the corresponding average value shown in Fig. 2. However, there are only five flights and SAL flight lags. How do these figures relate? How did you calculate the average in Fig. 2? See also my comment on p15l28.

As stated above, there are 14 flight legs shown in Figure 5a. Thus the weighting towards the b924 data is much less than 1 in 5. Please see response to reviewer 1 for the details of creating the campaign SAL average shown in Figure 2 and error processing, and associated text added to the manuscript.

Figure 6: You write '6(a)' while there is no '6(b)'.

a has been deleted

Figure 7: The dashed lines are not very well visualized and the description is missing in the legend (at a reference to p17l12 should be added).

We have added this to the legend, and plotted the dashed line with open circles to be clearer.

Figure 9: 'Aspect ratios histograms as a function of number fraction of particles' is not clear. You mean 'number fraction of particles as function of aspect ratio'?

Yes, we have changed this as suggested.

Figure 10c: It looks like there is a height dependence of the fraction of D>5m particles within the SAL. I think this height dependence should be briefly discussed in Section 3.3.

Thank you for this suggestion. We have added the following to this section:

"Additionally there appears to be a trend with altitude shown in Figure 10c: the mean mass fraction at d > 5 µm decreases steadily from 0.75 at the surface to 0.23 at 5 km altitude. A decrease is also evident in panel d with the

largest fractions being found towards the bottom of the SAL (excluding the MBL). These decreases with dust mass as a function of altitude are somewhat in contrast to the homogeneous distribution of dust size throughout the SAL shown in Figure 8. This may be due to the data shown in Figure 10c coming from profiles rather than SLRs, such that more data is available, and also that although d_{eff} represents the full size distribution, as such it is relatively insensitive to smaller changes in the coarse and giant particle concentration. Either way, there is clearly evidence of coarser dust particles being more prevalent towards the bottom of the SAL (and also in the MBL), indicating deposition processes occurring."

Figure 11: Relative 'n particles' for '10.0 to 40.0' shows no big difference between 'b920 R2' and 'b928 R2', so it is a bit unclear why you mention here 'B928 R2 (top right) contained giant mode MBL particles.' which should also be true for b920.

We refer to the wing probe measurements which show the substantial giant mode in the MBL for b928 R2 but not for b920 R2. This is now clarified in the caption.

Figure 11: The last sentence could be 'Errorbars are counting uncertainties.'.

Changed.

Figure 13: 'size-specific RI is used': Is this explained in the main text?

The text has been changed to be clearer here.

Anonymous Referee #3

The study characterizes the dust properties during the beginning of trans-Atlantic transport of dust particles. It presents new airborne measurements of dust size distribution, composition, shape, and optical properties within the Saharan Air Layer (SAL) and the Marine Boundary Layer (MBL) taken during the AERosol Properties – Dust (AER-D) fieldwork campaign in August, 2015. In their 6 flights, the authors used wing-mounted optical particle counters and shadow probes to measure dust sizes between 0.1 and 100 m diameter, a nephelometer and an absorption photometer to measure dust optical properties, and an in-cabin filter collection system to collect dust samples.

The focus of the study is to highlight the presence and contribution of coarse and giant mode dust particles to the dust size distribution, mass loading, shape, composition, refractive indices and optical properties. The authors found that within the SAL, dust particles with diameter (D) greater than 20m are detected in 100% of the cases, and those with D>40m are detected about 36% of the cases. Of the dust particles detected, 14% of the masses are for dust particles with size D<2.5m, 60% for size D>5m, and about 10% for D>20m. In addition, the authors also found the following: the shape of the measured particle size distribution does not vary significantly between dust layers; the modal aspect ratios are in between 1.2 to 1.4; the real part of dust refractive index in both SAL and MBL is within 1.47 to 1.49, but the imaginary part is between 0.0012 - 0.003i in the MBL and between 0.0004 - 0.0005i within the SAL. They also found that the single-scattering albedo (SSA) at 550nm decreases in the SAL when the measured coarse and giant dust particles are included in the calculation. However, they concluded that the variability of the SSA is not controlled by the dust size distribution, but by the variability in dust composition, contrary to previous studies.

Observational datasets for the coarse and giant dust particles, reported in this paper, are very important to better constrain dust properties in climate models. Current climate models over-estimate the fine-mode dust particles and under-estimate the coarse-mode particles, leading to uncertainties in the estimation of dust optical properties. This is largely due to inadequate observational constrains, and only few similar measurements of size-resolved dust properties are publicly available, with few obtained during the summer time period. Hence, high-quality measurements with a wider particle size range, like those reported in this study, are needed.

We thank the reviewer for their comments, and are pleased that they consider our observations high-quality and important for better constraining dust properties in climate models. In response to the three main comments, we have shortened sentences for clarity as much as possible throughout the whole manuscript, provided a detailed response to the back trajectories point, and expanded on the applicability of Mie theory in this work. Details are given below.

The paper is generally well written, and I believe it also meets the ACP standards. I recommend it for publication, if the authors can address the following comments:

1. Reading through the paper, some parts of it are rather confusing. This is primarily because some of the sentences are too long, making the reading of the paper a bit tiring. The long sentences also sometimes obscure the point the author may want to pass across. I encourage the author to look more closely into each sentence, separating the long ones to multiple short sentences, where necessary. While few of these sentences are highlighted below, I cannot point to all the instances and I hope the author will do the due diligence in addressing this comment throughout the paper.

Pg 14 Lines 6-8, 14-16. Pg 15 Line 1-4. Pg 17 Line 1-4, 10-12. Pg 18 Line 22-26. Pg 20 Line 2-5. Pg 25 lines 16-19

In all cases apart from one, these sentences have been shortened. We have also been through the whole paper and shortened long sentences where possible.

2. Pg 6: The authors should provide a more objective assessment of the dust source areas. While HYSPLIT back-trajectory understandably are associated with uncertainty at the trajectory endpoints, it is still a reasonable method to determine the age of the dust particles, especially when the alternative is subjective. This is particularly useful for the dust particles in the SAL, where such trajectory can easily be estimated along a constant potential temperature surface, therefore avoiding possible influence of the convective events within the boundary layer. Doing it this way, may give a more close and objective approximation of the dust age, to which the SEVIRI images can eventually confirm. Free-tropospheric dust aerosols generally preserve their temperature for a considerable distance from the source region. Isentropic trajectories are therefore suitable above the boundary layer (e.g. Merrill et al., 1986).

From the HYSPLIT website (https://ready.arl.noaa.gov/HYSPLIT_traj.php), the figure below shows an example of the isentropic back-trajectory for flight #b932 starting on 20/Aug/2015 at 12Z for an arbitrary height of 2800 m above sea level. This height corresponds approximately to the highest extinction in your Fig. 4. The figure is a 3-day back-trajectory and it appears to suggest that the starting point after 3 days is approximately in the same area as suggested by SEVIRI in you Figure 1. This calculation can be repeated for different height within the SAL, and can also be combined with the SEVIRI images to give a more objective estimate of the dust sources, the age and the starting location.

In addition, the figure below uses the NCEP reanalysis dataset. It may be useful, however, to use a better quality meteorological dataset, like ERA-Interim with relatively higher resolution, to drive the HYSPLIT back-trajectories. ECMWF assimilates meteorological data from radiosondes that launch from few but important stations over north Africa. This may reduce the uncertainty even further, giving some more credence to the methodology.

We appreciate the reveiwer's efforts to investigate one of our cases with HYSPLIT. We have to point out, however, that the trajectory endpoint location was incorrect as the b932 dust investigated was centred at around 20W, 20N (see red flight track in Figure 1) rather than at the Cape Verde Islands themselves. Below we show a HYSPLIT back trajectory that was used as part of the analysis that in part led to the discussion in Section 2.2, using the correct location and time for the in situ sampling of b932. Three starting heights were chosen to cover the altitudes of the dust layer sampled. We also show two SEVIRI images indicating the two dust uplift times for this case.

It can be seen that the back trajectories do not capture the actual uplift location, times or transport path of the dust over the Sahara at all. The back trajectories would lead us to infer dust uplift times/locations of 00UTC on 19 Aug in central Mauritania at ~20N (blue) and ~22N (red), and at ~12UTC on 17 Aug in northern Chad. While in fact the SEVIRI images show that uplift occurred firstly near the Mali/Algeria border between 17 Aug 1000 UTC to 0100 UTC 18 Aug, and then again over Northern Mali at 1200-1400 UTC on 18 Aug. Therefore we believe that the uplift locations suggested by the back trajectories are incorrect, and that we have a better representation for these events using the SEVIRI imagery. This should not be interpreted as a negative appreciation of back trajectories in general.

Secondly, according to HYSPLIT timings, the dust would be inferred to be aged >36h (lower layer, red/blue) and >96h (upper layer, green). The SEVIRI imagery dust ages are 45-47 h for the Northern Mali uplift, and 58-73 h for the Mali/Algerian border uplift.

The transport pathway of the dust is clearly visible on the satellite images. The dust is transported from the Mali/Algeria border region to the northwest, before moving southeastwards to the coastal area. This pathway is not captured at all by the back trajectories.

The image below shows back trajectories calculated using the GDAS 0.5 degree meteorology dataset. We also ran the same case with the NCEP reanalysis data, and the results were similar. To our knowledge, ERA-Interim data is not available with the web-based HYSPLIT trajectory model.

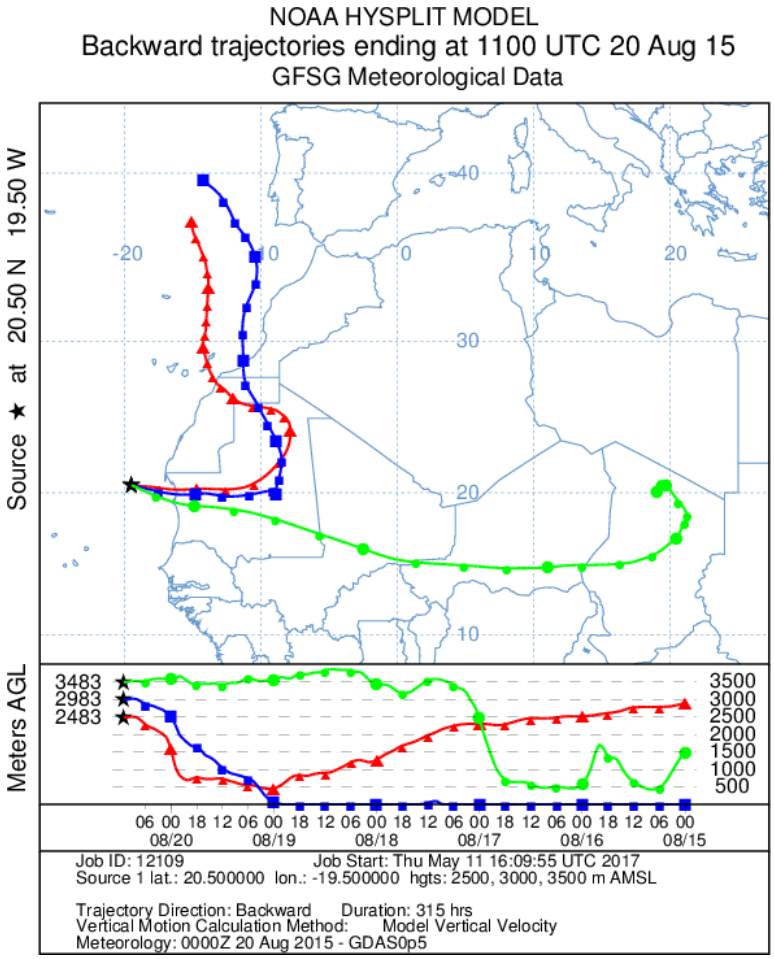

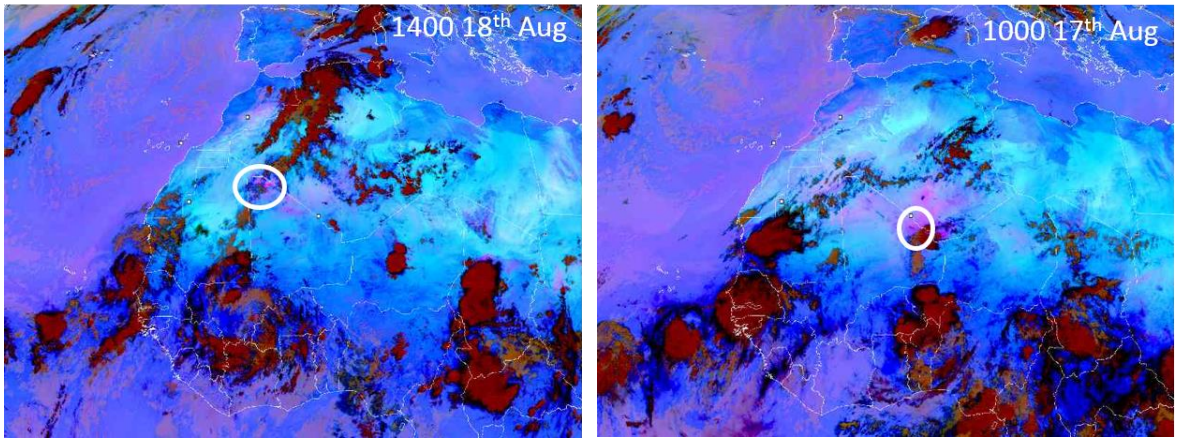

As stated in Section 2.2, we had already examined all the HYSPLIT back trajectories for our dust cases, and compared them to the SEVIRI imagery. ("HYSPLIT back trajectories were also run, but are not used to determine source location or age here, since in every case they indicated a transport path differing from that shown by the SEVIRI imagery.") Occasionally the dust source location was similar to that from SEVIRI, even though the indicated transport pathway was different. However, the back trajectories also always showed either too fast or too slow transport, which would lead to an incorrect assignment of dust age. Additionally, another limitation of back trajectories is that they only indicate when an air mass nears the surface, but do not reflect potential uplift conditions (e.g. surface wind strength, soil conditions…).

We have rewritten the last paragraph of Section 2.2 to explain this more clearly.

We agree with the reviewer that back trajectories, following a constant potential temperature, can be a very useful tool for situations like dust in the SAL. However, for the large part of the time between dust uplift and sampling during AER-D, the dust was over the Sahara and within the Saharan Boundary Layer, which can extend up to 5 km altitude. The SEVIRI images show that convection and clouds were frequently present along the transport pathway of the dust. Therefore over the Sahara our dust events cannot be assumed to follow isentropic trajectories, and the difference between the HYSPLIT results and the SEVIRI imagery confirms this.

Several Fennec studies examined model biases over the Sahara, including the effects of unresolved cold pools. Garcia-Carreras et al. (2013) found a "crucial role of convective cold pools in explaining model tropospheric temperature bias," and suggest that, "the misrepresentation of moist convective processes can affect continental-scale biases, altering the West African monsoon circulation," even when additional radiosonde data is assimilated. Engelstaedter et al. (2015) found that models have errors in moisture distribution which "is likely to have consequences for simulations of Saharan thermodynamics and dust emissions caused by convection-driven cold pools." Roberts et al. (2017) find that ERA Interim winds are systematically underestimated over the Sahara. Despite the assimilation of a few radiosondes over the Sahara, models still struggle to resolve Saharan meteorology (Garcia-Carreras et al., 2013), which has knock on effects on dust back trajectories which rely on model fields. We have added citations of these papers in Section 2.2.

Given the challenges models still face in simulating clouds, convection and dynamics over the Sahara, and the clear visibility of the dust transport pathways in the SEVIRI imagery, the uncertainty and subjectivity in the SEVIRI methodology was perhaps overstated in Section 2.2. The last paragraph of Section 2.2 has been rewritten to try to better reflect this, as follows:

"The SEVIRI imagery is not able to give altitude-resolved information, and can be subjective, particularly when dust loadings are light, at low altitude or in a moist environment, making dust appear less pink and more difficult to identify (Brindley et al., 2012). This is more evident in the dust tracked for flights b932 and b934 where dust loadings were lower. This introduces a small level of uncertainty into both the source locations and dust ages, which we account for by giving generous error bars to the dust uplift times and source locations. HYSPLIT back trajectories (Draxler and Hess, 1998; Stein et al., 2015) were also run for the AER-D dust events. In only one of the five dust events was the dust source location similar to that observed in the SEVIRI imagery. In every case the back trajectories indicated a transport path and transport time different to that shown by the SEVIRI imagery. Although the SEVIRI methodology has its limitations, the back trajectory method results were clearly not compatible with the information from SEVIRI. Therefore back trajectories are not used to determine source location or age here. Additionally, another limitation of back trajectories is that they only indicate when an air mass nears the surface, but do not reflect potential uplift conditions (e.g. surface wind strength or soil conditions). It has been shown that models and reanalyses are currently unable to adequately represent convective events and winds over the Sahara and Sahel, particularly due to the challenges of representing cold pools. For example, Garcia-Carreras et al. (2013) examine the role of convective cold pools and suggest that "the misrepresentation of moist convective processes can affect continental-scale biases, altering the West African monsoon circulation." Many other publications have examined the misrepresentation of Saharan convective events (Marsham et al., 2011; Heinold et al., 2009; Sodemann et al., 2015; Trzeciak et al., 2017; Allen et al., 2015; Roberts et al., 2017; Engelstaedter et al., 2015). Since convective events are the drivers of dust uplift in all the AER-D cases we do not consider HYSPLIT back trajectories (with relatively low model resolution of half a degree) to be informative here due to the challenges the models face in representing Saharan circulation. Finally, we note that back trajectories are recommended to be used with caution for dust events over the summertime Sahara (Trzeciak et al., 2017)."

3. The authors should either carefully justify the application of the Lorenz-Mie theory for dust particles larger than 20m or use a more appropriate methodology for this size range. The manufacturer-provided size bin diameters were calibrated against polystyrene latex spheres, which the authors corrected to diameter of dust using Lorenz-Mie method (on PCASP and CDP). But Lorenz-Mie theory is only valid when the particle size is comparable to the wavelength (Bohren and Huffman, 1983). For coarse and giant dust particles with diameter larger than 20 m, the application of Lorenz-Mie theory is no longer valid, and instead the geometric optics method may be useful (see Bi et al., 2009).

Firstly, although we process the entire CDP PSD using Mie theory, covering diameters up to around 50 microns, we only use the CDP data up to diameters of 20 microns, as at this point the CIP15 or 2DS data is given precedence. Therefore this is not an issue for the CDP data.

Secondly, we would like to point out that Mie theory is an exact solution for spheres of any size, and has no upper (or lower) limit, but converges to geometric optics for larger sizes and to Rayleigh scattering approximations at smaller sizes. (e.g. Petty, 2006). However, we assume that the reviewer is referring to the applicability to Mie code for the use of non-spherical particles. In this work we assume that the particles are spherical for optical property calculations. Sensitivity of SSA to the assumption of spherical particles was tested by Otto et al. (2009)

and Johnson and Osborne (2011), who found that SSA changed by under 1% and 2% respectively when non-spherical particles were assumed. This is less than our error in SSA described in Section 2.3.1, and therefore we consider this an acceptable assumption. We have added this information and citations to the text, as well as a new methodology section 2.6 'Calculation of Optical Properties' to make this clear.

Petty, (2006) A first course in Atmospheric Radiation, Ch 12, Sundog Publishing, USA.

Specific Comments:

Pg 5, Line 7. Pg 7, Line 20. Pg 14, Line 4. Pg 16, line 25. Pg 18, line 2. Pg 21, line 15: The table numbers referenced here are wrong. Please check all other reference in the paper.

All table references have been corrected.

Pg 3, Line 9-10: Re-write for clarity.

Done

Pg 9, Line 8-9: I wonder if this difference between the "all-in" and the "center-in" is actually quantified. This text referenced here appear to be an assumption as suggested by the use of word "considered". If the latter is the case, I suggest this sentence should be re-written to clarify this point.

The sample area is actually adjusted depending on the particle size and whether all-in or center-in is used, since they both impact the effective array width and therefore the sample area, and hence the number concentration calculated (McFarquhar et al., 2017). We have added the sentence, "The sample area is adjusted for the effective array width, which is different depending on whether 'all-in' or 'centre-in' is used (McFarquhar et al., 2017), and therefore the calculated number concentrations account for this."

Pg 16, Line 24: There is no need for "6a", there is just one figure. Please also correct this in other places of the manuscript.

These have been corrected.

Pg 18 line 14: Figure 8c is not provided.

Corrected.

There is no definition of some acronyms – an example is the "SLR" acronym in the text or in Fig. 4. I suggest the author look through the paper and make sure every acronym is defined before use.

We have added more detailed flight manoeuver information and explanations to section 2.1, and also added acronym explanations as an appendix.

Anonymous Referee #4

This manuscript presented a study of Saharan dust based on airborne observations made over the Eastern Tropical Atlantic near the western African coast. The measurements were targeted to characterize dust microphysical, chemical and optical properties, including size distribution, particle shape, mass loading, composition, refractive indices, and SSA. This study contrasted the dust properties in Saharan Air Layer and the marine boundary layer. The authors highlighted several important findings which will advance the current understanding and benefit later modeling studies. The manuscript is logically organized and well written. It is noted that the authors provided meticulous details about the instrument, data reduction, and uncertainty analysis. This reviewer believes that this manuscript shall be published after the authors considering a few suggested minor changes, which will not alter the major finds of this study.

We are pleased that the reviewer finds our results important and beneficial to modelling studies, and that they consider our data processing and uncertainty analysis meticulous. We thank the reviewer for their detailed comments which we hope have led to a clearer manuscript. We have responded to each comment in turn below. In particular, we thank the reviewer for their point about the relationship between SSA, k and d_{eff}, and have tried to clarify our aims here in confirming whether k or d_{eff} is the main contributor to the variability in SSA. Full details are given below.

Minor Comments:

Page 4, Line 4: Please clarify that while light shadowing techniques are not impacted aerosol composition or Mie theory conversion issues, they still can be impacted by non-spherical particles.

Done

Page 5, Line 7: Change “Table 1” to “Table 2”

Done

Page 5, Line 8, please describe the AOD and clarify if the AOD is calculated over the dust layers. Please also make changes to the table caption so that it will be consistent with the text

The AOD is calculated across the entire aircraft profile, not just the dust. We have changed the text, the table does not need changing.

We added to Section 2.1, “The events sampled revealed accumulation mode AODs at 550 nm (see Section2.3.1)…”

We added to Section 2.3.1, “Accumulation mode AODs are calculated from aircraft profiles by integrating the scattering and absorption measurements between the minimum aircraft altitude (typically around 30 m above sea level) to the top of the profile (typically around 6 km). Therefore AODs represent both SAL and MBL aerosol.”

Page 5, Line 26: Change “Figure 1b” to “Figure 1”

Changed

Page 6, Lines 18-19: The authors note that visually identifying and tracking dust plumes is subjective, difficult, and potentially error-prone. Would it be possible to instead obtain the underlying satellite data and apply an objective threshold?

As in the response to reviewer 3, we feel that we potentially over-emphasized the disadvantages of the SEVIRI method, and have changed the text accordingly.

Methods have been developed to automatically detect dust emission using the SEVIRI imagery, e.g. Ashpole and Washington (2012). To our knowledge none have been developed to track or back-track transported plumes. Applying a threshold to the underlying data may indeed have been possible, but would still be subject to variability due to underlying surface emissivity from surface temperature and surface type, altitude of dust in the atmosphere, obscuration by clouds.

Page 7, Line 5, please add a brief discussion on the choice using PSAP correction by Turnbull (2010) and difference between this correction and that by Virkkula, AS&T, 44:706-712, 2010

Turnbull (2010) reports on corrections necessary to the FAAM PSAP measurements based on the original work by Bond et al. (1999), and clarifications to this publication described in Ogren (2010), and clarifies any errors in calculations performed by Haywood and Osborne (2000).

Virkkula et al (2010) report corrections to the Virkkula et al (2005) publication, dealing with inconsistencies between a one and three-wavelength PSAP. The 2010 publication resolves the discrepancies. Since we employ a one-wavelength PSAP, not a three wavelength PSAP, we do not consider these publications in our corrections.

We have added the Bond et al. (1999) and Ogren (2010) references to the text.

Page 11, line 31, please provide a more quantitative criteria to define the word “dominant”

This has been changed to, “they were classified according to their dominant component type which made up the greatest oxide percentage.”

Page 13, Line 1: Figure 8b is unrelated to SSAs; perhaps Figure 13b was intended?

This sentence has been deleted.

Page 13, Line 8: Please restate the rationale to hold the real part of the refractive index at 1.53, in the context that in Section 3.5, the real part is found to be 1.47-1.49 based on the filter sample composition.

We also tested the sensitivity of our results to different real parts of the refractive index: 1.48 and 1.58. We found that effective diameter (resulting from varying the RI used to correct the PCASP and CDP data) changed by under 5%. For the optical properties calculated, scattering and absorption each changed by around 4%, but SSA changed by under 0.5% since typically both scattering and absorption changed in the same direction.

Also, for the reasons stated in Section 3.5, we believe the filters real refractive index results to be biased low.

We added, “Although a value of 1.53 for m^{550} is higher than that produced by the filter sample composition results (Section 3.5, 1.47-1.49) the filters result is likely biased low due to the reasons discussed in Section 3.5. We also performed a sensitivity test to using m^{550} of 1.48 and 1.58, and found that deff changed by up to 5% and SSA by under 1%.”

Page 13, Lines 14-20: This information might be better suited to a table, which could also include the actual refractive index used for each substance.

Although we appreciate this suggestion, since the spectral refractive index data is used rather than just a value at 550 nm, this would not fit into a table easily.

Page 14, Line 4: Change “Table 3” to “Table 4”

Done

Page 16, line 25. Please provide a brief discussion on how the “best-fit” compare to observed volume size distribution and number size distribution and Change “Table 4” to “Table 5”

Differences between the effective diameter calculated with the best-fit lognormal curves and the observed PSDs are between 10-15%. This relatively large error derives largely from the size range between diameters 3 to 20 µm measured by the CDP. The fluctuating nature of the CDP PSD does not reconcile it to an easy fit with lognormal curves. This has been added to this paragraph.

Table reference changed.

Page 18, Line 2: Change “Table 5” to “Table 6”

Done

Page 18, Lines 8 and 11: These two statements regarding a potential decrease in dmax with height seem contradictory. Please clarify to make them consistent.

This has been changed to, “There is no clear trend of d_{max} decreasing with altitude.”

Page 18, Line 14: There is no Figure 8c

Changed to 8b.

Page 19, Line 14: Please supply a reference for the dust density value.

The value comes from Tegen and Fung (1994), and is used by Woodward (2001) and Bellouin et al. (2011) as the default density value for dust aerosol in the Met Office Unified Model and also the radiation scheme within the model. References have been added.

Page 21, Line 15: Change “Table 6” to “Table 7”

done

Page 23, Line 26 (and Figure 13b): Some readers may wonder if finding a good agreement between the imaginary part of the refractive index and the SSA is expected, given the relationship between k, absorption, and SSA. The authors should consider the significance of confirming that the relationship exists in this case.

We are not trying to show or confirm the existence of a relationship between k, absorption and SSA. We acknowledge that this is an established relationship. However, the PSD can also impact the SSA. Therefore the SSA can be influenced by several factors, and our aim is to investigate which factors dominate the variability of

the SSA. During Fennec, for example, the variability in the PSD was the dominant controller of the SSA, rather than k. Contrastingly, during AER-D we found that the PSD did not vary much, and therefore variability in k dominated the variability in SSA.

We have rewritten this paragraph to try and better explain this finding and its significance, and also in the conclusion. This paragraph now reads:

"Contrastingly to Figure 13a, Figure 13b shows that the SSA variability was strongly influenced by the variability in composition. This is the case for both accumulation mode observations of SSA, and for the full size distribution. It is not surprising that variability in k^{550} influences absorption and therefore SSA. However, the SSA can be influenced by several factors, including the PSD. Our aim is to investigate which factors influence the variability of the SSA. Therefore it is notable that there is so little variation in the PSD during AER-D that the composition (or k^{550}) is the main factor contributing to the variability of the SSA. This finding is notably the opposite from that found during Fennec, where the size distribution was the dominant controller of optical properties. Liu et al. (2018) show that hematite content is important in the ICE-D/AER-D samples as a controlling factor on optical properties. Moosmuller et al. (2012) and Caponi et al. (2017) also show dependencies of refractive index on iron content. This is consistent with our findings that the calculated refractive index from the filter samples is strongly influenced by the iron content and its absorbing properties. It appears that over the Sahara, variations in the PSD (affected by dust age) have an important impact on SSA, while over the ocean the impacts of composition (perhaps either by chemical aging or by sampling dust from different sources) become more important."

Page 24, Line 20: Change "Table 5" to "Table 6"

Done

Figure 4: This figure suggests the flight b924 and b934 did not have extensive sampling in MBL, please make changes in text accordingly

We are not sure why the reviewer thought this. Figure 4 shows aircraft profile observations. Each flight included one SLR in the MBL. We have added information to Section 2.1 (Flight Patterns) to further explain the aircraft manoeuvres. See also the response to reviewer 3.

Figure 6: The blue shading was very faint on my screen. Perhaps a darker shade, or even hatching, could be used instead. Also, as there are no other parts to this figure, "Figure 6(a)" should be changed to "Figure 6" (as well as in the associated text).

'a' has been removed. The shading appears fine on our screen and print-offs. We will closely monitor the readability of this figure in proof-reading, where the original eps files will be used rather than a convert to .png contained in the MS Word document.

Coarse mode mineral dust size distributions, composition and optical properties from AER-D aircraft measurements over the Tropical Eastern Atlantic

Claire L. Ryder[1], Franco Marenco[2], Jennifer K. Brooke[2], Victor Estelles[3], Richard Cotton[2], Paola Formenti[4], James~~im~~ B. McQuaid[5], Hannah C. Price[6], Dantong Liu[7], Patrick Ausset[4], Phil D. Rosenberg[5,8], Jonathan W. Taylor[7], Tom Choularton[7], Keith Bower[7], Hugh Coe[7], Martin Gallagher[7], Jonathan Crosier[7,~~9~~8], Gary Lloyd[7], Eleanor J. Highwood[1], Benjamin J. Murray[5].

1 Department of Meteorology, University of Reading, Reading, RG6 6BB, UK
2 Met Office, Exeter, UK
3 Department de Física de la Terra i Termodinàmica, Universitat de València,46100 Burjassot, Spain
4 LISA, UMR CNRS 7583/Université Paris Est Créteil et Université Paris Diderot, Institut Pierre Simon Laplace, Créteil, France
5 School of Earth and Environment, University of Leeds, Woodhouse Lane, LS2 9JT, UK
6 Facility for Atmospheric Airborne Measurements, Cranfield, UK
7 Centre for Atmospheric Sciences, School of Earth and Environmental Sciences, University of Manchester, Manchester, UK
8 National Centre for Atmospheric Science, Fairbairn House, 71-75 Clarendon Road, Leeds, LS2 9PH, UK
~~9~~8 National Centre for Atmospheric Science, University of Manchester, Manchester, UK

Correspondence to: Claire Ryder (c.l.ryder@reading.ac.uk)

Abstract

Mineral dust is an important component of the climate system, affecting the radiation balance, cloud properties, biogeochemical cycles, regional circulation and precipitation, as well as having negative effects on aviation, solar energy generation and human health. Dust size and composition has an impact on all these processes. However, changes in dust size distribution and composition during transport, particularly for coarse particles, are poorly understood and poorly represented in climate models. Here we present new in-situ airborne observations of dust in the Saharan Air Layer (SAL) and the Marine Boundary Layer (MBL) ~~during~~ at the beginning of its trans-Atlantic transport pathway, from the AER-D fieldwork in August 2015, within the peak season of North African dust export. This study focuses on coarse mode dust properties, including size distribution, mass loading, shape, composition, refractive indices and optical properties. Size distributions from 0.1 to 100 µm diameter (d) are presented, fully incorporating the coarse and giant modes of dust. Within the MBL, mean effective diameter (d_{eff}) and volume median diameter (VMD) were 4.6 µm and 6.0 µm respectively, giant particles with a mode at 20-30 µm were observed, and composition was dominated by quartz and alumino-silicates at d > 1 µm. Within the SAL, particles larger than 20 µm diameter were always present up to 5km altitude, in concentrations over 10^{-5} cm^{-3}~~,~~ constituting up to 40% of total dust mass. Mean d_{eff} ~~effective diameter~~ and ~~volume median diameter~~VMD were 4.0 µm and 5.5 µm respectively. Larger particles were detected in the SAL than can be explained by sedimentation theory alone. Coarse mode composition was dominated by quartz and alumino-silicates; the accumulation mode showed a strong contribution from sulfate-rich and sea salt particles. In

the SAL, measured single scattering albedos (SSAs) at 550nm representing d<2.5 μm were 0.93 to 0.98 (mean 0.97). Optical properties calculated for the full size distribution (0.1<d<100 μm) resulted in lower SSAs of 0.91-0.98 (mean 0.95) and mass extinction coefficients of 0.27-0.35 m^2g^{-1} (mean 0.32 m^2g^{-1}). Variability in SSA was mainly controlled by variability in dust composition (principally iron), rather than by variations in the size distribution, in contrast to previous observations over the Sahara where size is the dominant influence. It is important that models are able to capture the variability and evolution of ~~this complex evolution of~~ both dust composition and size distribution with transport in order to accurately represent the impacts of dust on climate. These results provide a new SAL dust dataset, fully representing coarse and giant particles, to aid model validation and development.

1 Introduction

Mineral dust plays an important role in the Earth's climate system. It is the most dominant aerosol species in the atmosphere, constituting 70% of the global aerosol mass burden and 25% of the aerosol optical depth (AOD) (Kinne et al., 2006). Once uplifted from arid regions, dust is transported thousands of kilometres across the Atlantic Ocean from the Sahara desert (Carlson, 2016), and across the Pacific Ocean from eastern Asian deserts (Li et al., 2010). The abundance and long-distance transport of mineral dust allow it to affect the climate system via different processes. Dust interacts with both solar and infrared radiation, exerting a direct radiative effect at the top of atmosphere and surface, which can alter atmospheric heating rates and stability, surface fluxes and temperatures, and thus influence regional circulation and precipitation (Lavaysse et al., 2011; Strong et al., 2018). Dust particles may influence cloud development on a microphysical level by acting as both cloud condensation nuclei and ice nuclei (Kumar et al., 2011; Hoose and Mohler, 2012), affecting cloud optical properties and lifetimes. Finally, dust has an impact on biogeochemical cycles since it provides iron to the ocean (Jickells et al., 2005) and phosphorous to the Amazon rainforest (Yu et al., 2015), which can lead to subsequent changes in atmospheric carbon dioxide absorption by the oceans and vegetation and associated climate feedbacks. Dust impacts anthropogenic activities by depleting solar radiation available for solar energy generation, both in the atmosphere (Charabi and Gastli, 2012) and by deposition to solar panels (Piedra and Moosmuller, 2017). It also negatively impacts aviation in dust laden regions due to a reduction in visibility (Middleton, 2017), and finally high dust loadings can negatively impact respiratory health (Prospero et al., 2014). Many of these processes are dependent not only on total mass of dust, but also its size (Mahowald et al., 2014).

Recent studies have revealed how poorly climate models are able to simulate uplift and transport of dust. Evan et al. (2014) find that CMIP5 climate models underestimate dust mass path (the mass loading of dust per square metre) by a factor of three, 66% of which is due to a bias in size distribution skewed towards smaller particles, and 34% of which is due to an underestimate in emission fluxes. As a result, these models systematically failed to reproduce basic aspects of dust emission and transport, casting doubt on their ability to simulate regional African climate and the response of African dust to future climate change. Kok et al. (2017) used an observationally constrained emitted dust size distribution in combination with global model

simulations to determine dust radiative forcing. They estimated a more positive radiative forcing (-0.48 to +0.20 Wm^{-2}) compared to previous estimates from the AeroCom models (-0.6 to -0.3 Wm^{-2}) which over represented smaller, more cooling particles, and under represented the coarser, more warming particles. Kim et al. (2014) compared AeroCom models to satellite data, and found disagreement in dust optical depth of up to a factor of 4, also finding that mass extinction coefficient (MEC, which is sensitive to particle size distribution) varied by 27% between models. These studies emphasize the sensitivity of model predictions of key parts of the climate system to representation of particle size, and the challenges of capturing observations in current climate models.

Coarse and giant mode dust (defined here as d>2.5~~1~~ µm and d>2~~1~~0 µm, respectively) is of particular importance to its interaction with radiation. In the shortwave (SW) spectrum, larger particles (assuming fixed composition, shape and roughness) increase the amount of atmospheric absorption, thus decreasing the single scattering albedo (SSA or ω_0) (Tegen and Lacis, 1996). For example, calculations have shown ~~it has been shown~~ that including coarse and giant mode particles measured over the Sahara results in the SSA dropping from 0.92 to 0.80 at ~~wavelengths of~~ 500 nm. This resulted in ~~and~~ the associated atmospheric heating rates increasing by up to a factor of three (Ryder et al., 2013b). In the longwave (LW) spectrum, coarse particles are equally important. Otto et al. (2011) show that including particles larger than 5 µm diameter more than doubles the dust LW AOD; and the magnitude of the LW radiative effect can act to change the sign of the net radiative effect of dust (Woodage and Woodward, 2014). ~~Song et al. (in review, 2018)~~ Song et al. (2018) show that dust radiative closure assessed by satellite observations in both the shortwave and longwave spectra can only be achieved with a substantial coarse mode dust size distribution.

Part of the challenge in modelling the dust cycle is that it is not currently clear even from observations what all the mechanisms for the transport of coarse particles are. In theory, dry deposition depends on particle size, but is also influenced by particle shape, density and roughness (Li and Osada, 2007). However, observations have consistently shown that coarse dust particles are transported further than predicted by dry deposition theory (Maring et al., 2003; Ryder et al., 2013a; Weinzierl et al., 2017; Gasteiger et al., 2017; Denjean et al., 2016; Stevenson et al., 2015). Various suggestions as to the observed retention of the coarse mode during transport have been proposed, including solar absorption by dust generating convection and therefore additional vertical mixing in dust layers (e.g. Gasteiger et al. (2017)), turbulence within dust layers (Denjean et al., 2016), and electrostatic charging of dust (Harrison et al., 2018). Measuring and quantifying these processes remains challenging. In order to do so, high quality observations of dust properties at multiple stages throughout transport events are required.

Over the ~~10 years preceding the AER-D flights~~last 15 years, aircraft observations have made significant advances both in observing dust in increasingly remote regions of the Sahara near dust sources and in utilizing instrumentation to characterize the full dust size distribution. The major fieldwork campaigns ~~over this period~~since 2005 are shown in Table 1, including the measurement technique and maximum size measured. Size distributions can be measured inside aircraft cabins behind inlets,

although this introduces restrictions enforced by inlet dependent size cuts which prevent the measurement of the coarser particles to varying degrees. In recent years, wing-mounted sizing probes have been more routinely operated, removing any inlet sizing restrictions. Wing-probes have employed both light scattering and light shadowing techniques. ~~However,~~ Optical Particle Counters (OPCs) measure light scattering, and post-processing requires converting scattering cross section to particle size. This relationship, although dominated by particle size, is also impacted by aerosol composition (via the refractive index), and the ~~Mie theory conversion~~scattering cross-section to particle size relationship is non-monotonic. Non-spherical particles may also impact the retrieved size distribution. These limitations, impacts and uncertainties are discussed in detail by Ryder et al. (2015). Optical Array Probes (OAPs) can be wing-mounted and utilize light shadowing techniques for particle sizing, and are not subject to the above uncertainties, and therefore present a valuable method for sizing of coarse dust particles, as demonstrated by (Ryder et al., 2013b), although sizing can still be subject to uncertainties such as from particle shape. All wing probes can also potentially suffer from modification of the flow around the probe housing and particle bouncing from the probe tips (Korolev et al., 2013; Weigel et al., 2016; McFarquhar et al., 2017).

The progressive airborne measurement of larger dust particle sizes has demonstrated the prevalence of coarse and giant particles both over desert regions and far from sources. For example, Weinzierl et al. (2009) detected particles larger than 40 µm in 20% of cases over Morocco during SAMUM1, even up to 5 km altitude. During Fennec, dust particles sized over 100 µm were measured at altitudes up to 5 km over Mali and Mauritania (Ryder et al., 2013b). During SAMUM2 over the Atlantic Ocean, although dust particles sized over 10 µm were present in 88% of cases, no particles sized over 30 µm were detected (Weinzierl et al., 2011). However, these observations were performed within the low altitude wintertime Saharan dust plume (under 1.5 km), whereas the summertime elevated dust plume within the Saharan Air Layer (SAL) is subject to different meteorological and dust uplift and transport mechanisms (Prospero and Carlson, 1972; Karyampudi et al., 1999; McConnell et al., 2008).

Here we present new airborne measurements of aerosol in the tropical Eastern Atlantic region, obtained during August 2015 as part of the AERosol Properties – Dust (AER-D) fieldwork campaign, which ran alongside the Ice in Clouds Experiment – Dust (ICE-D) project. We utilize size distribution instrumentation aboard the UK FAAM BAe146 research aircraft consistent with the Fennec campaigns of 2011 and 2012 (Ryder et al., 2015) and present dust properties measured during summer, the peak North African dust transport season (Doherty et al., 2008), with a particular focus on the properties of the coarse mode. New ~~time-of-flight~~real time measurements of accumulation mode hematite content measured during several of the same flights, and their optical properties, are presented separately by Liu et al. (2018). Ice nucleating properties of the dust sampled are given by Price et al. (2018), ~~model comparisons are performed by O'Sullivan et al. (in preparation),~~ and vertical structure is analysed by Marenco et al. (2018, in review).

~~Section 2 describes aircraft flight patterns, determination of dust sources activated during AER-D, aircraft instrumentation and derivation of refractive indices. Results are presented in Section 3, including the vertical distribution of aerosol, size distributions and mass concentrations, dust composition and refractive indices and finally the optical properties. Conclusions are presented in Section 4.~~

2 Method

2.1 Flight Patterns

During August 2015, the UK BAe-146-301 Research Aircraft operated by the Facility for Airborne Atmospheric Measurements was stationed at Praia on the Cape Verde Islands, for the ICE-D and AER-D field campaigns. The AER-D project comprised six flights, focusing specifically on dust properties within and beneath the SAL. Each flight was performed 4 to 5 days apart, due to the transported dust in the SAL displaying intermittent character, typical for summertime dust export (Jones et al., 2003; Schepanski et al., 2017). Details of the flights are shown in ~~Table 1~~ Table 2 and flight tracks shown in Figure 1.

The ~~dust~~ events sampled revealed ~~550 nm~~ accumulation mode AODs at 550 nm (see Section 2.3.1) from 0.4 to 0.8, which is within the range expected from August climatology over the Eastern tropical Atlantic indicated by satellite imagery (not shown). The aircraft observations revealed mostly typical vertical dust structure (see Section 3.1). The exceptions were b923 and b924, a pair of flights which observed an intense dust outbreak with AODs of up to 2.5 at around 24N off the coast of West Africa, with in-situ and remote sensing observations showing a different and complex vertical structure compared to the conventional SAL model of an elevated dust layer (discussed in Marenco et al. (2018, in review).

Two flights (b928, b934) formed part of the Sunphotometer Airborne Validation Experiment in AER-D (SAVEX-D) project, focused on providing airborne measurements for comparison with two types of ground-based sunphotometer. Requirements for non-cloudy skies and moderate to high dust loadings, and proximity to the ground-based sunphotometers required that the first ~~SAVEX~~SAVEX-D flight (b928) took place close to Praia, while the second (b934) took place close to the island of Sal. Three flights (b923, b924 and b932) were aimed mainly at mapping the vertical and horizontal aerosol structure ~~of the SAL~~. These flights headed to the northeast in order to encounter heavy dust loads ~~nearer~~ closer to the African coast on 12 August. Flight b920 was conducted near to the Cape Verde archipelago and co-located with the path of the International Space Station (ISS), in order to fully characterise the SAL and validate the Cloud-Aerosol Transport System (CATS) remote sensing lidar instrument onboard the ISS.

Each flight consists of a combination of sloped profiles (abbreviated to ‘P’, e.g. ‘P1’) and straight-and-level ~~flight legs~~runs (known as ‘SLRs’ and abbreviated to ‘R’, e.g. ‘R2’) at various altitudes, generally selected to be within the aerosol layer of

interest, or at altitudes appropriate for radiometric measurements. Here we present results from 31 profiles and 19 in -situ aerosol sampling ~~legs~~SLRs, as shown in Figure 1~~Figure 1b~~. Five ~~legs~~ SLRs were performed in the marine boundary layer (MBL) at 30 to 35 m above sea level (one per flight), and 14 ~~legs~~ SLRs sampled the SAL at altitudes between 1.8 to 4.1 km. Exceptions were an intermediate layer sampled during flight b920 containing dust at 1.2 km, and heavy dust sampled during flight b924 at 920 m. Full information about profile and SLR times and altitude are available from the Centre for Environmental Data Analysis (see Data Availability).

2.2 Determination of Dust Sources and Dust Age

Broad geographic dust source locations, where dust was uplifted before being sampled by the aircraft during AER-D, have been identified using Spinning Enhanced Visible and Infrared Imager (SEVIRI) 'dust RGB' (red-green-blue) thermal infrared satellite imagery product (Lensky and Rosenfeld, 2008), where dust events are identifiable by their bright pink colour (e.g. Brindley et al. (2012)). Dust events sampled by the aircraft are tracked backwards in time visually until uplift times and locations are identified, identical to Ryder et al. (2013b). The high temporal resolution (15 min) of the imagery enables easier tracking compared to other spaceborne sensors which may have only two overpasses per day. However, this method is subjective, and therefore we allow generous errors in terms of geographic dust uplift location, and dust uplift time. Additionally, no height resolution information is available from the imagery, so source areas are categorized for each flight, and not for each sampling altitude within flights.

Examination of the dust events sampled during AER-D reveals that the dust in every event was initially uplifted by a mesoscale convective system (MCS) and a resultant cold pool (haboob) which spread out radially. This is in keeping with recent findings that cold pools are the dominant mechanism for summertime Saharan dust uplift (Marsham et al., 2013; Allen et al., 2013). The dust events then took 1 to 5 days to reach the Atlantic Ocean where they were sampled by the aircraft. In three cases, additional uplift events could be observed merging with the initial dust event, and in these cases error bounds on dust age were set to include all possible uplift events, and were therefore very broad. In most cases, convection and clouds could be observed developing over the SAL during the afternoon in the top of the dust layers during their transport. Therefore it is possible that the dust observed has been processed by clouds (e.g. Ryder et al. (2015) Section 4.1.4; Diaz-Hernandez and Sanchez-Navas (2016)), though no clouds were present when sampling took place.

The SEVIRI imagery is not able to give altitude-resolved information, and can be subjective, particularly when dust loadings are light, at low altitude or in a moist environment, making dust appear less pink and more difficult to identify (Brindley et al., 2012). This is more evident in the dust tracked for flights b932 and b934 where dust loadings were lower. This introduces a~~n unquantified~~ small level of uncertainty into both the source locations and dust ages, which we account for by giving generous error bars to the dust uplift times and source locations. HYSPLIT back trajectories (Draxler and Hess, 1998; Stein et al., 2015) were also run~~,~~ for the AER-D dust events.~~ but are not used to determine source location or age here~~ In only one of the five dust

events was the dust source location similar to that observed in the SEVIRI imagery.~~,~~ ~~since~~ ~~I~~in every case ~~they~~the back trajectories indicated a transport path and transport time differen~~ting from~~ to that shown by the SEVIRI imagery. Although the SEVIRI methodology has its limitations, the back trajectory method results were clearly not compatible with the information from SEVIRI. Therefore back trajectories are not used to determine source location or age here. Additionally, another limitation of back trajectories is that they only indicate when an air mass nears the surface, but do not reflect potential uplift conditions (e.g. surface wind strength or soil conditions). It has been shown that models and reanalyses are currently unable to adequately represent convective events and winds over the Sahara and Sahel, particularly due to the challenges of representing cold pools. For example, Garcia-Carreras et al. (2013) examine the role of convective cold pools and suggest that "the misrepresentation of moist convective processes can affect continental-scale biases, altering the West African monsoon circulation." Many other publications have examined the misrepresentation of Saharan convective events (Marsham et al., 2011; Heinold et al., 2009; Sodemann et al., 2015; Trzeciak et al., 2017; Allen et al., 2015; Roberts et al., 2017; Engelstaedter et al., 2015).~~,~~ ~~which~~ Since convective events are the drivers of dust uplift in all the AER-D cases~~.~~ ~~Therefore~~ we do not consider HYSPLIT back trajectories (with relatively low model resolution of ~~one~~ half a degree) to be informative ~~in these cases~~here due to the challenges the models face in representing Saharan circulation. Finally, we~~,~~ ~~and~~ note that ~~they~~ back trajectories are recommended ~~should~~ to be used with caution for dust events over the summertime Sahara (Trzeciak et al., 2017).

2.3 Instrumentation

Much of the instrumentation operated during ICE-D was identical to that operated during the Fennec campaign, described in Ryder et al. (2013b) and Ryder et al. (2015). Relevant information is provided below, noting where instruments and processing differed. Throughout this article all particle sizes are referred to in terms of diameter (d), and optical properties are presented at 550 nm unless stated otherwise.

2.3.1 Inlets, Scattering and Absorption Measurements

~~Scattering~~ Scattering measurements were made by a TSI 3563 integrating nephelometer (at wavelengths of 450, 550 and 700 nm). ~~and a~~Absorption measurements were made by a ~~TSI 3563 integrating nephelometer and a~~ Radiance Research Particle Soot Absorption Photometer (PSAP)~~,~~ at ~~wavelengths of 450, 550 and 700 and~~ 567 nm ~~respectively~~. Both instruments are situated inside the aircraft cabin, behind a modified Rosemount 102E inlet. PSAP filters were changed before every flight and spot size was measured. Standard corrections are performed on both instruments. For the PSAP these are taken from ~~according to~~ Turnbull (2010) ~~for the PSAP~~, which incorporates corrections necessary to the FAAM PSAP measurements based on the original work by Bond et al. (1999), and further clarifications to this publication described by Ogren (2010). For the nephelometer corrections are performed according to ~~and~~ Anderson and Ogren (1998) assuming supermicron particles.~~,~~ This result~~sing~~ in 11% and 15% uncertainty in extinction and single scattering albedo (SSA) respectively (Ryder et al., 2013b). Corrections for internal nephelometer temperature and pressure are included.

Accumulation mode AODs are calculated from aircraft profiles by integrating the scattering and absorption measurements between the minimum aircraft altitude (typically around 30 m above sea level) to the top of the profile (typically around 6 km). Therefore AODs represent both SAL and MBL aerosol.

Extensive experimental and theoretical efforts to characterize inlet and pipe losses were performed during Fennec (Trembath, 2012; Ryder et al., 2013b), and we apply those results here. It was found that the net impact of both Rosemount inlets and pipework supplying the nephelometer and PSAP led to number concentration enhancements by a factor of 1.5 for d<1.5µm, no net loss or enhancement at 2.5µm, net losses between 2.5 to 5 µm (50% efficiency at 3.5±0.5 µm), and no particles larger than 5 µm sampled. The exact enhancement and losses vary between the nephelometer and PSAP (slightly different pipework) and with altitude (see Supplement Figure S1). Since it is clear that coarse mode particles do not reach the nephelometer and PSAP, henceforward the term 'accumulation mode' is used to describe the size distribution arriving at these two instruments, roughly representing particles sized d<2.5 µm. The enhancement and loss factors as a function of diameter are applied to the size distribution described in Section 2.3.2 in order to replicate the accumulation mode size distributions reaching the nephelometer and PSAP.

2.3.2 Size Distribution Measurements

We present size distribution measurements from a combination of different wing-mounted instruments as shown in ~~Table 2~~Table 3. We utilize optical particle counter techniques for the accumulation and coarse modes (Passive Cavity Aerosol Spectrometer Probe (PCASP) and Cloud Droplet Probe (CDP)), and light shadowing measurement techniques for the giant mode (Two-Dimensional Stereo Probe (2D-S), Cloud Imaging Probe 15 (CIP15), Cloud Imaging Probe 100 (CIP100)). Size distributions are also provided for some ~~flight legs~~ SLRs from filter sample analysis (Section 2.4). This range of instrumentation allows us to take advantage of measuring a wide ~~aerosol~~ particle size range (0.1 to 6200 µm), though the processing and uncertainties associated with each must be considered carefully, as follows. Uncertainties due to flow distortion effects are not considered.

The PCASP was calibrated before and after the campaign, and the CDP was calibrated and cleaned before most flights during the campaign as described in Rosenberg et al. (2012). The PCASP and CDP employ light scattering in order to determine particle size, thus the nominal size bins have been adjusted for a refractive index (RI) of dust of 1.53 – 0.001i, informed by the refractive index closure results from Section 2.5, using the CStoDConverter software (Rosenberg et al., 2012). This results in an increase in diameter of the largest size bins due to the more absorbing imaginary part of the refractive index as compared to PSL (polystyrene latex) used in the manufacturer's calibrations. The software also provides uncertainties in the bin centres and bin widths due to oscillations in the Mie scattering curve, which can cause ~~singularities~~ ambiguities in the scattering–size relationship. This propagation of errors allows us to utilize data from the full size range while still maintaining a measure of the sizing uncertainty, and can be seen by horizontal error bars in Figure 2. The larger errors around diameters of 3.5 and 20

microns, for example, relate to inflection points on the Mie scattering curves. These horizontal sizing errors are propagated through to calculations of number and volume size distribution errors. The first size bins are removed for both the PCASP and CDP since the lower edges are not well defined.

In a similar manner to Fennec, custom bin widths were set for the CDP. The smallest bin of the CDP was set much wider than standard, with a lower minimum detection threshold in order to increase sensitivity to smaller particles, and subsequent processing of the particle-by-particle data allowed the smallest size bin to be split into 4 sub-bins. As a result, the bin sizes of the CDP increase due to the refractive index correction, but the size resolution at the small end of the spectrum is retained due to the custom bin specifications. This prevents too much of a gap developing between the PCASP and CDP size ranges, with the first 4 size bins covering 3.36-3.87, 3.76-4.18, 4.35-4.81, 4.74-5.36 µm. Note that the bin sizes overlap due to the method used to determine bin edges in CStoDConverter.

Bin sizes also depend on the choice of refractive index applied. In this work, a complex refractive index ~~at 550 nm~~ ($n^{550} = m^{550} - ik^{550}$) of 1.53-0.001i was used to determine the PCASP and CDP bin sizes, as determined from Section 2.5, for 550 nm. Since the PCASP and CDP operate at wavelengths of 633 and 658 nm, we assume a constant refractive index across these wavelengths. This is supported by the relatively flat spectral refractive index shape at these wavelengths indicated in Figure S2. As additional sensitivity tests, size distributions were also computed using a real part, m^{550}, of 1.48 and 1.58 (1.53±0.05), and imaginary parts, k^{550}, of 0.002~~i~~, 0.003~~i~~ and 0.006~~i~~. Particle sizes determined from the PCASP and CDP represent optically equivalent diameters. Sensitivity in effective diameter (d_{eff}) to these changes from m^{550} were less than 0.2 µm (<5%), and from changes in k^{550} were less than 0.9 µm (<20%). However, within the likely range of k^{550} (0.001 – 0.002~~i~~) as derived in Section 2.5, changes in d_{eff} were < 0.1 µm (<3%). Therefore we consider the uncertainty in d_{eff} to refractive index to be a maximum of 5% reflecting the uncertainty due to likely values of both m and k.

The Optical Array Probes (OAPs: CIP15, CIP100, 2DS) measure particles in two perpendicular directions: the first aligned with the photodiode array (x) and the second along the direction of aircraft motion (y), Thus providing a two-dimensional projection of a particle (McFarquhar et al., 2017). Although the OAPs do not require assumptions about refractive index to derive size, they can be subject to several systematic uncertainties associated with the processing/sizing method (McFarquhar et al., 2017). Thus to investigate some of these uncertainties, the 2DS data was processed in two different ways, using two different sizing metrics.

Firstly, data from all three OAPs were processed using the System for OAP Data Analysis (SODA-2) developed at NCAR. The SODA-2 removes out of focus images and various instrument artefacts including accounting for a stuck diode in the middle of the CIP-100 array. A ‘centre-in’ method was applied where particles are only counted when the centre of the particle falls within the photodiode array. The particle size was defined as the diameter of the smallest circle enclosing the particle

(denoted 'CC' – circumscribing circle), and thus for non-spherical particles may lead to an overestimate in particle size. Secondly, data from the 2DS instrument were analysed using the Optical Array Shadow Imaging Software (OASIS), developed by the National Centre for Atmospheric Science (NCAS) and DMT. Particle sizes were calculated using the mean of the x and y dimensions of each particle image (denoted 'XY') using an 'all-in' method where particles are only counted when they fall completely within the photodiode array. The x and y dimensions are measured along the probe array, i.e. the particle is not rotated to minimize or maximize either dimension.

The mean XY method is considered to give a more representative diameter for non-spherical particles than the CC metric, ~~though~~ Area-equivalent diameters were not calculated because particles can sometimes appear hollow on the OAPs (McFarquhar et al., 2017) which would lead to undersizing. If the particle image is an ellipse, the mean XY diameter~~s~~ will be ~~lower~~ larger than an ellipse area-equivalent diameter, as used by the filter sample analysis for example ~~for example, if the particle is an ellipse~~. However, the OAP images capture 2-D image projections of the particles in their atmospheric orientation, while the filter samples are will be collected with their largest surface lying parallel to the filter sample, and therefore may be oversized in this context. An additional motivation for testing this second processing option for the 2DS was for comparison with Fennec data (Ryder et al., 2013b) which were processed using an all-in, mean XY method for the CIP15.

Since particles detected by the 2DS during AER-D mostly cover 1-7 pixels, the impact of centre-in versus all-in is considered small. The sample area is adjusted for the effective array width, which is different depending on whether 'all-in' or 'centre-in' is used (McFarquhar et al., 2017), and therefore the calculated number concentrations account for this. ~~Instead, t~~The sizing metric (i.e. XY versus CC) has the greatest impact on the final size distribution. Smallest and largest size bins were removed for the OAP data, and data was excluded for size bins in ~~flight legs~~SLRs where fewer than 4 particles were detected as an additional measure for removing noise (equating to number concentrations of around 10^{-5}cm^{-3} for the 2DS and CIP15 for typical sampling times of around 20 minutes, or 132 km on the BAe146). The CIP100 suffered from noise and did not detect any particles within its size range (d>200 µm following exclusion of the first size bin).

Uncertainties in number concentration for all size probes are propagated from 1Hz measurements, through to means over ~~legs~~SLRs, through to the AER-D campaign averages. For all probes, random errors (due to counting and discretization error) and systematic errors (due to sample area uncertainty and bin size centre and width from Mie singularities) were accounted for in their contribution to total number concentration errors, and propagated ~~appropriately~~by standard analytical error propagation. I.e. random error can be minimized by increasing the sample size (averaging across the campaign), while systematic error remains constant. For the CDP at d < 20 µm bin size uncertainty was found to dominate the total uncertainty in dN/dlogD and dV/dlogD. Horizontal error bars in Figure 2 represent the maximum uncertainty in bin edges, derived from uncertainties in both bin centre and bin width. Uncertainties in bin size contribute to uncertainties in both dN/dlogD and dV/dlogD, and therefore the relative uncertainties do not change significantly between the two panels. All error bars represent

maximum uncertainty. ~~In calculations of number and volume size distribution, errors due to bin size from refractive index corrections were also incorporated for the optical probes.~~

Figure 2 shows an instrument comparison for the five instruments for the mean size distribution in the SAL. It can be seen that the CIP15 and 2DS cover similar size ranges, and the CDP overlaps both of these instruments at the smallest size bins. However, different number concentrations are detected by the CIP15 and 2DS, which becomes more evident as size approaches 100 µm. Greater number and volume distributions are seen from the CIP15 than the 2DS, although when the same processing and sizing assumptions are used (CIP15 CC, blue, and 2DS CC, orange), the size distributions agree within error bars. The 2DS XY processing (green) results in a lower number distribution and a smaller maximum size, as expected for non-spherical dust ~~when the~~ particles ~~are non-spherical~~ (section 3.2) because the CC metric will oversize a non-spherical particle. Therefore several choices are made in terms of how best to use data from each instrument in the analysis of size distributions and subsequent optical properties, as follows. We use the full size range of the PCASP for the accumulation mode, for the coarse mode the CDP is used up to 20 µm, and the giant mode is taken from the 2DS XY processing and metric since this is a better metric for non-spherical dust particles, and also consistent with the Fennec data processing. This size distribution is referred to as 'FULL PSD.'

Size distributions are summarized ~~using~~ with commonly used metrics of effective diameter, d_{eff}, ~~(~~(Hansen and Travis, 1974) (sometimes known as the volume-surface diameter, Hinds (1999))~~e.g. defined in Ryder et al., 2013b)~~, and volume median diameter (VMD, the diameter below which half of the volume size distribution lies, (Seinfeld and Pandis, 2006)). Additionally we present the maximum size detected, d_{max}, by the 2DS XY as a useful metric of the largest size present in the atmosphere. Weinzierl et al. (2009; 2011) present maximum size measured at a concentration above 10^{-2}cm^{-3}. Here we choose to simply present the maximum particle size detected, since the number concentration detected depends on the width of the size bin employed by the particular instrument operated and is not directly comparable. The sizing instruments operated during AER-D do not have a minimum detection concentration level, but at low particle concentrations the sampling statistics simply become poor, introducing an effective detection limit. Therefore we remove cases where fewer than 4 particles are detected over a ~~flight leg~~SLR as previously mentioned, with an implicit effect of removing data where concentrations are lower than 10^{-5}cm^{-3} for the 2DS and CIP15.

Some CIP15 AER-D data were also processed using a centre-in, mean XY metric, but unfortunately it was not possible to process data for all the SLRs with this method. Therefore this data was used to inform on instrumental differences between the 2DS and CIP15 when processed with the same size metric (XY mean). It was found that the impact on the full PSD was very small (d_{eff} differed by under 1%), but that d_{max} was up to 6% larger with the CIP15 XY compared to the 2DS XY. The upper uncertainty of 6% in d_{max} was therefore propagated in combination with the other uncertainties in d_{max}.

2.3.3 Size Distribution behind Rosemount Inlets

In addition to the main size distribution combination described above, a further size distribution is calculated in order to represent the size distribution reaching the nephelometer and PSAP, accounting for inlet enhancements and losses as well as pipe losses (Trembath, 2012; Ryder et al., 2013b). In order to do this, the 'FULL PSD' ~~size distribution~~ is adjusted for the size-resolved, height dependent, loss or enhancement as shown in Supplement Figure S1. Since particles larger than 5 µm diameter do not reach the nephelometer or PSAP, the choice of instrument at sizes larger than this is irrelevant. There is a net loss of particles at d > 2 ~~to~~ 3 µm and an enhancement of the number of particles in the accumulation mode at d < 2-3 µm. ~~diameters of around 0.2 to 1 µm.~~ We term this size distribution 'ACC PSD' since it predominantly represents the accumulation mode.

2.3.4 Filter Sample Collection

Aerosol filter samples were collected using the FAAM airborne filter collection system (Andreae et al., 2000; Formenti et al., 2008; McConnell et al., 2010) behind a separate inlet dedicated to filter samples (i.e. different to the Rosemount inlets). This is the same inlet used to collect ice nuclei particle samples presented in Price et al. (2018), in many cases samples were collected in parallel. The inlet passing efficiency has not been formally determined, though Andreae et al. (2000) found that while mounted on the previous C-130 aircraft, the same filters inlet restricted measurements to 35% of the coarse mode mass (defined as d>1.4 µm) in sea salt aerosol compared to ground-based observations. Further details are available in Price et al. (2018).

Aerosol particles were sampled by filtration onto a stacked-filter unit (SFU) with three stages, though only one stage was used in AER-D. Aerosols were collected on 47mm diameter Nucleopore filters with pore sizes of 0.2 or 0.4 µm using either a standard plastic filter holder as used previously (e.g. Formenti et al. (2008)) or on a newly developed adjusted plastic filter holder with a lip on the edge removed for ease of loading. Depending on the holder and pore size used, different support grids were used – either plastic, Millipore fine mesh metal, or JSHoldings coarse mesh metal. In total 22 filter samples were collected during AER-D flights, although problems were encountered with many samples ranging from difficulties mounting and removing the support grids into the old filter holder, very low flow rates when combining the 0.2 µm Nucleopore pore sizes and Millipore grid, and unexplained silicon contamination on some samples. As a result, many of the filter samples did not display the expected number of particles upon laboratory analysis. Therefore we were forced to discard many samples, and four samples of the best data were analysed for size, shape and chemical composition analysis: 2 ~~flight legs~~SLRs in the MBL (b920 R2, b928 R2) and 2 ~~legs~~ SLRs in the SAL (b920 R5, b932 R6), in order to give a snapshot of these properties during AER-D.

2.4 Filter Sample Analysis

Filter samples were analysed by Scanning Electron Microscopy (SEM, instrument model JEOL JSM 6301F) coupled to an X-ray energy-dispersive spectrometer (Silicon Drift X-Max 80 mm^2 Detector and Aztec Advanced-INCA350 analyzer, Oxford

Instruments) to provide information on the coarse and fine fractions respectively. Analysis was performed on a portion of filter cut and mounted on an aluminum stub using a double-sided adhesive and then covered with a thin film of Platinium (Pt) by sputter coating (Jeol JFC 1100E). Particles were found to be evenly distributed across the filter sample. Images were acquired by a series of transects at two magnifications (×2,000 (55.9 nm/pixel) and ×10,000 (11.0 nm/pixel)), scanning between 397 to 1116 particles per sample.

Particles were sized by processing the SEM images, which are essentially 2-D projections of 3-D particles. The 2-D projections were fitted with a circumscribed ellipse, to produce an ellipse area-equivalent diameter, where the major and minor axes (d_{max} and d_{min}) are used to define the particle diameter d according to $d=(d_{max}d_{min})^{1/2}$. The aspect ratio was accordingly calculated using d_{max}/d_{min}~~.~~ .

It was not possible to use automated image contrast to calculate projected particle area because of a high degree of variability in particle contrast. ~~Note~~ Our filters sizing ~~that~~ this technique may oversize the particle size for two reasons. Firstly, the area of a fitted ellipse may be larger than a projected particle area, though the particles were not noticeably jagged around their edges. Secondly, our method may oversize particle volume~~, particularly~~ where the shape is a platy silicate ~~with a~~ and has a tendency to fall with its largest surface parallel to the substrate. For example,~~; e.g.~~ Chou et al. (2008) found the height of dust particles examined under SEM to be around one third of their major axis length. Additionally, we tested the sensitivity of the filters PSD to using the mean XY and CC sizing methods applied to the OAP data (not shown). Using a mean XY method on the filters data did not produce significantly different results, while using the CC method was found to shift the PSD towards larger particles, similar to the findings from the OAP size metric comparisons.

Semi-quantitative elemental chemical analyses integrate the following elements: Na, Mg, Al, Si, P, S, Cl, K, Ca, Ti, Mn, and Fe . The results are expressed as a weight percentage of the associated oxides (Na_2O, MgO, Al_2O_3, SiO_2, P_2O_5, SO_3, Cl, K_2O, CaO, TiO_2, MnO, Fe_2O_3) normalized to 100%. The composition type of each particle is then identified based on these percentages into one of the following categories: alumino-silicates, quartz, sulfate, salt, thenardite, gypsum, Ca-rich, Ti-rich, Fe-rich and others. These are interpretations based on the elementary chemical analysis. E.g. if we observe the simultaneous presence of calcium and sulphur (typically within 10% of one another), this could be several possible minerals: a~~A~~nhydrite ($CaSO_4$), b~~B~~assanite ($CaSO_4 \cdot 0.5(H_2O)$) and g~~G~~ypsum ($CaSO_4$, $2H_2O$), though the most probable atmospheric form is gypsum. Sulfate is classified by the dominance of SO_3. Thenardite is classified when both Na_2O and SO_3 are dominant. Salt is classified by percentages of both Na_2O and Cl being high, indicating halite particles of marine origin. Alumino-silicates, quartz, thenardite, gypsum and Fe-rich particles indicate terrigenous particles in these cases. Only one black carbon chain-like structure was observed during the analysis of over 6500 particles, and therefore this aerosol category is not included.

Although particles may frequently be a mix of several composition types, they were classified according to their ~~dominant~~ component type which made up the greatest oxide percentage. This may particularly be an important assumption regarding the iron component, which was consistently present in small amounts on most particle types but only classified as iron when iron was the dominant component; i.e. in general when iron oxide constituted over 50% of the composition. More complex methods of accounting for iron as a minor component are possible (e.g. Kandler et al. (2011a); Balkanski et al. (2007) but are beyond the scope of this work. Although composition information is available for all particles sampled under magnifications of ×2,000, many particles sampled under the high magnification did not provide a strong enough signal to provide composition data. Thus the number of particles available for composition analysis in the fine fraction is much lower than that for the coarse fraction.

Filter sample analyses use subsets of data from each magnification in order to take advantage of the best counting statistics for each size range and optimal viewing at each magnification. Filter sample size distributions are calculated using fairly finely resolved size bins from 0.05 to 40 µm as shown in Figure 7. However, at each magnification, sensitivity to the smallest particles detected is low due to a low SEM signal (fewer photons emitted for smaller volume particles). Therefore~~, so~~ particles smaller than 0.1 and 0.5 µm are excluded for ×2,000 and ×10,000 respectively. Additionally, for the ×10,000 magnification, not many particles larger than 1 µm are counted in comparison to ×2,000, so particles larger than 1 µm are also excluded.

For aspect ratio, composition and refractive index analyses, particles sized 0.1 to 0.5 µm are taken from the ×10,000 magnification, while particles sized between 0.5 to 40 µm are taken from the ×2,000 magnification, and scaled appropriately to account for the different substrate area examined under the different magnifications. Size resolved composition data utilizes six size bins with edges at 0.1, 0.5, 1.0, 2.5, 5, 10 and 40 µm. Information for the full filters size distribution accordingly covers 0.1 to 40 µm. Additionally, bulk filter sample properties are calculated specifically for the accumulation mode, covering diameters 0.1 to 2.5 µm, in order to replicate the in-cabin measurements behind the Rosemount inlets, and also for the bulk sample from 0.1-40 µm to cover the full size distribution. Aspect ratios are presented as number fractions; composition is presented as volume fraction.

2.5 Derivation of Refractive Index

2.5.1 Refractive Index Iterated from Optical and Size Measurements

In order to determine the accumulation mode refractive index for each individual ~~flight leg~~SLR, measurements of scattering and absorption from the nephelometer and PSAP are used in combination with Mie scattering code, taking input from the measured size distributions. Since the nephelometer and PSAP only measure scattering and absorption from the accumulation mode due to inlet effects, the refractive indices derived only represent the accumulation mode up to 2.5 µm, and not the coarse mode. The method is identical to that described in Ryder et al. (2013b): a Mie scattering code is used to generate optical properties at 550 nm, using the ACC PSD, with refractive index of m^{550}=1.53 and k^{550} incrementing in steps of 0.0005 from

0.0005 to 0.006, but with ~~ranging from 0.0001 to 0.006i, in increments of 0.0005i, except for~~ an additional smallest value of 0.0001~~i~~ which was required for the MBL ~~legs~~SLRs. The value of k^{550} which produced best agreement with the SSA from the nephelometer and PSAP was selected for each ~~flight leg~~SLR. ~~Values are shown in Figure 8b.~~ The resulting values of k^{550} are shown in Figure 3, with modal values of 0.001i for SAL ~~legs~~SLRs and 0.0001i for MBL ~~legs~~SLRs. This set of refractive index data is referred to hereafter as the 'iterated refractive indices.'

The derived iterated refractive indices were then used in two ways. Firstly, a value of 1.53-0.001i was used to correct all size distributions from the PCASP and CDP. Secondly, iterated refractive indices derived for each ~~flight leg~~SLR were selected to generate optical properties for the FULL PSD and ACC PSD described in Section 2.6~~ 2.3.2~~. ~~Composition, and therefore k^{550}, is assumed to remain constant with particle size so that the derived refractive index for the accumulation mode can be applied to the full size distribution. For all cases m^{550} was assumed to be 1.53, and for the MBL k^{550} varied between 0.0001 to 0.0005i, and for the SAL k^{550} varied between 0.0015i to 0.0025i.~~

2.5.2 Refractive Index from Filter Samples

~~Firstly, we~~We use the composition volume fraction and spectral refractive index data of 7 aerosol/mineral components in order to compute refractive indices. These are alumino-silicates, quartz, carbonates, gypsum, iron-rich, sodium chloride (sea salt) and sulfate-rich. Alumino-silicate is represented by a mean of illite and kaolinite refractive indices, carbonates by calcite refractive indices, and iron-rich by a mean of hematite and goethite refractive indices. Sea-salt is represented ~~a~~with~~s~~ NaCl refractive indices. The sulfate-rich category is represented by ammonium sulfate refractive indices, assumed to be the most likely atmospheric composition. Thenardite is also included in ~~this~~ the sulfate-rich category as no refractive index data are available for it, similar to Kandler et al. (2009). Literature data was taken as follows: illite (Egan and Hilgeman, 1979; Querry, 1987), kaolinite (Egan and Hilgeman, 1979; Glotch et al., 2007), quartz (Shettle and Fenn, 1979; Peterson and Weinman, 1969), calcite (Querry et al., 1978; Long et al., 1993), gypsum (Long et al., 1993), hematite (Shettle and Fenn, 1979; Bedidi and Cervelle, 1993; Marra et al., 2005), goethite (Bedidi and Cervelle, 1993; Glotch and Rossman, 2009), sodium chloride (Toon et al., 1976), ammonium sulfate (Toon et al., 1976). Where no spectral data are available, values are linearly interpolated across wavelengths. Refractive indices are then calculated by weighting each mineral component by its volume fraction given from the composition analysis in Section 2.4, a method which assumes that particles are internally, homogenously mixed. Although it was evident from the SEM analysis that the particles are externally mixed, and it is known that internal and external mixing can result in different optical properties (McConnell et al., 2010).~~,~~ ~~w~~We employ this method partly for simplicity and partly for consistency with previous work (e.g. Kandler et al. (2009; 2011a); Klaver et al. (2011); Formenti et al. (2014). These refractive indices are then used with the size distribution data from the wing probes to generate optical properties using Mie scattering code.

~~Secondly, we calculate optical properties from the composition data using an external mixing assumption. In this case, size distributions of each mineral component are calculated by weighting the size distribution from the wing probes for each mineral component using its number fraction. Scattering properties for the size distribution of each mineral are then computed using Mie scattering code and the same literature refractive indices as described above. Summing scattering and absorption over all minerals then provides the total optical properties for the external mixing case.~~

2.6 Calculation of Optical Properties

Optical properties (SSA, MEC and g) are calculated using a Mie scattering code, where dust particles are assumed to be spheres. Size distributions used are taken from the wing probes, representing either the FULL PSD or the ACC PSD. Refractive indices are taken from either the iterated RI method (Section 2.5.1) or from internal or external mixing RI values calculated from the filter samples (Section 2.5.2).

When the iterated RI values are used, composition, and therefore k^{550}, is assumed to remain constant with particle size. This allows the iterated RI for the accumulation mode to be applied to the full size distribution. For all cases m^{550} was assumed to be 1.53. Iterated values of k^{550} specific to each SLR were used. For the MBL k^{550} varied between 0.0001 to 0.0005, and for the SAL k^{550} varied between 0.0005 to 0.0025 (as shown in Figure 3). Although a value of 1.53 for m^{550} is higher than that produced by the filter sample composition results (Section 3.5, 1.47-1.49) the filters result is likely biased low due to the reasons discussed in Section 3.5. We also performed a sensitivity test to using m^{550} of 1.48 and 1.58, and found that d_{eff} changed by up to 5% and SSA by under 1%.

Where composition from filter samples are used, RI is allowed to vary as a function of particle size according to the composition results. For internal mixing assumptions the refractive indices calculated according to Section 2.5.2 are used. ~~Secondly~~For external mixing assumptions, ~~we calculate optical properties from the composition data using an external mixing assumption. In this case,~~ size distributions of each mineral component are calculated by weighting the size distribution from the wing probes for each mineral component using its number fraction. Scattering properties for the size distribution of each mineral are then computed using Mie scattering code and the same literature refractive indices as described above. Summing scattering and absorption over all minerals then provides the total optical properties for the external mixing case.

Although it is clear that dust particles are not spherical, sensitivity of SSA to shape was tested by Otto et al. (2009) and Johnson and Osborne (2011), who found that SSA changed by under 1% and 2% respectively when non-spherical particles were assumed. This is less than our uncertainty in SSA of 5% due given above due to refractive index, and therefore we consider this an acceptable assumption.

3 Results

3.1 Dust Sources and Vertical Structure

Figure 1 shows the dust uplift locations (sources) determined using SEVIRI RGB imagery for dust sampled during each AER-D flight. ~~Table 3~~ Table 4 shows the corresponding meteorological event driving the uplift, and also the age of dust when sampled by the aircraft. Dust sampled by the first two flights, b920 and b923/924 originated from large scale dust events uplifted in easily identifiable single events. The b920 dust was uplifted over southern Algeria (blue circle in Figure 1), and subsequently transported northwards and then westwards.~~,~~ The dust emerged~~ing~~ over the Atlantic from southern Morocco, being sampled by the aircraft after around 4 days' transport. The b923/b924 dust was uplifted further west, over northern Mali (green oval in Figure 1), and was also subsequently transported northwestwards, emerging over the Atlantic over southern Morocco and sampled by the aircraft after a shorter time of 2 days due to the more direct transport path.

During the days leading up to flight b928, there was a change in the dominant meteorological dust export mechanism, as described by Liu et al. (2018). First, dust was uplifted over northern Mauritania (orange circle number 1) underneath widespread altocumulus cloud, which moved slowly to the southwest. Here, it became mixed with dust which had originated from northern Mali (orange circle number 2) where it had been uplifted by an MCS and haboob. This~~,~~ ~~which~~ moved rapidly westwards, driven by strengthened 700 mb winds, which characterized the second phase of ICE-D (Liu et al., 2018). The two dust events became mixed together and subsequently transported dust over the Atlantic via the Mauritanian coastline, thus taking a more direct southerly transport route than the dust exported and sampled by the first two flights of the campaign (b920 and b924). Thus the dust sampled during b928 was a mixture of dust from two different source regions. The final two flights, b932 and b934, consist of dust uplift events which subsequently overpassed secondary (or tertiary) uplift events, and are therefore considered as dust from a mixture of the identified sources. The dust sampled during b932 was initially uplifted by a MCS and haboob close to the Mali/Algerian border, and some small scale reinvigorated convection caused additional uplift over northern Mali, before the dust was transported southwestwards towards the Mauritanian coastline. Dust encountered during b934 was also initially uplifted in almost the same region along the Mali/Algeria border by a MCS and haboob, and on each subsequent evening a new convective cell developed over the transported dust with a new haboob – over the Mali/Mauritanian border (purple circle number 2), and then over western Mauritania (purple circle number 3). Therefore the range of possible dust ages for b934 is very large (16 hours to 3 days). The range of sources identified during AER-D are consistent with well-known source regions in the literature (Engelstaedter et al., 2006; Formenti et al., 2011; Evan et al., 2016; Scheuvens et al., 2013), particularly the Mali/Algeria border hotspot downwind of the gap between the Atlas and Ahaggar Mountains (Potential Source Area 3 in Formenti et al. (2011)), which contributed to 4 of the 5 AER-D dust events.

Figure 4 shows the vertical structure of the five dust events sampled during AER-D from in-situ aircraft measurements. Four events (b920, b928, b932 and b934) display typical SAL structure, with elevated dust from a base of between 0.5 to 1.5 km up

to an upper bound of 5 km (6 km in one case) overlying the MBL. Accumulation mode e~~E~~xtinction coefficients vary from around 100 to 500 Mm^{-1} in this layer, sometimes with fairly constant values in the vertical (b920, b934)~~,~~ ~~a~~At other ~~times displaying more sinuous~~ layers were more sinuous (b932, b928), but always ~~with~~ had accumulation mode scattering angstrom exponents (SAE; 700 to 450 nm) of fairly constant value around -0.5 – a clear indication of coarser particles. Within the SAL, water vapour mixing ratios were low (under 10 g/kg) and potential temperature increase~~d~~s slowly with altitude. Relative humidities were low at 30-50% at altitudes where ~~horizontal legs~~SLRs were performed. Contrastingly, in the MBL relative humidities were high (>90%) as expected, with the MBL capped by a temperature inversion. SAE values in the MBL were variable, sometimes exhibiting a jump to positive values (b920, b934) suggesting a dominance of smaller particles, whereas sometimes hardly displaying any difference to the overlying dust (b928, b932). In the former two cases, the PCASP size distribution confirms a greater relative contribution from fine (d<0.3µm) particles in comparison to those sized 0.3 to 3 µm. This vertical structure is as expected for the region in summer, and in keeping with the elevated and dusty SAL above the MBL (Prospero and Carlson, 1972).

In contrast, the dust event sampled on flights b923 and b924 displays very large dust loadings and different vertical structure. The upper SAL, from 2.5 to 5 km, displays roughly constant potential temperature and water vapour mixing ratio, with extinction coefficients of around 140 Mm^{-1}. Between 0.5 to 2.5 km, dust loadings become extremely high reaching 2122 Mm^{-1} at 1.2 km, contributing to the very high AOD of 2.54 for the accumulation mode only (including coarse particles would increase the estimated AOD further). To the authors' knowledge, this is the highest aircraft-measured value of dust-related extinction measured for dust transported over the ocean, and is explored further by Marenco et al. (2018, in review). (Note that lidar-derived AODs and extinction shown by (Marenco et al., 2018, in review) are slightly lower than those shown here, which may be due to different extinction properties of the dust at the lidar wavelength of 355 nm, the Rosemount inlet enhancement effects shown in Figure S2, or the differences between a lidar curtain and sloped aircraft in-situ profile). Moisture levels here ~~increase~~ decrease with decreasing altitude (8-12 gkg^{-1}) and are larger than observed within dust during the other flights. The higher levels of moisture are perhaps not surprising given that a MCS-haboob uplifted this dust two days earlier, and one day earlier Saharan Boundary Layer (SABL) convection can be seen impacting the dust over northern Mauritania (consistent with Marsham et al. (2013); and recycling of moisture within the dusty SABL in Ryder et al. (2015)). Note that these values of extinction do not include the coarse mode, and therefore actual extinction values will be even higher. Beneath the thick, low altitude dust layer~~,~~ was a shallow MBL extending up to 500 m. This unusual vertical structure of intense, thick dust within the bottom half of the SAL is not in keeping with the conventional SAL model (Prospero and Carlson, 1972) of well-mixed elevated dust throughout the whole SAL, and is therefore of additional interest. This is discussed in detail by Marenco et al. (2018, in review).

3.2 Size distributions and shape

Figure 5 shows the wing-probe size distributions for each ~~flight leg~~SLR, separated into those measured in the SAL and MBL. The size distribution in the SAL displays a broad shape which does not change with increasing or decreasing dust load, but simply shifts ~~towards~~ between higher or lower volume concentrations. For example, for b924 under large dust loadings where lidar-derived AODs approached 2.0 (Marenco et al., 2018, in review), the volume concentrations are markedly larger than other flights in AER-D (green points in Figure 5), although the size distribution shape is much the same. This is in contrast to measurements over land close to dust sources during Fennec (Ryder et al., 2013b) where the absence or presence of the coarse and giant modes had a strong impact on the overall shape of the size distribution, since the relative proportion of giant particles was observed to increase. The peak of the volume concentration during AER-D was constantly between 5-10 µm diameter. ~~The notable exception to this behaviour is that there is~~ We observe a fine mode of aerosol at 0.1-0.3 µm, which is evident when dust concentrations are lower, but becomes eclipsed by the accumulation mode dust during flights with larger dust loadings (e.g. b924). Section 3.4 shows that the composition of ~~sub-~~d < 0.5 µm ~~diameter~~ aerosol in the SAL during AER-D was dominated by sulfates and salts, thus explaining the different behaviour of this mode. Liu et al. (2018) examine the composition and behaviour of the accumulation mode during ICE-D in more detail.

In the MBL, a distinct giant mode is evident between 20 to 60 µm during three flights (b924, b928 and b932: red, green and orange in Figure 5b~~; red, green and orange~~). For flight b928, filter sample analysis (Section 3.4) confirms that this giant mode is composed of dust, rather than sea salt. Higher wind speeds in the MBL, which may be an indicator of sea salt abundance, are not correlated with the presence of this giant mode (10-11 ms^{-1} for b924 and b932; 3-5 ms^{-1} for b920, b928 and b934). It is possible that turbulent mixing from the SAL to the MBL is more likely given a weak inversion and higher turbulence. Therefore ~~W~~we also examined whether the strength of the temperature inversion (calculated using the vertical gradient of potential temperature) and the strength of turbulence at the inversion (indicated by the variance of vertical velocity) could be related to the giant particles present in the MBL. ~~, since it is possible that turbulent mixing from the SAL to the MBL is more likely given a weak inversion and higher turbulence.~~ However, we found no obvious connection in these cases. We note that giant mode particles in the MBL were only present during flights when there was a significant presence of giant mode particles in the SAL above: there is a giant mode in Figure 5b (flights b924, b928, b932; green, orange red) only when a higher concentration of particles in the SAL in the same size range was measured (Figure 5a, same colours). When few particles are measured in the SAL in this size range (b920 and b934, blue and purple), the MBL giant mode is also absent. Thus the observations suggest that the giant MBL mode may be dust being deposited from the overlying SAL towards the ocean. This has also been suggested by Jaenicke and Schutz (1978) from aerosol surface observations at Sal, Cape Verde, where giant particles (d > 40 µm) were observed to arrive at the site a day after that of coarse dust particles (6 < d < 60 µm).

Despite careful error analysis and selection of instrumental data, there is still a large degree of noise as a function of diameter in the wing probe size distributions shown in Figure 5, which was also not indicated in the filter sample PSDs. Therefore in Figure 6~~Figure 6a~~, lognormal curves using 4 lognormal modes are fitted to the wing probe instrumental data using a least squares regression (Markwardt, 2008) with mode parameters from ~~Table 4~~Table 5. The lognormal curves represent a best-fit across the full size range for the instruments available. Differences between the effective diameter calculated with the best-fit lognormal curves and the observed PSDs are between 10-15%, resulting largely from deviations between the observations and best-fit curve in the CDP size range (3 to 20 µm).

It can be seen that the volume concentrations in the SAL are larger than those in the MBL, as expected due to the higher concentrations of elevated dust, and that the SAL size distribution has a notably different structure. ~~While d~~Dust in the SAL displays a broad size distribution~~,~~ with contributions from particles over a wide range of sizes (0.3 to 100 µm), peaking at 5 - 10 µm~~.~~, ~~t~~The MBL size distribution has a narrow peak at d~5 µm and a giant mode contribution at around 20 to 60 µm, where volume concentrations in the MBL mean are actually larger than the SAL mean. Compared to PSDs over the desert measured with aircraft during Fennec and SAMUM1 (Ryder et al., 2013b; Weinzierl et al., 2009), where the volume distributions peak at diameters larger than 10 µm, AER-D has a smaller giant mode contribution, as would be expected. The AER-D PSD is more in keeping with other aircraft observations of transported dust, where the volume distributions peak at diameters between 3 to 10 µm (measured during GERBILS (Johnson and Osborne, 2011), ADRIMED (Denjean et al., 2016), SAMUM2 (Weinzierl et al., 2011) and SALTRACE (Weinzierl et al., 2017)). Despite some agreement here, the variation of size across the 3 to 10 µm size range can still have a large impact on the dust radiative effect (Tegen and Lacis, 1996). MBL PSDs under the influence of dust advection were measured by Kandler et al. (2011b) at Cape Verde. Their observations revealed a sharp mode at 10 µm, declining steeply at larger sizes, which contrasts to our modes centred at d~5 µm and 20 to 60 µm. They also found that when air masses had a maritime origin (but still dominated by dust) the PSD was broadly flat between around 10 to 80 µm, similar to the AER-D MBL PSDs.

Size distributions have also been derived from the 4 filter samples, and are contrasted to the wing-probe size distributions in Figure 7. Such comparisons have previously been shown to be challenging due to the different nature of measurement from each instrument (e.g. Chou et al. (2008); McConnell et al. (2008); Price et al. (2018)) and discrepancies are common, particularly with non-spherical particle geometry. We note that particles measured by the PCASP will be randomly orientated due to passing into the PCASP nozzle~~.~~, ~~while the~~ L~~l~~arger particles sampled by the CDP and those measured by the 2DS and CIP15 may be aligned horizontally in the atmosphere (e.g. Ulanowski et al. (2007)), and measured in this orientation. Also,, ~~and that~~ each technique allocates size using a different methodology. Additionally filter sample viewing is likely to preferentially view the larger cross-section of plate-like particles as they fall flat on the filter substrate.

Figure 7 shows that in most cases, the filters size distribution is greater than that from the wing probes. In the size range 0.5-1 µm the best agreement is found. In 3 of the 4 ~~flight legs~~SLRs, the filters coarse mode volume distribution exceeds that of the wing probes by an order of magnitude or more. At d<0.5 µm the filters size distribution shows a much more distinct fine mode than that seen from the PCASP. Solid lines for the filter samples (blue and orange) in Figure 7 indicate volume distribution calculated assuming spherical shape using diameter calculated from the area-equivalent diameter of the fitted ellipse. ~~Since i~~It is possible that the filter samples overestimate size, and therefore also volume, if particles are plate-like and fall flat on the filter substrate.~~,~~ W~~w~~e ~~also~~ test whether accounting for this by including a representation of particle height,~~,~~ using a height:maximum axis ratio of 1:3 (Chou et al., 2008) can improve the agreement with the wing probes. This sizing metric is shown by the dashed lines in Figure 7. Although accounting for preferential particle orientation on the filters makes some differences to the derived size distribution, it is not sufficient to allow agreement with the wing probe size distributions. It is possible that there were problems with the filters flow rates measured during AER-D resulting from some combinations of filter pore sizes and filter supports. ~~flight legs~~SLRs with higher flow rates (b920 R2 and R5) show better agreement with the wing probes (Figure 7a and c) and also used filter samples with the larger pore sizes (0.4 µm), compared to the other two SLRs (Figure 7b and d) which have worse agreement. We note that for all the SLRs shown, the shape of the coarse mode size distribution is the same for both filters and wing probes, even if they are offset. For example, the broad shoulder of the coarse mode size distribution can be seen in b928 R2 (Figure 7b), and the sharper drop off of the coarse mode in b920 R5 and b934 R6 (Figure 7c and d), for both filters and wing probe size distributions. Additionally diameters of the peak size distribution (5-10 µm) are consistent between filters and wing-probes for the SAL (c and d). We also note that the filters PSD is much smoother than that from the CDP.

Examination of the metric of effective diameter is useful, since it takes into account the contribution of a range of particle sizes. Figure 8a shows that the effective diameter of the full size distribution computed from the wing probes is fairly constant with altitude with no discernible trend, as expected for a well-mixed SAL. A similar picture is seen for the VMD but with values of around 5 to 6 µm (not shown). No evidence is found for larger particles being more abundant closer to the base of the SAL, as would be expected due to gravitational settling. For the SAL the mean (minimum, maximum) d_{eff} value is 4.0 µm (3.6, 4.7) while for the MBL the mean is 4.6 µm (3.4, 5.5). Variation within the MBL is much greater due to the absence or presence of the giant mode shown in Figure 6. ~~Within the SAL d_{eff} differed by a mean of 0.3 µm and up to 0.9 µm between PSDs using the CIP15 and the 2DS-XY for the giant mode (not shown).~~ Mean (minimum, maximum) d_{eff} for the accumulation mode is smaller at 1.7 µm (1.4, 2.0) for the SAL, and 1.1 µm (0.7, 1.4) for the MBL, in agreement with Liu et al. (2018), reflecting the enhanced fine mode in the MBL size distribution from 0.1 to 0.3 µm diameters shown in Figure 5. We also note that d_{eff} for flight b924 in the thick dust layer was 4.3 µm – not at all different from other d_{eff} values in typical dust loadings, despite total volume concentration being much larger. Mean AER-D size parameters of d_{eff} and VMD are given for the SAL and MBL in ~~Table 5~~Table 6.

In addition to d_{eff}, we also show the maximum size (d_{max}) detected by the 2DS XY at concentrations greater than 10^{-5} cm^{-3} (see Section 2.3.2), as a useful indication of transport of the largest sizes, which ~~dominate~~ can contribute substantially to the mass fraction and are therefore important to dust biogeochemical cycles. Figure 8b shows maximum size detected during AER-D ~~in black~~. The largest value of 80 µm at 900 m comes from flight b924, during the intense dust event. Within the SAL, d_{max} varied between 20 to 80 µm, and the same range was found within the MBL. There is no clear trend of d_{max} decreasing with altitude. ~~some suggestion that d_{max} decreases with altitude, though this trend is mostly implicated by the outlier point at 1km measured during the intense dust event of b924.~~ Particles sized ~~over~~ 20 µm (40 µm) ~~diameter~~ or larger were detected in 100% (36%) of the AER-D dust layers investigated, and in 100% (80%) of MBL layers. The lack of decrease of d_{max} with altitude during AER-D is similar to that observed over the desert during SAMUM1 by Weinzierl et al. (2011)~~,~~.

The prevalence of coarse particles shown in Figure 8b~~c~~ is greater than predicted due to settling velocities alone: a 20 µm particle should fall 5 km in 1.4 days (Li and Osada, 2007), and a 40 µm particle would take 13 hours for the same distance. Therefore with the dust age range in AER-D estimated at 17 hours to 4.6 days, we would not expect any 40 µm particles to be present at all, and would only expect 20 µm particles at altitudes below 2.4 km, yet 40 µm sizes were measured over 3 km and 20 µm sizes were measured at altitudes over 4 km.

Aspect ratio derived from the filter samples, defined as the ratio of the major to minor fitted-ellipse axes, is shown in Figure 9. The results are somewhat noisy in the larger size ranges due to the relatively small number of particles analysed, and samples where n<10 have been excluded. As expected, larger particles are more non-spherical in general, with higher median aspect ratios (between 1.30 and 1.51) for the 5 to 10 µm and 10 to 40 µm size ranges. This contrasts to the 0.5 to 5 µm range where median aspect ratio varied from 1.3 to 1.44 and modal values are 1.3. This is particularly notable ~~for all samples, particularly so~~ for b928 R2 in the MBL where there were enough giant mode particles (10-40 µm) counted, showing much larger modal aspect ratios of 1.5 (median of 1.50)~~compared to all other samples and size ranges, where modal values are 1.3~~. For flight b920 the smallest particles (0.1-0.5 µm) were more spherical (modal aspect ratios 1.0-1.2, median values 1.08 and 1.23), though b928 R2 and b934 R6 contrast to this with much greater fractions of higher aspect ratios for smaller particles (mode aspect ratios 1.2-1.4, median values of 1.27 and 1.13, a larger tail in the aspect ratio distribution). This is explained by the composition of these latter 2 ~~flight legs~~SLRs being more strongly dominated by sea salt with a cuboid shape. Data representing the accumulation mode and full PSD strongly shadow the smallest size bin shown, since the data are dominated by smallest particles with the highest number concentrations. Our median values are slightly lower than the majority of those reported in the literature. E.g. SAMUM1 values were around 1.6 for d>0.5 µm and 1.3 for smaller particles (Kandler et al., 2009), while at Praia, Cape Verde, Kandler et al. (2011a) found values of 1.6-1.7 at d>0.7 µm and values below 1.4 at d<0.7 µm, and Chou et al. (2008) found median values of 1.7 during AMMA. Contrastingly Rocha-Lima et al. (2018) found lower modal values of 1.3 from ground-based samples during Fennec.

3.3 Mass Loading

In order to facilitate comparisons with model data, where typical output is in terms of dust mass loadings, Figure 10 shows dust mass loadings from all the 31 AER-D in-situ aircraft profiles, calculated from the measured size distributions and assuming a typical dust density of 2.65 gcm^{-3} (Tegen and Fung, 1994) and spherical p~~e~~articles. The intense dust profiles encountered during certain sections of flights b923/b924 are highlighted in orange, where dust was elevated further north around the Canary Islands, and in red where the dust was found at lower altitudes at around 23N, since they both show notably higher dust mass loadings. Due to the presence of a strong coarse and giant mode, mass loadings are generally high, and typically 300-1000 μgm^{-3} in the elevated SAL (Figure 10a, black lines) when AODs were low to moderate (0.2 to 0.5) (black lines). Exceptionally high values were found during the intense dust event on 12 August 2015 when values of mass loading exceeded 1000 μgm^{-3} and reached a maximum value of around 460043 μgm^{-3}. These values are of the order of a factor of ten larger than those observed in the region previously measured up to a maximum size of 20 µm (Collins et al., 2000; Garrett et al., 2003).

Figure 10b shows that the mass contained within the accumulation mode (d<2.5 µm) ~~decreases by~~is around a factor of ten lower than ~~compared to~~ the total mass, indicating that sub-sampling dust properties behind size-limiting inlets significantly under-samples dust mass. Specifically, we find that on average 14% (10^{th} and 90^{th} percentiles at 6 and 28%) of total mass is contained within ~~PM2.5~~the accumulation mode between altitudes of 1.5 to 4 km, values in agreement with estimates by Kok et al. (2017). Figure 10c and d further illustrate the impact of size on the mass loading by showing the fraction of mass contained at diameters greater than 5 µm and 20 µm (c and d respectively). These values are selected since 5 µm is the diameter at which models begin to under represent dust mass concentration compared to observations (Kok et al., 2017), and few models represent dust particles larger than 20 µm (Huneeus et al., 2011). On average, around 60% of the mass is found at sizes greater than 5 µm and 0-12~~0~~ % at sizes greater than 20 µm in the SAL between altitudes of 1.5-4 km where most of the mass is found. Within the MBL a greater fraction of mass is found at large sizes: 70-80% greater than 5 µm and 10-20% greater than 20 µm. In the extreme, up to 90% of dust mass can be found at sizes greater than 5 µm and up to 40% at sizes greater than 20 µm.

There appears to be a trend with altitude shown in Figure 10c: the mean mass fraction at d > 5 µm decreases steadily from 0.75 at the surface to 0.23 at 5 km altitude. A decrease is also evident in panel d with the largest fractions being found towards the bottom of the SAL (excluding the MBL). These decreases with dust mass as a function of altitude are somewhat in contrast to the homogeneous distribution of d_{eff} throughout the SAL shown in Figure 8. This may be due to the data shown in Figure 10 coming from profiles rather than SLRs, such that more data is available, and also that although d_{eff} represents the full size distribution, as such it is relatively insensitive to smaller changes in the coarse and giant particle concentration. Either way, there is clearly evidence of coarser dust particles being more prevalent towards the bottom of the SAL (and also in the MBL), indicating deposition processes occurring.

Additionally, we have calculated dust mass path (DMP, also known as integrated column mass loading) values from the mass profiles, where DMP is the vertically integrated mass of dust per unit area (Evan et al., 2014). For AER-D low to moderate AODs, mean DMP is 1.0 gm^{-2} (minimum and maximum values of 0.2 and 2.4 gm^{-2}). These values are higher than, but within the bounds of error and variability of those derived from satellite retrievals in the same geographic region (Evan et al., 2014). However, DMPs produced by CMIP5 models are much lower (0.05 to 0.46 gm^{-2} with a multi-model median of 0.26 gm^{-2}) – falling at or below the lower edge of the AER-D values, furthering the argument that models underestimate dust mass loading due to poor representation of dust coarse mode. For the intense dust event on 12 August DMP values are extremely large, from 3.1 to 6.2 gm^{-2}.

3.4 Dust Composition

Figure 11 shows the size resolved and bulk (full PSD and accumulation mode, d<2.5 µm only) composition results for the 4 filter samples analysed. In general, across all the samples and all size ranges above diameters of 0.5 µm, the particles are dominated by alumino-silicates and quartz, with alumino-silicates forming over 80% of the composition volume, with quartz typically forming around 10% of the volume, though sometimes being up to 20%, consistent with Price et al. (2018). Other components are generally low in volume percentage, with calcium-rich particles providing up to 15% of volume content in some samples. Particles dominated by iron are present in low quantities (and therefore displayed separately on the right hand axis), although their contribution is extremely important in controlling shortwave refractive indices (section 3.5). Fe-rich particles are present in higher quantities in the SAL cases (0.5-2.5%) compared to the MBL (0-0.9%). Error bars are noticeably large for Fe-rich particles due to the relatively low counting statistics. Although there is some variation in the iron content as a function of particle size, no distinct pattern is displayed across all the samples, and the uncertainties prevent definitive conclusions from being drawn. Even when the uncertainties are reduced by looking at the full PSD vs accumulation mode only (black circle and triangle), iron content is higher for the full PSD than the accumulation mode in the SAL for b920 R5 (1.7% vs 1.3%), whereas for b934 R6 also in the SAL, iron content is higher in the accumulation mode than for the full PSD (1.3% vs 0.6%). These values agree well with the range of hematite content proposed by Balkanski et al. (2007) where values span 0.9 to 2.7%, though our values will be low-biased as ~~they~~ we only include iron when iron was the dominant component of a particle, ~~detectable as single iron particles,~~ and it is evident that iron is present as a portion of almost all larger particles. Iron is detected across the full size range in variable amounts, thus where absorption is increased due to large particle sizes, it will be further increased due to elevated iron content.

The size range 0.1 to 0.5 µm (shown in dark blue) displays notably different composition, in keeping with the different size distribution displayed for the fine mode (Figure 5 and Figure 7) indicating a different aerosol type. Although some fraction of this fine mode is composed of dust particles (alumino-silicates and quartz), there is always a contribution from sulfate particles (10-40%). Contributions from sea salt in the MBL fine mode (25 and 55%) are higher than in the SAL, as expected. Samples

B928_R2 and B934_R6 show noticeably higher thenardite concentrations, possibly indicative of dry saline lake origins (e.g. Formenti et al. (2003)) or sea salt reacted with sulfuric acid. The high contribution of sea salt in the fine mode in b928 R2 (Figure 11b) impacts the aspect ratio distributions for this size range shown in Figure 9b, where these small particles are much less spherical and present a rectangular shape in the SEM imagery, inferred to be a cuboid shape.

Figure 11 shows that even within the MBL, the aerosol content was dominated by dust particles in both cases examined here. Additionally, during b928 R2 (orange points in Figure 5b, and Figure 11b), one of the ~~flight legs~~SLRs when a substantial giant mode was present, the composition data confirms that this giant mode (purple points) was composed of dust, being dominated by alumino-silicates, quartz and calcium rich-particles (most likely calcite).

Kandler et al. (2009; 2011a) show that the quartz fraction for particles increases with particle size, particularly for d>20 µm. Our data do not show that quartz content appreciably increases with size, though this may be due to the relatively large errors on the size-resolved data, although even the bulk data for the full PSD and accumulation mode PSD with smaller error bars do not show significant differences in quartz content. It may also be due to our filters data not extending to such large size ranges (up to 200 µm) as Kandler et al. (2009).

Additionally, in contrast to Liu et al. (2018), we do not detect any black carbon on the filter samples, which they find present predominantly between sizes of 0.1 to 0.6 µm. During the analysis of 6500 particles, only one black carbon chain structure was observed. This difference is unlikely to be due to the pore size of the filter samples (0.2 and 0.4 µm) allowing small BC particles to pass through them, since our filters collect efficiently over a size range extending below this by diffusion and impaction (e.g. Lindsley (2016)) and the size distributions in Figure 7 clearly show that this size range is collected. BC loadings for the ICE-D flights shown in Liu et al. (2018) are very low (0.05-1.0 μgm^{-3}). The most likely explanation is that BC particles were not present in sufficient concentrations to be sampled by the filters.

3.5 Refractive Indices

Size resolved and bulk complex refractive indices at 550 nm calculated from the filter samples' composition are shown in ~~Table 6~~Table 7, and full spectral variability (solar and terrestrial) is shown in the supplement, figures S2 and S3. Real values in ~~Table 6~~ Table 7 representing the full PSD and accumulation mode PSD are generally 1.47 to 1.49 and do not vary substantially. These values are relatively low compared to that expected for dust, and may be influenced by the lower real part of illite in determining the 'alumino-silicate mean' refractive index which is an average of illite and kaolinite. Other refractive indices such as those of Kandler et al. (2009; 2011a) solely apply kaolinite refractive indices and produce higher real values. The low values may also be influenced by the internal volume mixing rule applied here, and are consistent with those from Formenti et al. (2014). Additionally, the percentages of kaolinite and illite by mass respectively have been shown to vary between 71.1±13.5% and 16.4±11.8% for dust originating from Southern Mali/Algeria, to 30.7±3.2% and 54.2±6.0% for dust

from Mali/Mauritania/Western Sahara (Formenti et al., 2014). Real values are also distinctly higher for the smallest size class, though this has no impact on the bulk value due to the low volumetric contribution from these small sized particles.

Much more variability is seen in the imaginary part, largely influenced by the iron content and its absorbing influence via hematite and goethite. For the two samples in the SAL, k is the same for both in the accumulation mode (0.0023~~i~~), but increases or decreases to 0.0030~~i~~ or 0.0012~~i~~ when the coarser particles are included. To explain this, inspecting the size resolved data, it can be seen that for sample b920 R5 k increases with size from 0.0020~~i~~ to 0.0034~~i~~ reflecting the increasing iron content with size seen in Figure 11c. However this is not the case for the second SAL sample (b934 R6) where iron content and k are highest (0.0023 to 0.0039~~i~~) in the mid-range sizes from 0.5 to 5 microns (Figure 11d), while lower k values (0.0003 to 0.0009~~i~~) are found for d < 0.5 µm and d>5 µm due to their lower iron content.

Imaginary parts for the MBL are much smaller than those for the SAL (0.0004-0.0005~~i~~ compared to 0.0012 to 0.003~~i~~), reflecting the lower iron content across all size ranges. Real parts in the MBL are not notably different to those in the SAL.

Longwave spectral refractive indices have also been calculated and are shown in Figure S3 in the supplement. Here the main controlling factor is the fraction of sea salt and sulfate-rich particles, which is important for d<0.5 µm and occasionally up to d=1 µm in the MBL, and the relative proportion of alumino-silicate and quartz is important for sizes d>0.5 µm. The refractive indices of sea salt used here have zero absorption in the longwave spectrum, so higher salt content lowers k in the smallest size range. All samples show an increase in absorption within the atmospheric window between around 8.5 to 10 µm. The quartz absorption peak occurs at 9.4 µm while the alumino-silicate peak occurs at 9.6 µm. Thus the relative proportions of these two minerals control the height of each of these peaks, but since no significant size resolved change in the quartz:alumino-silicate ratio was found in Section 3.4, any size resolved changes in these peaks in the longwave refractive index are negligible.

~~Additionally,~~ Tthe longwave imaginary parts are substantially higher between 9-10 µm, by 2 to 3 times, than those of some of the literature where k is less than 1.0 (Di Biagio et al., 2017; Fouquart et al., 1987; Volz, 1973; Hess et al., 1998; Balkanski et al., 2007), although our values similarly high to those of both Otto et al. (2009) and Formenti et al. (2014) who used the similar internal mixing volume calculations. We purport this to be due to the assumption of an internally mixed dust aerosol to be inappropriate, knowing that the dust ~~is~~ actually is externally mixed (excepting the complex nature of iron existing within mixtures), as in Formenti et al. (2014), though why this assumption produces worse results in the longwave spectrum is unclear. Other ways of calculating the refractive index based on iron being internally mixed, while quartz and alumino-silicates are externally mixed are possible (e.g. Balkanski et al. (2007)), as are other more complex ways of representing internal and inhomogeneous mixing (Lindqvist et al., 2014; Nousiainen, 2009) but are beyond the scope of this work.

3.6 Optical Properties

Figure 12 shows how SSA varied with height for the accumulation mode and the full size distribution. SSA was fairly constant with altitude within the SAL. Measured mean (minimum, maximum) accumulation mode SAL SSAs (black) were 0.97 (0.93, 0.98). MBL values were all greater than 0.99. Mie-calculated values of SSA for the accumulation mode (orange) agree with measurements (black) within error bounds, since here agreement in SSA is tuned by refractive index iterations. Once the full size distribution had been accounted for, calculated SSA values (green) decrease to 0.95 (0.91,0.98) for the SAL and to 0.99 (0.97,0.99) for the MBL. Since larger particles are more absorbing for a fixed refractive index, this decrease is expected, and the magnitude of the decrease is dependent on the amount of coarse ~~mode present~~particles, and also the refractive index. In the MBL, SSA values do not decrease much since k^{550} is ~~so~~ small (~0.0001i); the addition of a coarse mode of negligible absorption makes little difference to SSA. However, in the SAL, where derived k^{550} varies from 0.0005 to 0.0025i, the addition of the full coarse mode causes SSA to drop noticeably.

Since it is clear from the composition results that aerosol in the SAL is dominated by dust across all sizes, applying the same k^{550} for the accumulation mode to the coarse particles may be appropriate. However,~~,~~ ~~although~~ some variation of dust composition with size is still evident (Section 3.4) which is not taken into account in Figure 12. The low k^{550} of 0.0001i in the MBL is representative of highly scattering sea salt or sulfates ~~as~~ which dominate the fine mode in the MBL (Section 3.4), although it is clear that dust particles dominate at larger sizes in the MBL. Therefore extending the low value of k^{550} to the coarse mode in the MBL is a less reasonable assumption. Therefore it is likely that the SSA values in the MBL for the full size distribution shown in Figure 12 are overestimates. SSA values calculated using a RI representative of dust for the coarse mode from filter samples are discussed later on.

Theoretically, ~~It is possible~~ the variability of the optical properties of dust in the SAL ~~is~~ may be determined by either the dust composition, the dust size distribution, or both. Other elements may also influence the optical properties, such as particle shape, roughness, hygroscopic growth and mixing, but are not considered here as there are few observational constraints available on these properties from AER-D. In order to determine the contributions from both particle size (assessed via d_{eff} from the measured size distribution) and composition (assessed via k^{550} calculated from two different methods described in Section 2.5) to the variability of ~~optical properties~~SSA, we show both d_{eff} and k^{550} as a function of SSA in Figure 13, separated into the ACC PSD and FULL PSD size ranges.

It is clear that during AER-D, it was the variability of dust composition that controlled the variability of SSA, rather than the variability of size distribution. In Figure 13a for the SAL (orange) points, it can be seen that the direct observations for the accumulation mode (orange asterixes, where nephelometer and PSAP scattering and absorption are used to calculate SSA) are in agreement with Mie simulations using the ACC PSD (small orange circles). When the coarse mode size distribution is then

included (large orange circles), effective diameter increases and there is a slight decrease in SSA. Although d_{eff} does impact the magnitude of the SSA, within AER-D the shape of the PSD was relatively stable, with a relatively constant d_{eff}.~~,~~ ~~which~~ This meant that the small variation of size distribution shape had minimal impact in determining the variability of SSA.

Figure 13b shows the variation in SSA as a function of composition, represented by k^{550}~~, as a function of the SSA~~. Here we show the relationship between these two variables calculated with different RI datasets: firstly for RI from the Mie scattering iterations (circles, Section 2.5.1) and secondly for RI calculated for filter sample composition (diamonds, Section 2.5.2). Optical properties are shown for the accumulation mode only (small data points), and for the full PSD (large data points). For dust in the SAL, Figure 13b shows a consistent decrease in SSA with the imaginary part of the refractive index. This relationship becomes more negative when the full coarse mode PSD (large symbols) are included because for a fixed RI, the larger particles exert more absorption. Although there is some variability between the results from different RI datasets, overall they show the same trend.

Contrastingly to Figure 13a, Figure 13b shows that the ~~optical property~~SSA variability was strongly influenced by the variability in composition. This is the case for both accumulation mode observations of SSA, and for the full size distribution. It is not surprising that variability in k^{550} influences absorption and therefore SSA. However, the SSA can be influenced by several factors, including the PSD. Our aim is to investigate which factors influence the variability of the SSA. Therefore it is notable that there is so little variation in the PSD during AER-D that the composition (or k^{550}) is the main factor contributing to the variability of the SSA. This finding is notably the opposite from that found during Fennec, where the size distribution was the dominant controller of optical properties. Liu et al. (2018) show that hematite content is important in the ICE-D/AER-D samples as a controlling factor on optical properties. Moosmuller et al. (2012) and Caponi et al. (2017) also show dependencies of refractive index on iron content. This is consistent with our findings that the calculated refractive index from the filter samples is strongly influenced by the iron content and its absorbing properties. It appears that over the Sahara, variations in the PSD (affected by dust age) have an important impact on SSA, while over the ocean the impacts of composition (perhaps either by chemical aging or by sampling dust from different sources) become more important.

Finally, we compare optical properties calculated with composition data from the filter samples using both internal and external mixing assumptions against observations in Figure 14 for the ACC PSD (a) and the FULL PSD (b). Observations are available only for ~~The SSA is calculated for~~ the ACC PSD size range ~~only since we have direct observations only for the accumulation mode due to inlet restrictions~~. Figure 14a shows ~~It is clear~~ that compared to the observations of SSA, the external mixing assumption provides closer agreement with the observations, confirming that the internal mixing assumption used to derive refractive indices shown in Section 3.5 overestimates the absorption, consistent with previous publications (Formenti et al., 2014). Figure 14b shows the same results but for the full PSD, and also those for the iterated RI for the full PSD.~~Additionally,~~ ~~t~~The internal and external mixing calculations, when applied to the full size distribution, allow for the composition of larger

particles being dust in the MBL, contrasting~~ly~~ to the iterated RI method which assumes constant composition across all sizes. For the two MBL SLRs the SSAs drop from 0.99 for the ACC PSD ~~The external mixing optical properties for the full size distribution result in SSAs dropping from 0.99 for the two MBL legs,~~ down to 0.98 and 0.97 for external mixing when the coarse mode and its composition is accounted for ~~(not shown)~~ – thus producing SSAs in the MBL similar to those of the overlying SAL. This is only achieved through analysis of the coarse mode aerosol composition within the MBL. SSAs from internal mixing RIs are also 0.98 and 0.97 for the MBL SLRs, but these are much the same as those for the accumulation mode. For b934 R6 there is not much variation between the three methods, while for b 920 R5 the SSA is lower at 0.89 for internal mixing, compared to 0.96 for the other two methods. This is because b934 R6 contained more iron in the coarse mode than the other SLRs (see Figure 11c) which had a strong impact on lowering the SSA for an internal mixing assumption. This is not reflected in the external mixing value due to the non-linearity of the scattering and absorption properties.

Campaign mean optical properties representing the full size distribution in the SAL and MBL are summarized in~~ Table 5~~Table 6. ~~In contrast to Fennec observations of the full PSD and associated optical properties over the Sahara,~~In ~~-~~AER-D, MEC in the SAL is higher (0.27-0.35 m^2g^-) compared to Fennec observations over the Sahara (0.15-0.23m^2g^{-1}, Ryder et al. (2013a)) as a result of fewer coarse and giant particles. AER-D SAL SSA values (0.91 to 0.98, mean 0.95) are somewhat higher than those of Fennec (0.86 to 0.97) for the same RI (Ryder et al., 2013b), and closer to previously published higher values, for transported dust. For example, (Haywood et al., 2003) values of 0.95-0.98 during SHADE and Chen et al. (2011) values of 0.97±0.02 during NAMMA. AER-D SAL Asymmetry parameters are large~~,~~ at 0.74, unsurprising given the presence of coarse particles, contributing to forward scattering.

4 Conclusion

Dust in the SAL during the AER-D airborne field campaign from six different flights, 19 in-situ ~~flight leg~~SLRs and 31 profiles ~~during August 2015~~ has been characterized. The flights were performed in August 2015 between the Cape Verde and Canary Islands. In particular, a strong focus is given to the presence and contribution from coarse and giant dust particles through operating wing-mounted instrumentation intended to sample the full size distribution from 0.1 to 100 µm diameter. This work fills a research gap by providing in-situ coarse mode dust observations which firstly cover the full size range, and secondly by providing these observations in the SAL close to the African continent during the peak dust transport season.

Dust sources contributing to the events sampled were located in southern Algeria, Mali and northern Mauritania, with a well-documented dust hotspot along the Mali/Algeria border contributing to dust sampled in 4 out of 5 cases. Several events sampled dust which had been uplifted from up to three separate source regions. Dust age at sampling was determined to be 17 hours to 4.6 days. Dust transport ~~paths~~pathways, ages and source locations assessed with SEVIRI dust RGB satellite imagery were ~~to be~~ different to paths indicated by back-trajectories, in keeping with Trzeciak et al. (2017) that back-trajectory models struggle

over the convective summertime Sahara. Vertical structure of the dust was consistent with the conventional model of the SAL, with elevated dust (~1-5 km) overlying the MBL, except in one intense dust event with an AOD of 2.5, with thick dust concentrated between 500 m to 2.5 km altitude.

Size distributions spanning 0.1 to 100 µm were assessed by combining wing-mounted optical particle counters and shadow probes. Mean ~~D~~d_{eff} for the SAL ~~the mean~~ (minimum, maximum) was 4.0 µm (3.6, 4.7 µm) while for the MBL the mean was 4.6 µm (3.4, 5.5 µm). ~~D_{eff} in one intense event at 4.3 µm was within the range from other flights, with elevated number concentrations across the full size range.~~ The campaign mean VMD was 5.5 µm. The shape of the measured size distribution did not vary significantly between dust layers (reflecting d_{eff} values which were relatively constant both at different altitudes and in different dust events)~~,~~ ~~with v~~Volume size distributions consistently peak~~ed~~ing between 5 to 10 µm, even though total volume concentrations were found to increase or decrease with dust loading. This contrasts to the Fennec results over desert where the contribution from the coarse mode was highly variable, as was d_{eff} (Ryder et al., 2013b). Within the SAL dust layers, particles sized ~~over~~ 20 µm diameter or larger were detected in 100% of cases, and particles ~~over~~ 40 µm or larger were detected in 36% of cases, at concentrations over 10^{-5} cm^{-3}. Based on dust age at sampling time, more coarse and giant particles were present than expected due to gravitational sedimentation alone.

Giant particles (d>20 µm) were found in the MBL on 3 out of 5 flights. Filter sample analysis for one of these cases confirms that these giant ~~MBL mode~~ particles were dust. The shape of the size distribution indicates similarity to the dust layers above in the SAL, and therefore suggests a high likelihood of dust being deposited from above. Despite this, the only size metrics which showed ~~no~~ evidence of increasing particle size towards the bottom of the SAL ~~was found~~were the mass fraction of particles sized over 5 and 20 µm.

Size distributions from vertical profiles were also used to calculate~~d~~ size resolved mass loadings. Very large values were found, between 300 to 1,000 $µgm^{-3}$ in the SAL for low to moderate AODs (0.2 to 0.5), and up to 46004~~3~~ $µgm^{-3}$ in an intense dust event. Only 14% of mass was found to reside in sizes beneath 2.5 µm, while 60% resided in sizes larger than diameters of 5 µm and 0-120% resided at sizes above 20 µm. The latter two diameters are important, ~~denoting~~ representing ~~diameters~~ sizes where models begin to underestimate the size distribution and where models typically exclude larger particles respectively (Kok et al., 2017; Huneeus et al., 2011). Thus it is clear that a large proportion of mass resides in the larger size ranges, which will impact biogeochemical cycles in models if underestimated. Dust Mass Paths (DMPs) were also calculated for these profiles giving values between 0.2 to 2.4 gm^{-2} (mean of 1.0 gm^{-2}), in agreement with satellite-derived values of Evan et al. (2014) within error bounds.

Analysis of four filter samples provided information on size-resolved aspect ratio, composition, and refractive indices. Modal aspect ratios were 1.2 to 1.4, ~~slightly~~ lower than typically found in the literature. In the SAL, alumino-silicate particles

dominated the composition at sizes above 0.5 µm, followed by ~~and~~ quartz, ~~particles dominated the composition at sizes above 0.5 µm,~~ although sulfates and sea salt were present in significant quantities at sizes beneath 0.5 µm. In the MBL the situation was similar, with particles sized over 1 µm being predominantly dust, though the contribution of sulfates and sea salt extended up to 1 µm diameter. The iron rich fraction was small in the SAL (0.5 to 2.5% by volume fraction), and even smaller in the MBL (0 to 0.9%). Although iron content varied with particle size, there was no consistent behaviour across the small number of samples analysed.

Full spectral complex refractive indices were calculated from the filter samples. At 550 nm, the imaginary part of the refractive index k^{550} for the full PSD was 0.0012 to 0.0030~~i~~ in the SAL, strongly influenced by the volumetric iron content. Real parts were relatively low at 1.48 due to the low real values contributed by the literature kaolinite data. In general, refractive indices at 550 nm calculated from two different methods agreed well. For the full spectrum of data, iterated k^{550} values representing the accumulation mode covered 0.0005 to 0.0025 with a modal value of 0.001~~i~~. Refractive indices calculated from composition data and internal mixing assumptions were found to overestimate absorption, while external mixing assumptions provided the best agreement with observations.

SSAs for the accumulation mode were measured, and SSAs for the full size distribution were calculated using measured size distributions and derived refractive indices at 550 nm. Within the SAL, measured SSAs at 550 nm for the accumulation mode were 0.93-0.98 (mean 0.97), and calculated values for the full size distribution dropped to 0.91-0.98 (mean 0.95). During AER-D~~, the shape of the PSD varied little, yet~~ the SSA still showed a reasonable amount of variability. The contribution of both PSD and k to the variability of SSA was investigated. Both the shape of the PSD and d_{eff} varied little, despite total dust concentrations being variable. Therefore during AER-D, variability in PSD did not have a strong effect on SSA. This allowed ~~variability was found to be controlled by~~ variations in composition (via the imaginary part of the refractive index) to control the variability of the SSA~~, rather than variations in size distribution~~. This contrasts to Fennec where size was strongly the controlling factor. Liu et al. (2018) show that hematite variability within the accumulation mode was an important control on SSA during ICE-D. Within the MBL, aerosol in the accumulation mode was extremely scattering with SSA values above 0.99. However, once accounting for the coarse mode particles and coarse mode-specific composition, SSAs within the MBL were found to be more absorbing and representative of mineral dust.

Over the Atlantic, a significant coarse mode of dust is still present, and contributes to the overall optical properties of dust~~,~~. Particles larger than ~~and is greater than~~ expected from sedimentation processes alone are found. Additionally, the transport of mass is dominated by the larger particles, which is important to biogeochemical cycles via deposition of nutrients to the ocean. However, we find that variability in the optical properties is controlled principally by the variability in composition. Therefore in order to appropriately model the transport of dust and its associated optical properties and mass impacts, dust models must

attempt to capture both the broad size range of particles detected by measurements, and also the variability in composition, particularly that from absorbing iron oxides.

Data Availability

Facility for Airborne Atmospheric Measurements (2015): UK ICE-D: atmospheric measurements dataset collection. Centre for Environmental Data Analysis, July 2018. http://catalogue.ceda.ac.uk/uuid/d7e02c75191a4515a28a208c8a069e70.

Appendix: Acronyms

2DS Two Dimensional Stereo Probe
APS Aerodynamic Particle Sampler
CAS-DPOL Cloud and Aerosol Spectrometer with Depolarization Detection
CDP Cloud Droplet Probe
CIP Cloud Imaging Probe
FSSP Forward Scattering Spectrometer Probe
OAP Optical Array Probe
OPC Optical Particle Counter
PCASP Passive Cavity Aerosol Spectrometer Probe
SID Small Ice Detector
SLR Straight and Level Run

Acknowledgements

Airborne data from the BAe146 were obtained using the BAe-146-301 Atmospheric Research Aircraft operated by Directflight Ltd and managed by FAAM, which is a joint entity of the NERC and the UK Met Office. ICE-D was supported by NERC grant number NE/M001954/1 and the Met Office. SAVEX-D flights were funded by EUFAR TNA (European Union Seventh Framework Programme grant agreement 312609) and other AER-D flights were funded by the Met Office. C.L.R. acknowledges NERC support through Independent Research Fellowship NE/M018288/1. SAVEX-D was supported by projects PROMETEUII/2014/058 and GV/2014/046 from the Valencia Autonomous Government, and CGL2015-70432-R from the Spanish Ministry of Economy and Competitiveness - European Regional Development Fund. BJM, JBM and HCP thank the European Research Council (ERC) (240449 ICE and 648661 MarineIce) for funding. CEDA are acknowledged for their efforts in storing and archiving ICE-D FAAM data. We thank Claudia Di Biagio for providing mineral refractive index

data and useful discussions, Konrad Kandler for providing calcite refractive index data, ~~and~~ Helen Dacre for dust transport discussions and Graeme Nott for discussions about wing probe flow distortions.

References

Allen, C. J. T., Washington, R., and Engelstaedter, S.: Dust emission and transport mechanisms in the central Sahara: Fennec ground-based observations from Bordj Badji Mokhtar, June 2011, J Geophys Res-Atmos, 118, 6212-6232, 10.1002/jgrd.50534, 2013.

Allen, C. J. T., Washington, R., and Saci, A.: Dust detection from ground-based observations in the summer global dust maximum: Results from Fennec 2011 and 2012 and implications for modeling and field observations, J Geophys Res-Atmos, 120, 897-916, 10.1002/2014jd022655, 2015.

Anderson, T. L., and Ogren, J. A.: Determining aerosol radiative properties using the TSI 3563 integrating nephelometer, Aerosol Sci Tech, 29, 57-69, 1998.

Andreae, M. O., Elbert, W., Gabriel, R., Johnson, D. W., Osborne, S., and Wood, R.: Soluble ion chemistry of the atmospheric aerosol and SO2 concentrations over the eastern North Atlantic during ACE-2, Tellus B, 52, 1066-1087, DOI 10.1034/j.1600-0889.2000.00105.x, 2000.

Balkanski, Y., Schulz, M., Claquin, T., and Guibert, S.: Reevaluation of Mineral aerosol radiative forcings suggests a better agreement with satellite and AERONET data, Atmos Chem Phys, 7, 81-95, 2007.

Bedidi, A., and Cervelle, B.: Light-Scattering by Spherical-Particles with Hematite and Geothite-Like Optical-Properties - Effect of Water Impregnation, J Geophys Res-Sol Ea, 98, 11941-11952, Doi 10.1029/93jb00188, 1993.

Bond, T. C., Anderson, T. L., and Campbell, D.: Calibration and intercomparison of filter-based measurements of visible light absorption by aerosols, Aerosol Sci Tech, 30, 582-600, Doi 10.1080/027868299304435, 1999.

Brindley, H., Knippertz, P., Ryder, C., and Ashpole, I.: A critical evaluation of the ability of the Spinning Enhanced Visible and Infrared Imager (SEVIRI) thermal infrared red-green-blue rendering to identify dust events: Theoretical analysis, J Geophys Res-Atmos, 117, Doi 10.1029/2011jd017326, 2012.

Caponi, L., Formenti, P., Massabo, D., Di Biagio, C., Cazaunau, M., Pangui, E., Chevaillier, S., Landrot, G., Andreae, M. O., Kandler, K., Piketh, S., Saeed, T., Seibert, D., Williams, E., Balkanski, Y., Prati, P., and Doussin, J. F.: Spectral- and size-resolved mass absorption efficiency of mineral dust aerosols in the shortwave spectrum: a simulation chamber study, Atmos Chem Phys, 17, 7175-7191, 10.5194/acp-17-7175-2017, 2017.

Carlson, T. N.: The Saharan Elevated Mixed Layer and its Aerosol Optical Depth, The Open Atmospheric Science Journal, 10, 26-38, DOI: 10.2174/1874282301610010026, 2016.

Charabi, Y., and Gastli, A.: Spatio-temporal assessment of dust risk maps for solar energy systems using proxy data, Renew Energ, 44, 23-31, 10.1016/j.renene.2011.12.005, 2012.

Chen, G., Ziemba, L. D., Chu, D. A., Thornhill, K. L., Schuster, G. L., Winstead, E. L., Diskin, G. S., Ferrare, R. A., Burton, S. P., Ismail, S., Kooi, S. A., Omar, A. H., Slusher, D. L., Kleb, M. M., Reid, J. S., Twohy, C. H., Zhang, H., and Anderson, B. E.: Observations of Saharan dust microphysical and optical properties from the Eastern Atlantic during NAMMA airborne field campaign, Atmos Chem Phys, 11, 723-740, DOI 10.5194/acp-11-723-2011, 2011.

Chou, C., Formenti, P., Maille, M., Ausset, P., Helas, G., Harrison, M., and Osborne, S.: Size distribution, shape, and composition of mineral dust aerosols collected during the African Monsoon Multidisciplinary Analysis Special Observation Period 0: Dust and Biomass-Burning Experiment field campaign in Niger, January 2006, J Geophys Res-Atmos, 113, 10.1029/2008jd009897, 2008.

Collins, D. R., Jonsson, H. H., Seinfeld, J. H., Flagan, R. C., Gasso, S., Hegg, D. A., Russell, P. B., Schmid, B., Livingston, J. M., Ostrom, E., Noone, K. J., Russell, L. M., and Putaud, J. P.: In situ aerosol-size distributions and clear-column radiative closure during ACE-2, Tellus B, 52, 498-525, DOI 10.1034/j.1600-0889.2000.00008.x, 2000.

Denjean, C., Cassola, F., Mazzino, A., Triquet, S., Chevaillier, S., Grand, N., Bourrianne, T., Momboisse, G., Sellegri, K., Schwarzenbock, A., Freney, E., Mallet, M., and Formenti, P.: Size distribution and optical properties of mineral dust aerosols transported in the western Mediterranean, Atmos Chem Phys, 16, 1081-1104, 10.5194/acp-16-1081-2016, 2016.

Di Biagio, C., Formenti, P., Balkanski, Y., Caponi, L., Cazaunau, M., Pangui, E., Journet, E., Nowak, S., Caquineau, S., Andreae, M. O., Kandler, K., Saeed, T., Piketh, S., Seibert, D., Williams, E., and Doussin, J. F.: Global scale variability of the mineral dust long-wave refractive index: a new dataset of in situ measurements for climate modeling and remote sensing, Atmos Chem Phys, 17, 1901-1929, 10.5194/acp-17-1901-2017, 2017.

Diaz-Hernandez, J. L., and Sanchez-Navas, A.: Saharan dust outbreaks and iberulite episodes, J Geophys Res-Atmos, 121, 7064-7078, 10.1002/2016jd024913, 2016.

Doherty, O. M., Riemer, N., and Hameed, S.: Saharan mineral dust transport into the Caribbean: Observed atmospheric controls and trends, J Geophys Res-Atmos, 113, 10.1029/2007jd009171, 2008.

Draxler, R. R., and Hess, G. D.: An overview of the HYSPLIT_4 modeling system of trajectories, dispersion, and deposition, Australian Meteorological Magazine, 47, 295-308, 1998.

Egan, W. G., and Hilgeman, T.: Retroreflectance Properties of Photometric Standards with Polarized Laser-Radiation, J Opt Soc Am, 69, 1415-1415, 1979.

Engelstaedter, S., Tegen, I., and Washington, R.: North African dust emissions and transport, Earth-Sci Rev, 79, 73-100, 10.1016/j.earscirev.2006.06.004, 2006.

Engelstaedter, S., Washington, R., Flamant, C., Parker, D. J., Allen, C. J. T., and Todd, M. C.: The Saharan heat low and moisture transport pathways in the central Sahara-Multiaircraft observations and Africa-LAM evaluation, J Geophys Res-Atmos, 120, 4417-4442, 10.1002/2015jd023123, 2015.

Evan, A. T., Flamant, C., Fiedler, S., and Doherty, O.: An analysis of aeolian dust in climate models, Geophys Res Lett, 41, 5996-6001, 10.1002/2014gl060545, 2014.

Evan, A. T., Flamant, C., Gaetani, M., and Guichard, F.: The past, present and future of African dust, Nature, 531, 493-+, 10.1038/nature17149, 2016.

Formenti, P., Elbert, W., Maenhaut, W., Haywood, J., and Andreae, M. O.: Chemical composition of mineral dust aerosol during the Saharan Dust Experiment (SHADE) airborne campaign in the Cape Verde region, September 2000, J Geophys Res-Atmos, 108, Artn 8576 10.1029/2002jd002648, 2003.

Formenti, P., Rajot, J. L., Desboeufs, K., Caquineau, S., Chevaillier, S., Nava, S., Gaudichet, A., Journet, E., Triquet, S., Alfaro, S., Chiari, M., Haywood, J., Coe, H., and Highwood, E.: Regional variability of the composition of mineral dust from western Africa: Results from the AMMA SOP0/DABEX and DODO field campaigns, J Geophys Res-Atmos, 113, Artn D00c13 10.1029/2008jd009903, 2008.

Formenti, P., Schütz, L., Balkanski, Y., Desboeufs, K., Ebert, M., Kandler, K., Petzold, A., Scheuvens, D., Weinbruch, S., and Zhang, D.: Recent progress in understanding physical and chemical properties of African and Asian mineral dust, Atmos Chem Phys, 11, 8231-8256, DOI 10.5194/acp-11-8231-2011, 2011.

Formenti, P., Caquineau, S., Desboeufs, K., Klaver, A., Chevaillier, S., Journet, E., and Rajot, J. L.: Mapping the physico-chemical properties of mineral dust in western Africa: mineralogical composition, Atmos Chem Phys, 14, 10663-10686, 10.5194/acp-14-10663-2014, 2014.

Fouquart, Y., Bonnel, B., Brogniez, G., Buriez, J. C., Smith, L., Morcrette, J. J., and Cerf, A.: Observations of Saharan Aerosols - Results of Eclats Field Experiment .2. Broad-Band Radiative Characteristics of the Aerosols and Vertical Radiative Flux Divergence, J Clim Appl Meteorol, 26, 38-52, Doi 10.1175/1520-0450(1987)026<0038:Oosaro>2.0.Co;2, 1987.

Garcia-Carreras, L., Marsham, J. H., Parker, D. J., Bain, C. L., Milton, S., Saci, A., Salah-Ferroudj, M., Ouchene, B., and Washington, R.: The impact of convective cold pool outflows on model biases in the Sahara, Geophys Res Lett, 40, 1647-1652, 10.1002/grl.50239, 2013.

Garrett, T. J., Russell, L. M., Ramaswamy, V., Maria, S. F., and Huebert, B. J.: Microphysical and radiative evolution of aerosol plumes over the tropical North Atlantic Ocean, J Geophys Res-Atmos, 108, Artn 4022 10.1029/2002jd002228, 2003.

Gasteiger, J., Gross, S., Sauer, D., Haarig, M., Ansmann, A., and Weinzierl, B.: Particle settling and vertical mixing in the Saharan Air Layer as seen from an integrated model, lidar, and in situ perspective, Atmos Chem Phys, 17, 297-311, 10.5194/acp-17-297-2017, 2017.

Glotch, T. D., Rossman, G. R., and Aharonson, O.: Mid-infrared (5-100 mu m) reflectance spectra and optical constants of ten phyllosilicate minerals, Icarus, 192, 605-622, 10.1016/j.icarus.2007.07.002, 2007.

Glotch, T. D., and Rossman, G. R.: Mid-infrared reflectance spectra and optical constants of six iron oxide/oxyhydroxide phases, Icarus, 204, 663-671, 10.1016/j.icarus.2009.07.024, 2009.

Hansen, J. E., and Travis, L. D.: Light-Scattering in Planetary Atmospheres, Space Sci Rev, 16, 527-610, Doi 10.1007/Bf00168069, 1974.

Harrison, R. G., Nicoll, K. A., Marlton, G. J., Ryder, C. L., and Bennett, A. J.: Saharan dust plume charging observed over the UK, Environ Res Lett, 13, https://doi.org/10.1088/1748-9326/aabcd9, 2018.

Haywood, J. M., Francis, P., Osborne, S., Glew, M., Loeb, N., Highwood, E., Tanre, D., Myhre, G., Formenti, P., and Hirst, E.: Radiative properties and direct radiative effect of Saharan dust measured by the C-130 aircraft during SHADE: 1. Solar spectrum, J Geophys Res-Atmos, 108, Doi 10.1029/2002jd002687, 2003.

Heinold, B., Tegen, I., Esselborn, M., Kandler, K., Knippertz, P., Müller, D., Schladitz, A., Tesche, M., Weinzierl, B., Ansmann, A., Althausen, D., Laurent, B., Massling, A., Müller, T., Petzold, A., Schepanski, K., and Wiedensohler, A.: Regional Saharan dust modelling during the SAMUM 2006 campaign, Tellus B, 61, 307-324, DOI 10.1111/j.1600-0889.2008.00387.x, 2009.

Hess, M., Koepke, P., and Schult, I.: Optical properties of aerosols and clouds: The software package OPAC, B Am Meteorol Soc, 79, 831-844, Doi 10.1175/1520-0477(1998)079<0831:Opoaac>2.0.Co;2, 1998.

Hinds, W. C.: Aerosol technology: properties, behavior, and measurement of airborne particles, Wiley, 1999.

Hoose, C., and Mohler, O.: Heterogeneous ice nucleation on atmospheric aerosols: a review of results from laboratory experiments, Atmos Chem Phys, 12, 9817-9854, 10.5194/acp-12-9817-2012, 2012.

Huneeus, N., Schulz, M., Balkanski, Y., Griesfeller, J., Prospero, J., Kinne, S., Bauer, S., Boucher, O., Chin, M., Dentener, F., Diehl, T., Easter, R., Fillmore, D., Ghan, S., Ginoux, P., Grini, A., Horowitz, L., Koch, D., Krol, M. C., Landing, W., Liu, X., Mahowald, N., Miller, R., Morcrette, J. J., Myhre, G., Penner, J., Perlwitz, J., Stier, P., Takemura, T., and Zender, C. S.: Global dust model intercomparison in AeroCom phase I, Atmos Chem Phys, 11, 7781-7816, DOI 10.5194/acp-11-7781-2011, 2011.

Jaenicke, R., and Schutz, L.: Comprehensive Study of Physical and Chemical Properties of Surface Aerosols in Cape-Verde-Islands Region, J Geophys Res-Oc Atm, 83, 3585-3599, DOI 10.1029/JC083iC07p03585, 1978.

Jickells, T. D., An, Z. S., Andersen, K. K., Baker, A. R., Bergametti, G., Brooks, N., Cao, J. J., Boyd, P. W., Duce, R. A., Hunter, K. A., Kawahata, H., Kubilay, N., laRoche, J., Liss, P. S., Mahowald, N., Prospero, J. M., Ridgwell, A. J., Tegen, I., and Torres, R.: Global iron connections between desert dust, ocean biogeochemistry, and climate, Science, 308, 67-71, 2005.

Johnson, B. T., and Osborne, S. R.: Physical and optical properties of mineral dust aerosol measured by aircraft during the GERBILS campaign, Q J Roy Meteor Soc, 137, 1117-1130, Doi 10.1002/Qj.777, 2011.
Jones, C., Mahowald, N., and Luo, C.: The role of easterly waves on African desert dust transport, J Climate, 16, 3617-3628, Doi 10.1175/1520-0442(2003)016<3617:Troewo>2.0.Co;2, 2003.
Kandler, K., Schutz, L., Deutscher, C., Ebert, M., Hofmann, H., Jäckel, S., Jaenicke, R., Knippertz, P., Lieke, K., Massling, A., Petzold, A., Schladitz, A., Weinzierl, B., Wiedensohler, A., Zorn, S., and Weinbruch, S.: Size distribution, mass concentration, chemical and mineralogical composition and derived optical parameters of the boundary layer aerosol at Tinfou, Morocco, during SAMUM 2006, Tellus B, 61, 32-50, DOI 10.1111/j.1600-0889.2008.00385.x, 2009.
Kandler, K., Lieke, K., Benker, N., Emmel, C., Kupper, M., Muller-Ebert, D., Ebert, M., Scheuvens, D., Schladitz, A., Schutz, L., and Weinbruch, S.: Electron microscopy of particles collected at Praia, Cape Verde, during the Saharan Mineral Dust Experiment: particle chemistry, shape, mixing state and complex refractive index, Tellus B, 63, 475-496, DOI 10.1111/j.1600-0889.2011.00550.x, 2011a.
Kandler, K., Schutz, L., Jackel, S., Lieke, K., Emmel, C., Muller-Ebert, D., Ebert, M., Scheuvens, D., Schladitz, A., Segvic, B., Wiedensohler, A., and Weinbruch, S.: Ground-based off-line aerosol measurements at Praia, Cape Verde, during the Saharan Mineral Dust Experiment: microphysical properties and mineralogy, Tellus B, 63, 459-474, 10.1111/j.1600-0889.2011.00546.x, 2011b.
Karyampudi, V. M., Palm, S. P., Reagen, J. A., Fang, H., Grant, W. B., Hoff, R. M., Moulin, C., Pierce, H. F., Torres, O., Browell, E. V., and Melfi, S. H.: Validation of the Saharan dust plume conceptual model using lidar, Meteosat, and ECMWF data, B Am Meteorol Soc, 80, 1045-1075, 1999.
Kim, D., Chin, M., Yu, H. B., Diehl, T., Tan, Q., Kahn, R. A., Tsigaridis, K., Bauer, S. E., Takemura, T., Pozzoli, L., Bellouin, N., Schulz, M., Peyridieu, S., Chedin, A., and Koffi, B.: Sources, sinks, and transatlantic transport of North African dust aerosol: A multimodel analysis and comparison with remote sensing data, J Geophys Res-Atmos, 119, 6259-6277, 10.1002/2013jd021099, 2014.
Kinne, S., Schulz, M., Textor, C., Guibert, S., Balkanski, Y., Bauer, S. E., Berntsen, T., Berglen, T. F., Boucher, O., Chin, M., Collins, W., Dentener, F., Diehl, T., Easter, R., Feichter, J., Fillmore, D., Ghan, S., Ginoux, P., Gong, S., Grini, A., Hendricks, J. E., Herzog, M., Horowitz, L., Isaksen, I., Iversen, T., Kirkavag, A., Kloster, S., Koch, D., Kristjansson, J. E., Krol, M., Lauer, A., Lamarque, J. F., Lesins, G., Liu, X., Lohmann, U., Montanaro, V., Myhre, G., Penner, J. E., Pitari, G., Reddy, S., Seland, O., Stier, P., Takemura, T., and Tie, X.: An AeroCom initial assessment - optical properties in aerosol component modules of global models, Atmos Chem Phys, 6, 1815-1834, DOI 10.5194/acp-6-1815-2006, 2006.
Klaver, A., Formenti, P., Caquineau, S., Chevaillier, S., Ausset, P., Calzolai, G., Osborne, S., Johnson, B., Harrisone, M., and Dubovik, O.: Physico-chemical and optical properties of Sahelian and Saharan mineral dust: in situ measurements during the GERBILS campaign, Q J Roy Meteor Soc, 137, 1193-1210, Doi 10.1002/Qj.889, 2011.
Kok, J. F., Ridley, D. A., Zhou, Q., Miller, R. L., Zhao, C., Heald, C. L., Ward, D. S., Albani, S., and Haustein, K.: Smaller desert dust cooling effect estimated from analysis of dust size and abundance, Nat Geosci, 10, 274-278, 10.1038/Ngeo2912, 2017.
Korolev, A., Emery, E., and Creelman, K.: Modification and Tests of Particle Probe Tips to Mitigate Effects of Ice Shattering, J Atmos Ocean Tech, 30, 690-708, 10.1175/Jtech-D-12-00142.1, 2013.
Kumar, P., Sokolik, I. N., and Nenes, A.: Cloud condensation nuclei activity and droplet activation kinetics of wet processed regional dust samples and minerals, Atmos Chem Phys, 11, 8661-8676, 10.5194/acp-11-8661-2011, 2011.
Lavaysse, C., Chaboureau, J. P., and Flamant, C.: Dust impact on the West African heat low in summertime, Q J Roy Meteor Soc, 137, 1227-1240, Doi 10.1002/Qj.844, 2011.
Lensky, I. M., and Rosenfeld, D.: Clouds-Aerosols-Precipitation Satellite Analysis Tool (CAPSAT), Atmos Chem Phys, 8, 6739-6753, 2008.
Li, C., Krotkov, N. A., Dickerson, R. R., Li, Z. Q., Yang, K., and Chin, M.: Transport and evolution of a pollution plume from northern China: A satellite-based case study, J Geophys Res-Atmos, 115, 10.1029/2009jd012245, 2010.
Li, J. M., and Osada, K. Z.: Preferential settling of elongated mineral dust particles in the atmosphere, Geophys Res Lett, 34, 10.1029/2007gl030262, 2007.
Lindqvist, H., Jokinen, O., Kandler, K., Scheuvens, D., and Nousiainen, T.: Single scattering by realistic, inhomogeneous mineral dust particles with stereogrammetric shapes, Atmos Chem Phys, 14, 143-157, 10.5194/acp-14-143-2014, 2014.
Lindsley, W. G.: Filter Pore Size and Aerosol Sample Collection, in: NIOSH Manual of Analytical Methods, 5th ed., NIOSH, Cincinnati, Ohio., 2016.
Liu, D. T., Taylor, J., Crosier, J., Marsden, N., Bower, K. N., Lloyd, G., Ryder, C. L., Brooke, J. K., Cotton, R., Marenco, F., Blyth, A., Cui, Z. Q., Estelles, V., Gallagher, M., Coe, H., and Choularton, T. W.: Aircraft and ground measurements of dust aerosols over the west African coast in summer 2015 during ICE-D and AER-D, Atmos Chem Phys, 18, 3817-3838, 10.5194/acp-18-3817-2018, 2018.
Long, L. L., Querry, M. R., Bell, R. J., and Alexander, R. W.: Optical-Properties of Calcite and Gypsum in Crystalline and Powdered Form in the Infrared and Far-Infrared, Infrared Phys, 34, 191-201, Doi 10.1016/0020-0891(93)90008-U, 1993.
Mahowald, N., Albani, S., Kok, J. F., Engelstaeder, S., Scanza, R., Ward, D. S., and Flanner, M. G.: The size distribution of desert dust aerosols and its impact on the Earth system, Aeolian Res, 15, 53-71, 10.1016/j.aeolia.2013.09.002, 2014.
Marenco, F., Ryder, C. L., Estelles, V., O'Sullivan, D., Brooke, J., and Orgill, L.: Unusual vertical structure of the Saharan Air Layer and giant dust particles during AER-D, Atmospheric Chemistry and Physics Discussions, https://doi.org/10.5194/acp-2018-758, 2018, in review.

Maring, H., Savoie, D. L., Izaguirre, M. A., Custals, L., and Reid, J. S.: Mineral dust aerosol size distribution change during atmospheric transport, J Geophys Res-Atmos, 108, Doi 10.1029/2002jd002536, 2003.
Markwardt, C. B.: Non-Linear Least Squares Fitting in IDL with MPFIT, ASP Conference Series ADASS XVIII, Quebec, Canada, 2008, 251-254, 2008.
Marra, A., Blanco, A., Fonti, S., Jurewicz, A., and Orofino, V.: Fine hematite particles of Martian interest: Absorption spectra and optical constants, Journal of Physics: Conference Series, 6, 10.1088/1742-6596/6/1/013, 2005.
Marsham, J. H., Knippertz, P., Dixon, N. S., Parker, D. J., and Lister, G. M. S.: The importance of the representation of deep convection for modeled dust-generating winds over West Africa during summer, Geophys Res Lett, 38, Doi 10.1029/2011gl048368, 2011.
Marsham, J. H., Hobby, M., Allen, C. J. T., Banks, J. R., Bart, M., Brooks, B. J., Cavazos-Guerra, C., Engelstaedter, S., Gascoyne, M., Lima, A. R., Martins, J. V., McQuaid, J. B., O'Leary, A., Ouchene, B., Ouladichir, A., Parker, D. J., Saci, A., Salah-Ferroudj, M., Todd, M. C., and Washington, R.: Meteorology and dust in the central Sahara: Observations from Fennec supersite-1 during the June 2011 Intensive Observation Period, J Geophys Res-Atmos, 118, 4069-4089, 10.1002/jgrd.50211, 2013.
McConnell, C. L., Highwood, E. J., Coe, H., Formenti, P., Anderson, B., Osborne, S., Nava, S., Desboeufs, K., Chen, G., and Harrison, M. A. J.: Seasonal variations of the physical and optical characteristics of Saharan dust: Results from the Dust Outflow and Deposition to the Ocean (DODO) experiment, J Geophys Res-Atmos, 113, Doi 10.1029/2007jd009606, 2008.
McConnell, C. L., Formenti, P., Highwood, E. J., and Harrison, M. A. J.: Using aircraft measurements to determine the refractive index of Saharan dust during the DODO Experiments, Atmos Chem Phys, 10, 3081-3098, DOI 10.5194/acp-10-3081-2010, 2010.
McFarquhar, G. M., Baumgardner, D., Bansemer, A., Abel, S. J., Crosier, J., French, J., Rosenberg, P., Korolev, A., Schwarzoenboeck, A., Leroy, D., Um, J., Wu, W., Heymsfield, A. J., Twohy, C., Detwiler, A., Field, P., Neumann, A., Cotton, R., Axisa, D., and Dong, J. Y.: Processing of Ice Cloud In Situ Data Collected by Bulk Water, Scattering, and Imaging Probes: Fundamentals, Uncertainties, and Efforts toward Consistency, Meteor Mon, 58, 10.1175/Amsmonographs-D-16-0007.1, 2017.
Middleton, N. J.: Desert dust hazards: A global review, Aeolian Res, 24, 53-63, 10.1016/j.aeolia.2016.12.001, 2017.
Moosmuller, H., Engelbrecht, J. P., Skiba, M., Frey, G., Chakrabarty, R. K., and Arnott, W. P.: Single scattering albedo of fine mineral dust aerosols controlled by iron concentration, J Geophys Res-Atmos, 117, Artn D11210 10.1029/2011jd016909, 2012.
Nousiainen, T.: Optical modeling of mineral dust particles: A review, J Quant Spectrosc Ra, 110, 1261-1279, 10.1016/j.jqsrt.2009.03.002, 2009.
O'Sullivan, D., Ryder, C. L., Pradhan, Y., Kipling, Z., Johnson, B., Benedetti, A., Marenco, F., Brooks, M., McGill, M., Yorks, P., and Selmer, P.: Models transport Saharan dust too low in the atmosphere compared to observations from the AER-D field campaign, in preparation.
Ogren, J. A.: Comment on Calibration and Intercomparison of Filter-Based Measurements of Visible Light Absorption by Aerosols, Aerosol Sci Tech, 44, 589-591, Doi:10.1080/02786826.2010.482111, 2010.
Osborne, S. R., Johnson, B. T., Haywood, J. M., Baran, A. J., Harrison, M. A. J., and McConnell, C. L.: Physical and optical properties of mineral dust aerosol during the Dust and Biomass-burning Experiment, J Geophys Res-Atmos, 113, Doi 10.1029/2007jd009551, 2008.
Otto, S., Bierwirth, E., Weinzierl, B., Kandler, K., Esselborn, M., Tesche, M., Schladitz, A., Wendisch, M., and Trautmann, T.: Solar radiative effects of a Saharan dust plume observed during SAMUM assuming spheroidal model particles, Tellus B, 61, 270-296, DOI 10.1111/j.1600-0889.2008.00389.x, 2009.
Otto, S., Trautmann, T., and Wendisch, M.: On realistic size equivalence and shape of spheroidal Saharan mineral dust particles applied in solar and thermal radiative transfer calculations, Atmos Chem Phys, 11, 4469-4490, 10.5194/acp-11-4469-2011, 2011.
Peterson, J. T., and Weinman, J. A.: Optical properties of quartz dust particles at infrared wavelengths, J Geophys Res, 74, 6947-6952, https://doi.org/10.1029/JC074i028p06947, 1969.
Piedra, P., and Moosmuller, H.: Optical losses of photovoltaic cells due to aerosol deposition: Role of particle refractive index and size, Sol Energy, 155, 637-646, 10.1016/j.solener.2017.06.047, 2017.
Price, H. C., Baustian, K. J., McQuaid, J. B., Blyth, A., Bower, K. N., Choularton, T., Cotton, R. J., Cui, Z., Field, P. R., Gallagher, M., Hawker, R., Merrington, A., Miltenberger, A., Neely, R. R., Parker, S. T., Rosenberg, P. D., Taylor, J. W., Trembath, J., Vergara-Temprado, J., Whale, T. F., Wilson, T. W., Young, G., and Murray, B. J.: Atmospheric Ice-Nucleating Particles in the Dusty Tropical Atlantic, J Geophys Res-Atmos, 123, 2175-2193, 10.1002/2017jd027560, 2018.
Prospero, J. M., and Carlson, T. N.: Vertical and Areal Distribution of Saharan Dust over Western Equatorial North-Atlantic Ocean, J Geophys Res, 77, 5255-&, DOI 10.1029/JC077i027p05255, 1972.
Prospero, J. M., Collard, F. X., Molinie, J., and Jeannot, A.: Characterizing the annual cycle of African dust transport to the Caribbean Basin and South America and its impact on the environment and air quality, Global Biogeochem Cy, 28, 757-773, 10.1002/2013gb004802, 2014.
Querry, M. R., Osborne, G., Lies, K., Jordon, R., and Coveney, R. M.: Complex Refractive-Index of Limestone in Visible and Infrared, Appl Optics, 17, 353-356, Doi 10.1364/Ao.17.000353, 1978.
Querry, M. R.: Optical constants of minerals and other materials from the millimeter to the UV, US Army, Aberdeen, MD, USA, 1987.

Roberts, A. J., Marsham, J. H., Knippertz, P., Parker, D. J., Bart, M., Garcia-Carreras, L., Hobby, M., McQuaid, J. B., Rosenberg, P. D., and Walker, D.: New Saharan wind observations reveal substantial biases in analysed dust-generating winds, Atmos Sci Lett, 18, 366-372, 10.1002/asl.765, 2017.

Rocha-Lima, A., Martins, J. V., Remer, L. A., Todd, M., Marsham, J. H., Engelstaedter, S., Ryder, C. L., Cavazos-Guerra, C., Artaxo, P., Colarco, P., and Washington, R.: A detailed characterization of the Saharan dust collected during the Fennec campaign in 2011: in situ ground-based and laboratory measurements, Atmos Chem Phys, 18, 1023-1043, 10.5194/acp-18-1023-2018, 2018.

Rosenberg, P., Dean, A., Williams, P., Minikin, A., Pickering, M., and Petzold, A.: Particle sizing calibration with refractive index correction for light scattering optical particle counters and impacts upon PCASP and CDP data collected during the Fennec campaign, Atmospheric Measurement Technique Discussions, 5, 97-135, doi:10.5194/amtd-5-97-2012, 2012.

Ryder, C. L., Highwood, E. J., Lai, T. M., Sodemann, H., and Marsham, J. H.: Impact of atmospheric transport on the evolution of microphysical and optical properties of Saharan dust, Geophys Res Lett, 40, 2433-2438, Doi 10.1002/Grl.50482, 2013a.

Ryder, C. L., Highwood, E. J., Rosenberg, P. D., Trembath, J., Brooke, J. K., Bart, M., Dean, A., Crosier, J., Dorsey, J., Brindley, H., Banks, J., Marsham, J. H., McQuaid, J. B., Sodemann, H., and Washington, R.: Optical properties of Saharan dust aerosol and contribution from the coarse mode as measured during the Fennec 2011 aircraft campaign, Atmos Chem Phys, 13, 303-325, DOI 10.5194/acp-13-303-2013, 2013b.

Ryder, C. L., McQuaid, J. B., Flamant, C., Rosenberg, P. D., Washington, R., Brindley, H. E., Highwood, E. J., Marsham, J. H., Parker, D. J., Todd, M. C., Banks, J. R., Brooke, J. K., Engelstaedter, S., Estelles, V., Formenti, P., Garcia-Carreras, L., Kocha, C., Marenco, F., Sodemann, H., Allen, C. J. T., Bourdon, A., Bart, M., Cavazos-Guerra, C., Chevaillier, S., Crosier, J., Darbyshire, E., Dean, A. R., Dorsey, J. R., Kent, J., O'Sullivan, D., Schepanski, K., Szpek, K., Trembath, J., and Woolley, A.: Advances in understanding mineral dust and boundary layer processes over the Sahara from Fennec aircraft observations, Atmos Chem Phys, 15, 8479-8520, 10.5194/acp-15-8479-2015, 2015.

Schepanski, K., Heinold, B., and Tegen, I.: Harmattan, Saharan heat low, and West African monsoon circulation: modulations on the Saharan dust outflow towards the North Atlantic, Atmos Chem Phys, 17, 10223-10243, 10.5194/acp-17-10223-2017, 2017.

Scheuvens, D., Schutz, L., Kandler, K., Ebert, M., and Weinbruch, S.: Bulk composition of northern African dust and its source sediments - A compilation, Earth-Sci Rev, 116, 170-194, 10.1016/j.earscirev.2012.08.005, 2013.

Seinfeld, J. H., and Pandis, S. N.: Properties of the Atmospheric Aerosol, in: Atmospheric Chemistry and Physics: From Air Pollution to Climate Change, 2nd ed., John Wiley & Sons, New Jersey, USA, 350-388, 2006.

Shettle, E. P., and Fenn, R. W.: Models for the Aerosols of the Lower Atmosphere and the Effects of Humidity Variations on Their Optical Properties, Air Force Geophysics Laboratory Environmental Research Papers, Hanscomb, MA, 1979.

Sodemann, H., Lai, T. M., Marenco, F., Ryder, C. L., Flamant, C., Knippertz, P., Rosenberg, P., Bart, M., and McQuaid, J. B.: Lagrangian dust model simulations for a case of moist convective dust emission and transport in the western Sahara region during Fennec/LADUNEX, J Geophys Res-Atmos, 120, 6117-6144, 10.1002/2015jd023283, 2015.

Song, Q., Zhang, Z., Yu, H., Kato, S., Yang, P., Colarco, P. R., Remer, L. A., and Ryder, C. L.: Toward an Observation-Based Estimate of Dust Net Radiative Effects in Tropical North Atlantic Through Integrating Satellite Observations and In Situ Measurements of Dust Properties, Atmospheric Chemistry and Physics Discussions, https://doi.org/10.5194/acp-2018-267, in review, 2018.

Song, Q. Q., Zhang, Z. B., Yu, H. B., Kato, S., Yang, P., Colarco, P., Remer, L. A., and Ryder, C. L.: Net radiative effects of dust in the tropical North Atlantic based on integrated satellite observations and in situ measurements, Atmos Chem Phys, 18, 11303-11322, 10.5194/acp-18-11303-2018, 2018.

Stein, A. F., Draxler, R. R., Rolph, G. D., Stunder, B. J. B., Cohen, M. D., and Ngan, F.: Noaa's Hysplit Atmospheric Transport and Dispersion Modeling System, B Am Meteorol Soc, 96, 2059-2077, 10.1175/Bams-D-14-00110.1, 2015.

Stevenson, J. A., Millington, S. C., Beckett, F. M., Swindles, G. T., and Thordarson, T.: Big grains go far: understanding the discrepancy between tephrochronology and satellite infrared measurements of volcanic ash, Atmos Meas Tech, 8, 2069-2091, 10.5194/amt-8-2069-2015, 2015.

Strong, J. D. O., Vecchi, G. A., and Ginoux, P.: The Climatological Effect of Saharan Dust on Global Tropical Cyclones in a Fully Coupled GCM, J Geophys Res-Atmos, 123, 5538-5559, 10.1029/2017jd027808, 2018.

Tegen, I., and Fung, I.: Modeling of Mineral Dust in the Atmosphere - Sources, Transport, and Optical-Thickness, J Geophys Res-Atmos, 99, 22897-22914, Doi 10.1029/94jd01928, 1994.

Tegen, I., and Lacis, A. A.: Modeling of particle size distribution and its influence on the radiative properties of mineral dust aerosol, J Geophys Res-Atmos, 101, 19237-19244, Doi 10.1029/95jd03610, 1996.

Toon, O. B., Pollack, J. B., and Khare, B. N.: Optical-Constants of Several Atmospheric Aerosol Species - Ammonium-Sulfate, Aluminum-Oxide, and Sodium-Chloride, J Geophys Res-Oc Atm, 81, 5733-5748, DOI 10.1029/JC081i033p05733, 1976.

Trembath, J.: Airborne CCN Measurements, Doctor of Philosophy, Faculty of Engineering and Physical Science, University of Manchester, 2012.

Trzeciak, T. M., Garcia-Carreras, L., and Marsham, J. H.: Cross-Saharan transport of water vapor via recycled cold pool outflows from moist convection, Geophys Res Lett, 44, 1554-1563, 10.1002/2016gl072108, 2017.

Turnbull, K.: PSAP Corrections, Met Office, OBR, UK Met Office, Exeter, UK, Technical Note No. 80, http://www.faam.ac.uk/index.php/component/docman/cat_view/140-science-instruments, 2010.
Ulanowski, Z., Bailey, J., Lucas, P. W., Hough, J. H., and Hirst, E.: Alignment of atmospheric mineral dust due to electric field, Atmos Chem Phys, 7, 6161-6173, DOI 10.5194/acp-7-6161-2007, 2007.
Volz, F. E.: Infrared Optical-Constants of Ammonium Sulfate, Sahara Dust, Volcanic Pumice, and Flyash, Appl Optics, 12, 564-568, Doi 10.1364/Ao.12.000564, 1973.
Weigel, R., Spichtinger, P., Mahnke, C., Klingebiel, M., Afchine, A., Petzold, A., Kramer, M., Costa, A., Molleker, S., Reutter, P., Szakall, M., Port, M., Grulich, L., Jurkat, T., Minikin, A., and Borrmann, S.: Thermodynamic correction of particle concentrations measured by underwing probes on fast-flying aircraft, Atmos Meas Tech, 9, 5135-5162, 10.5194/amt-9-5135-2016, 2016.
Weinzierl, B., Petzold, A., Esselborn, M., Wirth, M., Rasp, K., Kandler, K., Schütz, L., Koepke, P., and Fiebig, M.: Airborne measurements of dust layer properties, particle size distribution and mixing state of Saharan dust during SAMUM 2006, Tellus B, 61, 96-117, DOI 10.1111/j.1600-0889.2008.00392.x, 2009.
Weinzierl, B., Sauer, D., Esselborn, M., Petzold, A., Veira, A., Rose, M., Mund, S., Wirth, M., Ansmann, A., Tesche, M., Gross, S., and Freudenthaler, V.: Microphysical and optical properties of dust and tropical biomass burning aerosol layers in the Cape Verde region-an overview of the airborne in situ and lidar measurements during SAMUM-2, Tellus B, 63, 589-618, DOI 10.1111/j.1600-0889.2011.00566.x, 2011.
Weinzierl, B., Ansmann, A., Prospero, J. M., Althausen, D., Benker, N., Chouza, F., Dollner, M., Farrell, D., Fomba, W. K., Freudenthaler, V., Gasteiger, J., Gross, S., Haarig, M., Heinold, B., Kandler, K., Kristensen, T. B., Mayol-Bracero, O. L., Muller, T., Reitebuch, O., Sauer, D., Schafler, A., Schepanski, K., Spanu, A., Tegen, I., Toledano, C., and Walser, A.: The Saharan Aerosol Long-range Transport and Aerosol-cloud-interaction experiment: Overview and Selected Highlights, B Am Meteorol Soc, 98, 1427-1451, 10.1175/Bams-D-15-00142.1, 2017.
Woodage, M. J., and Woodward, S.: UK HiGEM: Impacts of Desert Dust Radiative Forcing in a High-Resolution Atmospheric GCM, J Climate, 27, 5907-5928, 10.1175/Jcli-D-13-00556.1, 2014.
Yu, H. B., Chin, M., Yuan, T. L., Bian, H. S., Remer, L. A., Prospero, J. M., Omar, A., Winker, D., Yang, Y. K., Zhang, Y., Zhang, Z. B., and Zhao, C.: The fertilizing role of African dust in the Amazon rainforest: A first multiyear assessment based on data from Cloud-Aerosol Lidar and Infrared Pathfinder Satellite Observations, Geophys Res Lett, 42, 1984-1991, 10.1002/2015gl063040, 2015.

Tables and Figures

Campaign	Acronym	Fieldwork Date	Location	Measurement upper size limit, µm	Instrument type	In-cabin or wing-mounted	Details	Publication
Dust And Biomass burning Experiment	DABEX	2006	Niger	10	OPC	In-cabin	PCASP-X, behind a counter-flow virtual impactor with significant pipework; loss of majority of coarse particles	Osborne et al. (2008)
				10	Filter samples	In-cabin	~~i~~Inlet restricted measurements to 35% of coarse mode (d>1.4 µm)	Chou et al. (2008)
Dust Outflow and Deposition to the Ocean 2	DODO2	Aug 2006	Tropical Eastern Atlantic	40	OPC	Wing-mounted	CDP measurements on a few flights only; otherwise size distributions up to 3 µm	~~McConnell et al., 2008~~McConnell et al. (2008)
African Monsoon Multidisciplinary Analysis	AMMA	Jun-Jul 2006	Niger and Benin	20	OPC	In-cabin	Grimm OPC behind isokinetic inlet with 50% passing efficiency at 9 µm	Formenti et al. (2011a)
NASA AMMA	NAMMA	Aug-Sep 2006	Tropical Eastern Atlantic	5	APS	In-cabin	APS behind an inlet with 50% sampling efficiency at 5 µm	Chen et al. (2011)
Saharan Mineral Dust Experiment 1	SAMUM1	May-Jun 2006	Morocco	30/100	OPCs	Wing-mounted	FSSP-300/FSSP-100	Weinzierl et al. (2009)
Geostationary Earth Radiation Budget Intercomparison of Longwave and Shortwave radiation	GERBILS	Jun 2007	Mali, Southern Mauritania	60	OPC	Wing-mounted	SID-2. PSDs represent aged, transported dust events with light dust loadings	~~Johnson and Osborne, 2011~~Johnson and Osborne (2011)
Saharan Mineral Dust Experiment 2	SAMUM2	Jan-Feb 2008	Tropical Eastern Atlantic	30	OPC	Wing-mounted	FSSP-300	~~Weinzierl et al., 2011~~Weinzierl et al. (2011)
Fennec – The Saharan Climate System	Fennec	Jun 2011	Mali, Mauritania	50/60/930	OPCs and OAPs	Wing-mounted	CDP/SID2/CIP15	~~Ryder et al., 2013b~~Ryder et al. (2013b)
Aerosol Direct Radiative Impact on the regional climate in the MEDiterranean region	ADRIMED	Jun-Jul 2013	Mediterranean Sea	20	OPC	Wing-mounted	FSSP-300	Denjean et al. (2016)
Saharan Aerosol Long-range Transport and Aerosol-Cloud-Interaction Experiment	SALTRACE	Jun-Jul 2013	Tropical Western Atlantic	50~~30~~/100	OPCs	Wing-mounted	CAS-DPOL/FSSP-13~~00~~. Some measurements additionally taken over the Eastern Tropical Atlantic	~~Weinzierl et al., 2017~~Weinzierl et al. (2017)
AERosol Properties – Dust	AER-D	Aug 2015	Tropical Eastern Atlantic	100	OPCs and OAPs	Wing-mounted	CDP, CIP15 and 2DS	This article

Table 1: Airborne campaigns measuring size distributions of Saharan mineral dust since 2006, showing maximum particle size measured and size restrictions by inlets where instruments were located inside the aircraft cabin. OPC size ranges are nominal diameters. See text for acronym details. Instrument acronyms can be found in the Appendix.

5

Flight Number	Date	Times of in-situ sampling (UTC)	Accumulation Mode 550 nm AOD	General Flight Aims and Conditions
b920	7 Aug 2015	15:00 – 17:00	0.4	In-situ and remote sensing, CATS underflight
b923	12 Aug 2015		1.8*	High-level remote sensing of dust, mapping of intense dust event, Cape Verde to Fuerteventura, Canary Islands
b924	12 Aug 2015	15:30-16:30	2.5	In-situ and remote sensing of intense dust event, Fuerteventura, Canary Islands to Cape Verde.
b928	16 Aug 2015	15:00-18:00	0.8	~~SAVEX~~SAVEX-D flight 1; in-situ and remote sensing close to Praia ground site
b932	20 Aug 2015	11:00-12:00	0.7	In-situ and remote sensing
b934	25 Aug 2015	15:00-17:45	0.6	~~SAVEX~~SAVEX-D flight 2; in-situ and remote sensing close to Sal ground site

Table 2: Dates of AER-D flights and times of intensive in-situ sampling ~~legs~~SLRs, and accumulation mode AOD at the region of in-situ sampling. *No in-situ sampling, AOD is provided at the Canary Islands.

Instrument	Abbreviation	Wavelength, nm	Scattering angle, degrees (primary, secondary)	Nominal size range measured, µm diameter	Corrected size range, µm diameter	Measurement method
Passive Cavity Aerosol Spectrometer Probe 100-X	PCASP	632.8	35-120, 60-145	0.1-3.0	0.12-3.02	Light scattering
Cloud Droplet Probe	CDP	658	1.7-14	3-50	3.4-95.4	Light scattering
Cloud Imaging Probe 15	CIP15	642	n/a	15-930	n/a	Light Shadowing
Two-Dimensional Stereo Probe	2DS		n/a	10-1280	n/a	Light Shadowing
Cloud Imaging Probe 100	CIP100		n/a	100-6200	n/a	Light Shadowing

Table 3: Wing mounted Size Distribution instrumentation operated during AER-D.

Flight	Uplift number	Event driving uplift	Time and date of uplift	Uplift longitude centre	Uplift latitude centre	Age at aircraft sampling, days
b920	n/a	MCS and haboob	2 Aug 15:00Z ~~2 Aug~~ to 3 Aug 07:00Z ~~3 Aug~~	3.0	23.5	3.9 to 4.6
b923/b924	n/a	MCS and haboob	10 Aug 10:00Z ~~10 Aug~~ to 10 Aug 19:00Z ~~10 Aug~~	~~1.5~~=1.0	~~2.5~~21.0	1.9 to 2.2
b928	1	Convection under widespread patchy cloud	13 Aug 12:00Z ~~13 Aug~~ to 14 Aug 10:00 ~~14 Aug~~	-8.5	23.0	2.2 to 3.1
	2	MCS and haboob	14 Aug 19:00Z ~~14 Aug~~ to 15 Aug 05:00 ~~15 Aug~~	-2.2	20.4	1.4 to 1.8
b932	1	MCS and haboob	17 Aug 10:00Z ~~17 Aug~~ to 18 Aug 01:00Z ~~18 Aug~~	-1.5	21.5	2.4 to 3.0
	2	Small scale local convection	18 Aug 12:00Z ~~18 Aug~~ to 18 Aug 14:00Z ~~18 Aug~~	-5.0	~~-~~24.5	1.9 to 2.0
b934	1	Small scale convection and haboob	22 Aug 21:00Z ~~22 Aug~~ to 23 Aug 03:00Z ~~23 Aug~~	-1.3	22.5	2.6 to 2.9
	2	Small scale convection and haboob	23 Aug 22:00Z ~~23 Aug~~ to 24 Aug 01:00Z ~~24 Aug~~	-6.0	20.0	1.6 to 1.7
	3	Small scale convection and haboob	24 Aug 20:00Z ~~24 Aug~~ to 24 Aug 23:00Z ~~24 Aug~~	-13.0	~~-~~19.5	0.7 to 0.8

Table 4: Details of dust uplift events determined from SEVIRI RGB imagery driving dust sampled by the aircraft. Uplift numbers correspond to primary, secondary or tertiary uplift, also indicated in Figure 1.

			Mode 1	Mode 2	Mode 3	Mode 4
SAL	d_{pg}	Mean	0.105	0.851	1.580	32.527
	σ_g		2.200	1.181	1.928	1.528
	N_{tot}		3.91×10^{2}	8.39×10^{0}	1.16×10^{1}	1.38×10^{-4}
	d_{pg}	Min	0.142	0.838	2.176	10.643
	σ_g		1.658	1.262	1.585	1.300
	N_{tot}		1.14×10^{2}	2.80×10^{0}	1.52×10^{0}	4.44×10^{-3}
	d_{pg}	Max	0.089	0.576	1.571	15.421
	σ_g		2.200	1.500	1.957	1.877
	N_{tot}		1.14×10^{3}	2.32×10^{2}	5.47×10^{1}	3.75×10^{-3}
MBL	d_{pg}	Mean	0.148	0.487	3.675	7.651
	σ_g		1.437	1.900	1.392	2.000
	N_{tot}		3.14×10^{2}	1.42×10^{1}	1.38×10^{0}	1.08×10^{-2}
	d_{pg}	Min	0.133	0.686	3.288	10.457
	σ_g		1.483	1.500	1.500	1.300
	N_{tot}		1.35×10^{2}	2.39×10^{0}	6.60×10^{-1}	1.27×10^{-3}
	d_{pg}	Max	0.151	0.458	3.144	7.651
	σ_g		1.423	1.872	1.491	2.000
	N_{tot}		4.86×10^{2}	2.81×10^{1}	2.88×10^{0}	2.32×10^{-2}

Table 5: Lognormal Mode Properties for the number size distribution. Diameters are given in microns, number concentrations in ambient cm^{-3}.

	SAL Mean (min, max)	MBL Mean (min, max)
MEC, m^2g^{-1}	0.32 (0.27,0.35)	0.25 (0.22, 0.29)
SSA	0.95 (0.91,0.98)	0.99 (0.97,0.99)
g	0.74 (0.74, 0.74)	0.73 (0.71, 0.74)
σ_e, Mm^{-1}	220 (38, 1148)	77 (27, 139)
d~~D~~$_{eff,}$ µm	4.0 (3.6, 4.7)	4.6 (3.4, 5.5)
VMD, µm	5.5 (5.0, 6.3)	6.0 (5.7, 6.3)

Table 6: Optical and Size Properties for the AER-D SAL and MBL campaign minimum, mean and maximum: Optical properties of Mass Extinction Coefficient (MEC), single scattering albedo (SSA), asymmetry parameter (g) and Extinction coefficient (σ_e) are given at 550nm. Effective diameter (d_{eff}) and Volume Median Diameter (VMD) are calculated directly from the 2DS XY PSD; optical properties are calculated using the same PSDs and ~~derived~~ iterated RIs for each ~~flight leg~~SLR.

Size range, µm diameter	Sample ID	B920 R2	B928 R2	B920 R5	B934 R6
	Layer type	MBL	MBL	SAL	SAL
FULL PSD	m	1.46	1.48	1.48	1.48
	k	0.0004	0.0005	0.0030	0.0012
ACC PSD	m	1.47	1.49	1.48	1.48
	k	0.0014	0.0010	0.0023	0.0023
0.1-0.5	m	1.49	1.54	1.52	1.53
	k	0.0002	0.0005	0.0021	0.0009
0.5-1.0	m	1.48	1.50	1.49	1.51
	k	0.0007	0.0004	0.0026	0.0039
1-2.5	m	1.47	1.48	1.48	1.48
	k	0.0015	0.0010	0.0023	0.0023
2.5-5.0	m	1.47	1.48	1.49	1.49
	k	0.0003	0.0016	0.0031	0.0027
5-10	m	1.45	1.48	1.49	1.47
	k	0.0004	0.0003	0.0034	0.0003
10-40	m	1.47	1.47	n/a	n/a
	k	0.0003	0.0003	n/a	n/a

Table 7: Complex refractive indices at 550 nm derived from filter sample composition assuming internal mixing. Real part (m) and imaginary part (k). Values are given for the full size distribution (full PSD), accumulation mode PSD (d<2.5 µm), and as a function of diameter range given.

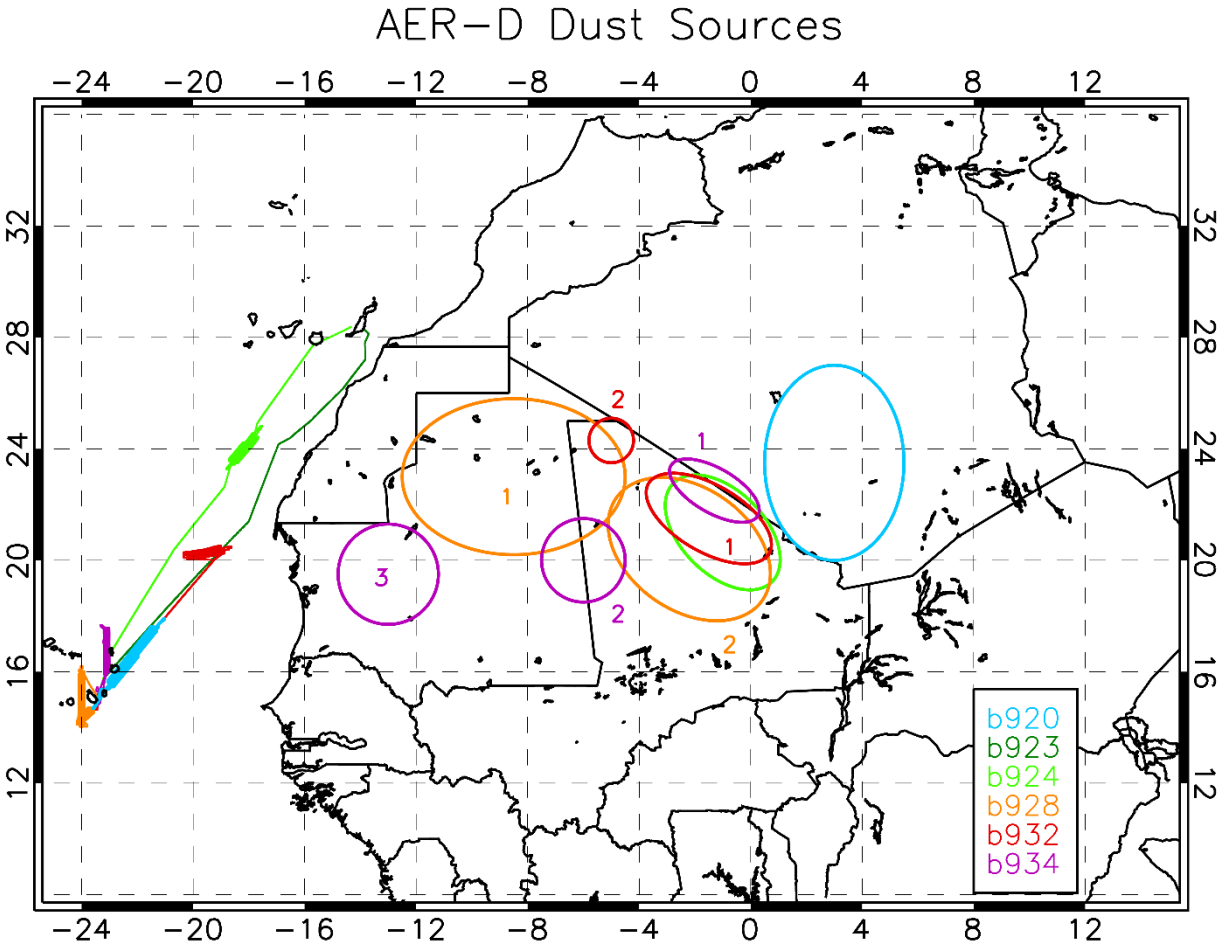

Figure 1: Map showing the location of the AER-D flights, based out of Praia on Cape Verde. Thin lines show full flight tracks, bold sections indicate in-situ sampling ~~legs~~ SLRs analysed here. Note that within each flight there were several ~~legs~~ SLRs at different altitudes, which overlay each other here. Circles indicate dust source locations. Numbers indicate primary, secondary and tertiary dust uplift (see Table 4) events. Note that flights b923/b924 sampled the same dust event.

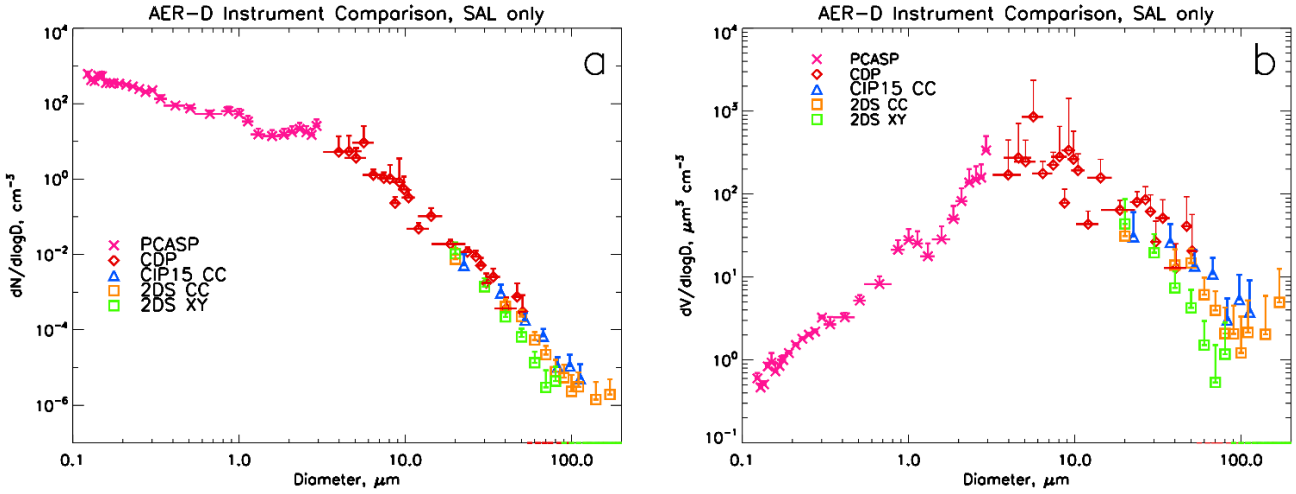

Figure 2: Comparison of mean size distributions in the SAL during AER-D from different instruments and different sizing metrics. For clarity only upper error bounds are shown. Horizontal error bars represent maximum bin width due to uncertainties in both bin centre and bin width.

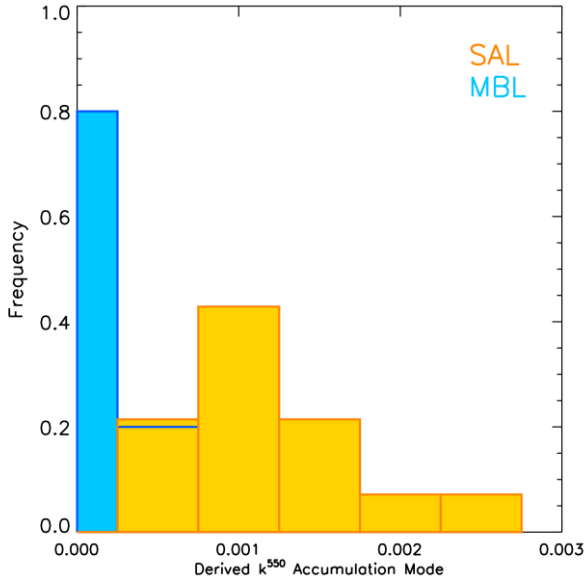

Figure 3: Histogram of derived imaginary part of the refractive index at 550 nm (k^{550}) from iterations for the accumulation mode, shown separately for ~~legs~~ SLRs in the SAL and MBL.

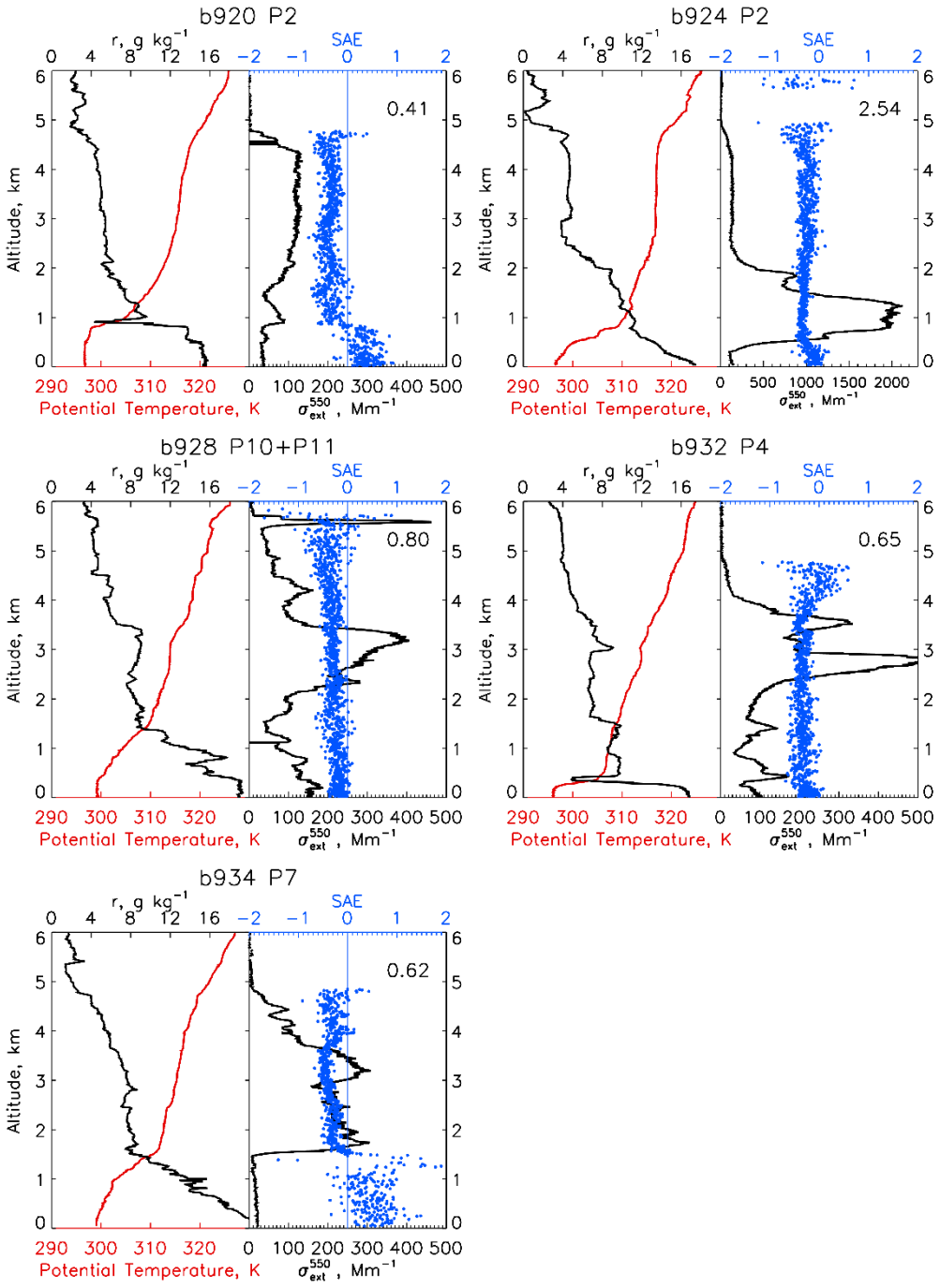

Figure 4: Vertical structure observed during the 5 flights from in-situ measurements during aircraft profiles, in the region where the SLRs were performed. Potential temperature (K; red), water vapour mixing ratio (r, g/kg, black), accumulation mode extinction (Mm^{-1}, black, note different x-axis range for b924) and scattering angstrom exponent (SAE) for the accumulation mode between 450 and 700nm (blue). Numbers at the top right of each panel indicate accumulation mode AOD at 550nm.

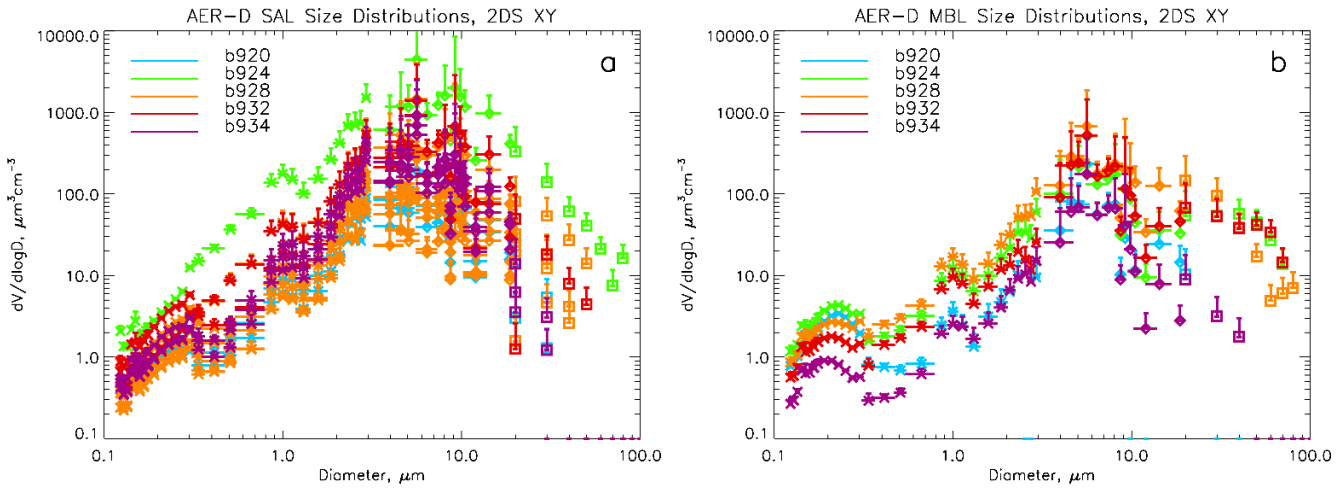

Figure 5: Size distributions for ~~legs~~ SLRs (a) in the SAL and (b) in the MBL, for the PCASP, CDP and 2DS XY. Errors combine systematic and random errors. For clarity only upper error bounds are shown. The following numbers of SLRs were performed per flight in the SAL and are shown in panel (a): b920 (2), b924 (1), b928 (6), b932 (2), b934 (3). One SLR per flight was performed in the MBL as shown in panel (b).

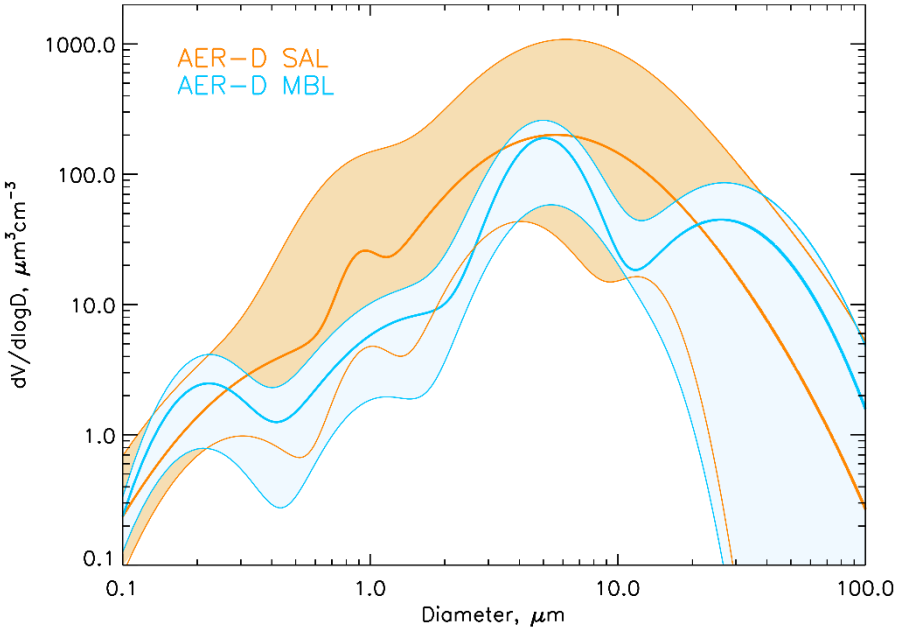

Figure 6~~(a)~~ AER-D mean logfit size distribution from the MBL (blue) and SAL (orange). Shading indicates the range between minimum to maximum values, and central solid line shows the mean.

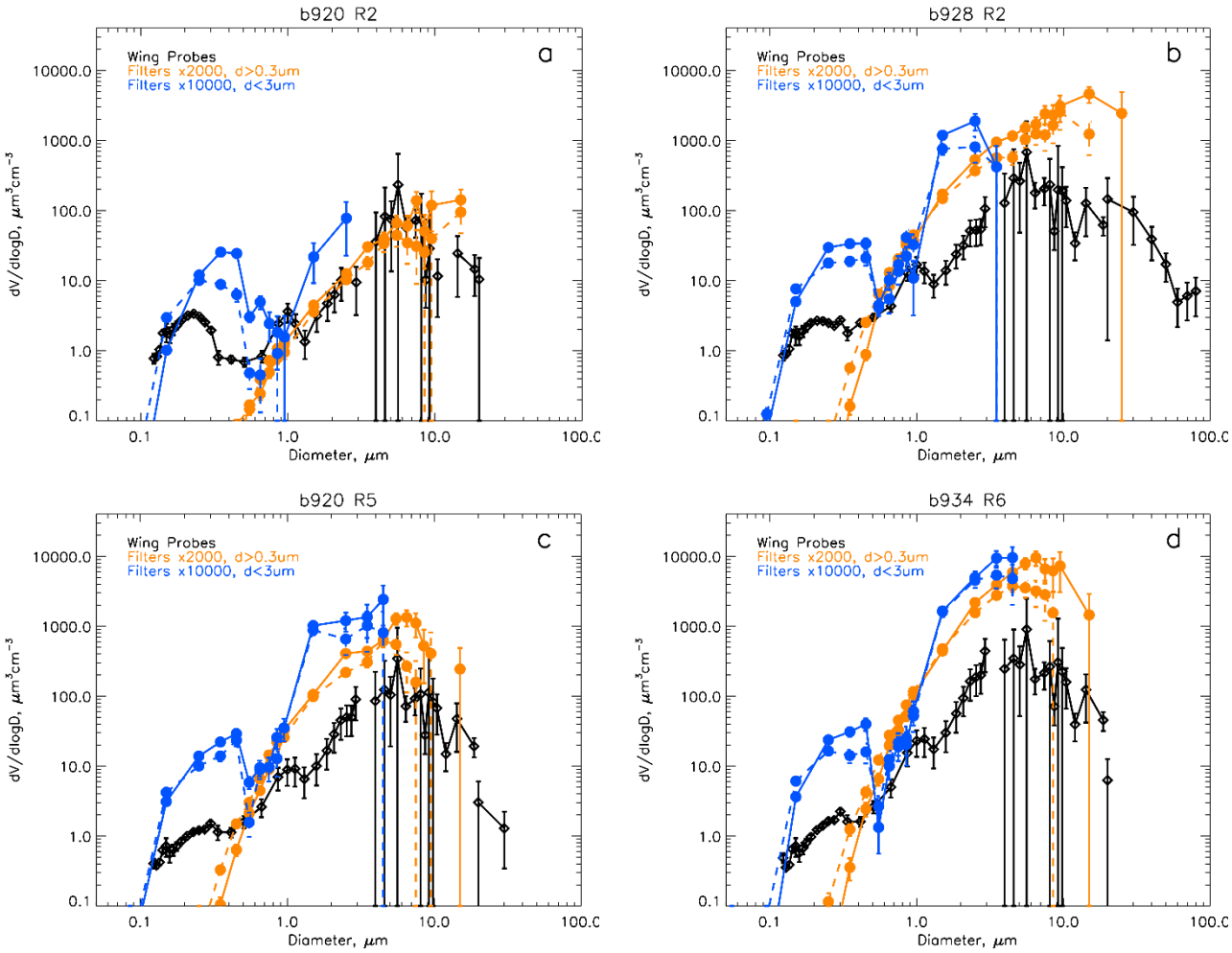

Figure 7: Comparison of wing-probe size distributions with size distributions from filter samples at 2 magnifications (2,000 and 10,000) for 4 ~~flight legs~~SLRs. (a) and (b) show PSDs in the MBL without (a) and with (b) giant mode present; (c) and (d) show PSDs in the SAL. For filter PSDs, solid lines indicate volume distribution calculated assuming spherical shape using an area-equivalent diameter. Dashed lines indicate volume distribution calculated using a height:maximum axis ratio of 1:3 (see text for more details).

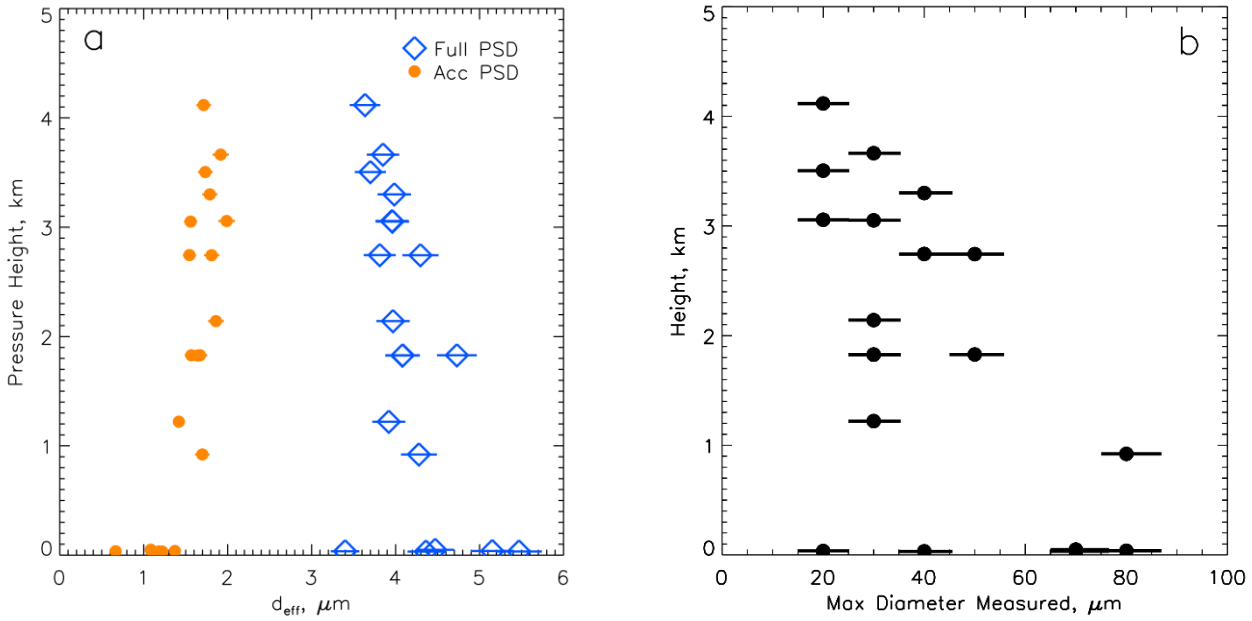

Figure 8: Variation of size with altitude for ~~flight legs~~SLRs: (a) effective diameter; (b) maximum diameter measured by the 2DS XY instrument. Orange circles represent accumulation mode only, blue diamonds represent the full PSD.

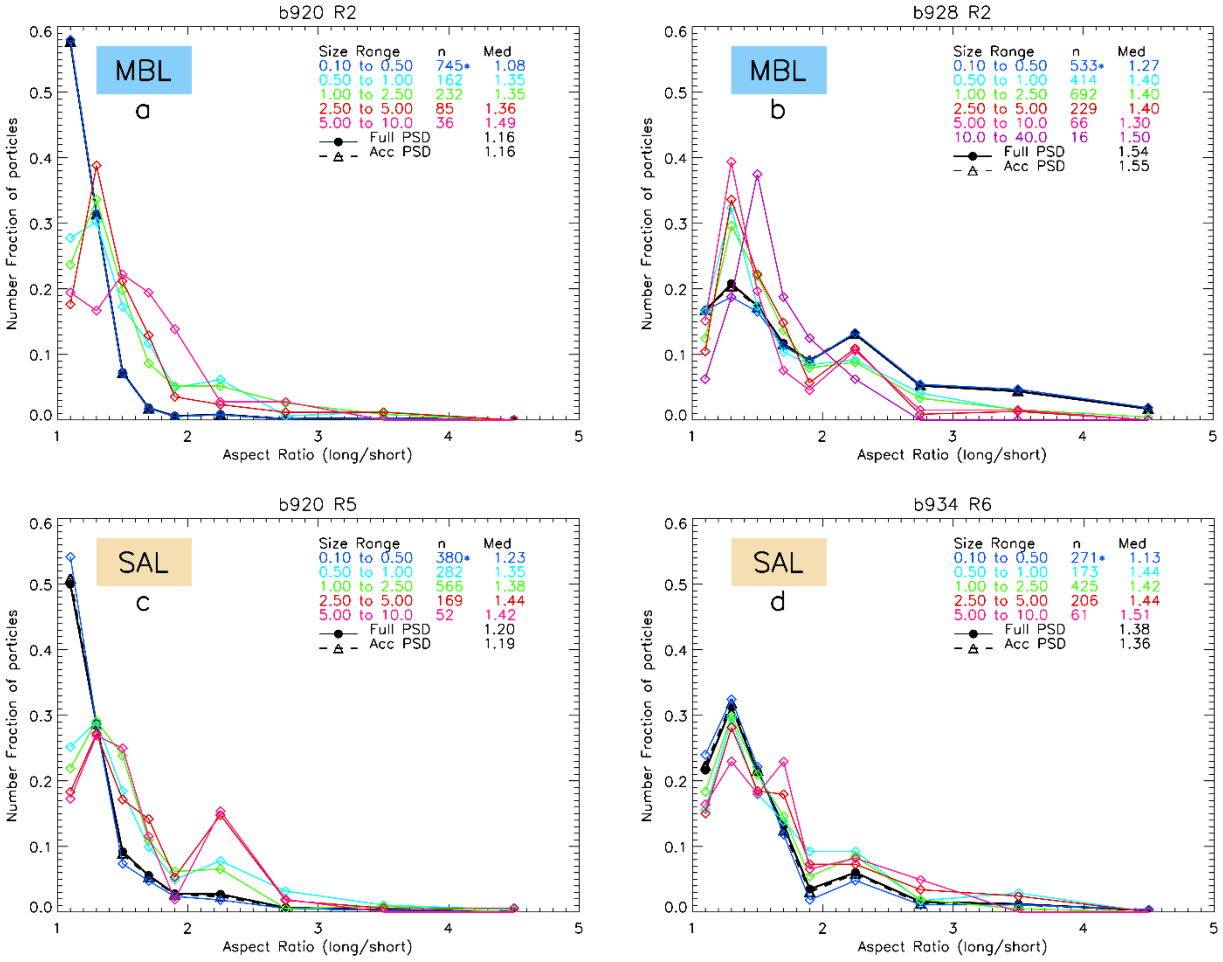

Figure 9: Number fraction of particles as a function of ~~A~~aspect ratio ~~s histograms as a function of number fraction of particles~~ from filter sample analysis for the same 4 ~~legs~~ SLRs as shown in Figure 7, as a function of size (colours), for the full PSD (0.1-40 µm, solid black), and accumulation mode PSD (0.1-2.5 µm). * indicates numbers were scaled-up from value shown to allow for different substrate areas at the higher magnification. Top row are samples from the MBL without (a) giant particles and with (b) giant particles. Bottom row are SAL samples. Data are not shown where the number of particles in a size range is under 10. In each panel the size range (microns diameter) and the associated number of particles counted and median aspect ratio are shown.

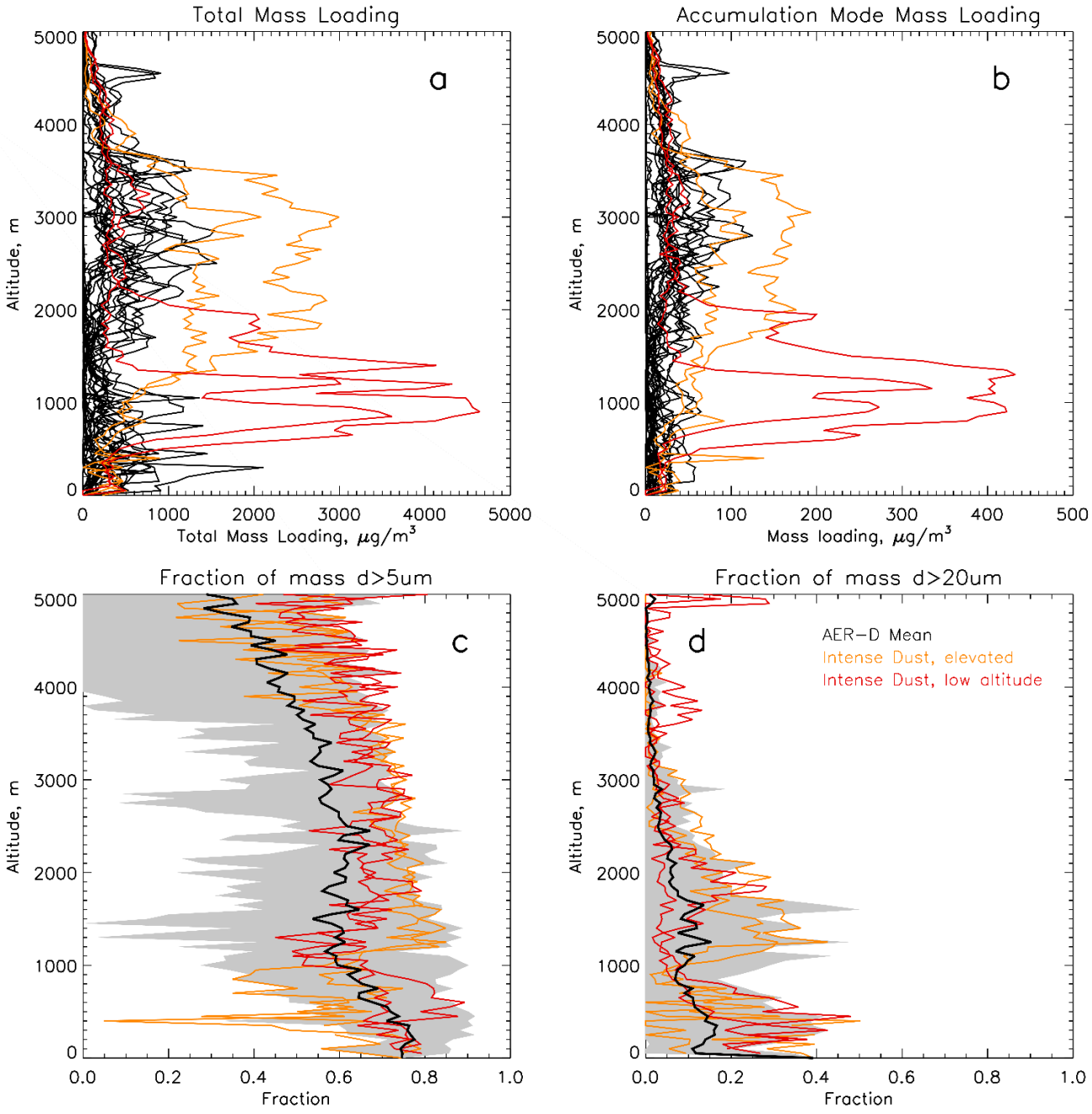

Figure 10: Profiles of aerosol mass loading calculated from in-situ size distributions assuming a dust density of 2.65gcm^{-3}. (a) Total mass loading for the full size distribution; (b) accumulation mode mass loading (d<2.5 µm); (c) Fraction of mass at sizes greater than 5 µm diameter; (d) fraction of mass at sizes greater than 20 µm diameter. Black lines in (a) and (b) represent all AER-D profiles under low-medium AODs, red/orange represent the intense dust event with AODs ~2.0 (b923/b924) separated by locations where the dust was elevated (orange) or at lower altitudes (red). In (c) and (d) grey shading represents AER-D 10th to 90th percentile range; black line represents AER-D mean. Dust Mass Path values are given in the text.

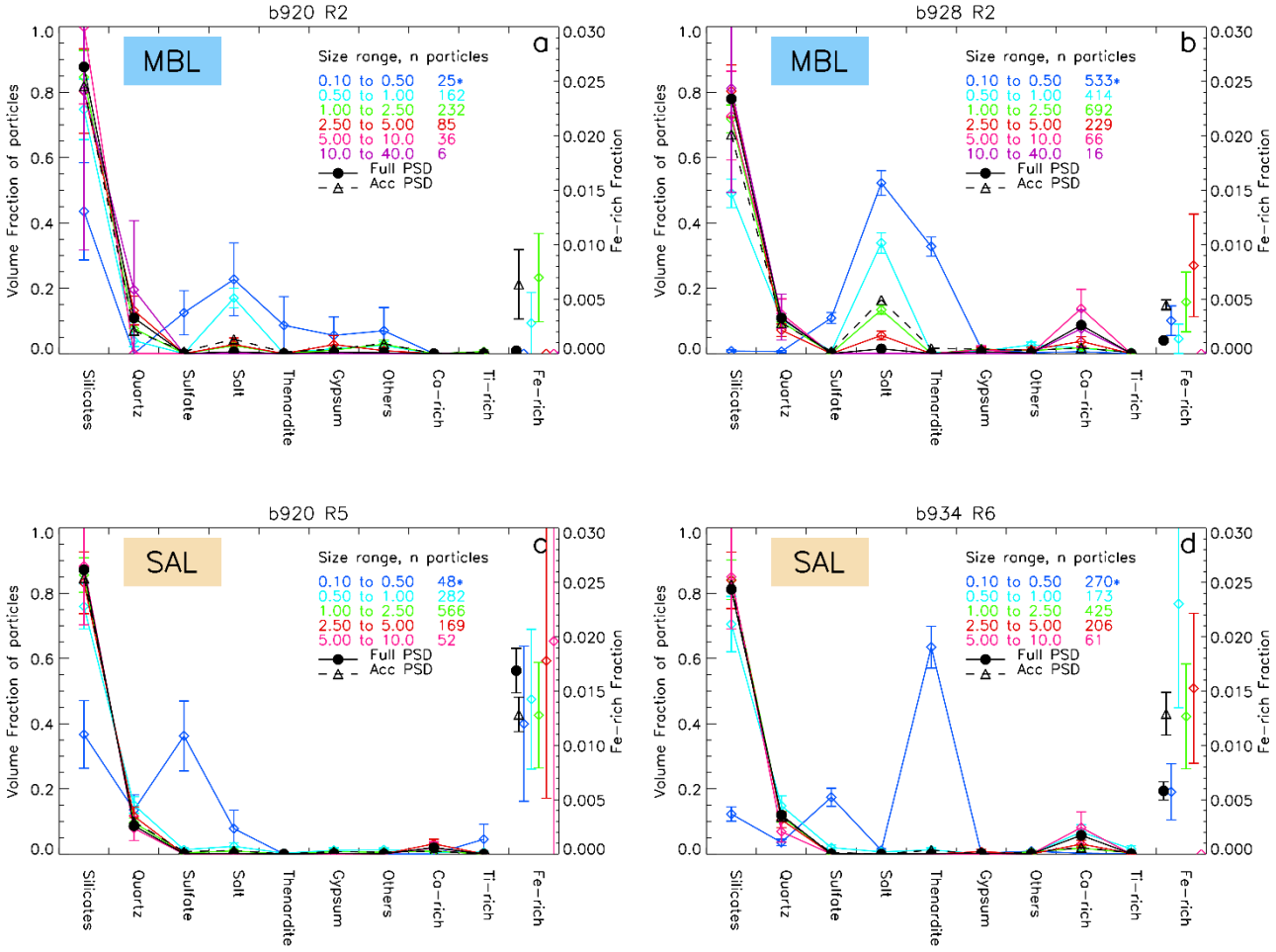

Figure 11 Composition as volume fraction from filter samples in the MBL (top panels) and SAL (bottom panels). B928 R2 (top right) contained a substantial giant mode in the MBL (e.g. see Figure 5 and Figure 7) ~~particles~~. Individual panels indicate number of particles sampled; * indicates numbers were scaled-up from value shown to allow for different substrate areas at the higher magnification. Fe-rich volume fraction is provided on the right axis with different size ranges offset. Data is also shown as bulk properties for the full PSD and accumulation mode (d<2.5 µm) and size resolved. Data is only shown when sample size is greater than 5. ~~Uncertainties~~ Error bars are counting ~~errors~~uncertainties.

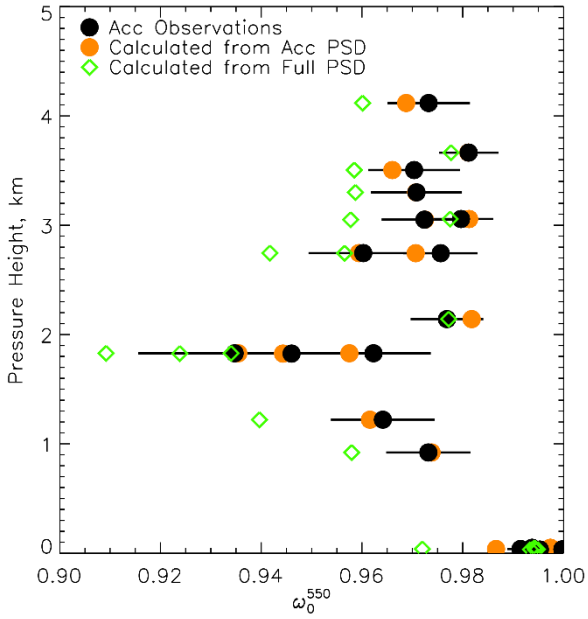

Figure 12: Variation of SSA at 550nm with altitude for ~~horizontal flight legs~~SLRs. Black circles indicate direct measurements~~, made~~ taken in-cabin behind inlets and therefore represent~~ing~~ the accumulation mode (ACC PSD~~'Acc'~~) only. Orange circles indicate calculated properties, representative of the same conditions in-cabin behind inlets for the ACC PSD. Green diamonds indicate values calculated using the 2DS-XY ~~full size distributions~~FULL PSD covering size ranges 0.1 to 200 um. Green and orange data points are from Mie calculations, black represents measurements.

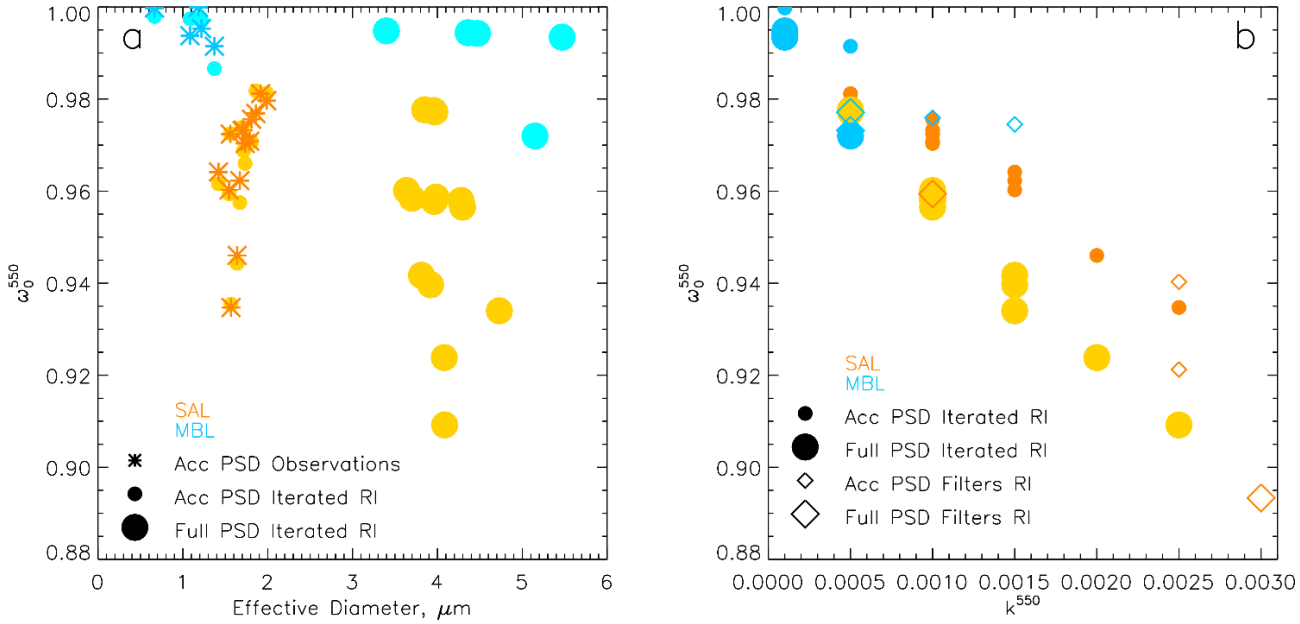

Figure 13: Contribution to single scattering albedo from particle size (a: SSA vs d_{eff} ~~vs SSA~~) and from composition (b: SSA vs k^{550} ~~vs SSA~~), separated by ~~leg~~SLRs in the SAL (orange and yellow) and MBL (blue). Small data points represent the ~~accumulation mode~~ACC PSD only, large data points represent the ~~full~~ FULL PSD. Asterixes in (a) are direct observations behind inlets. Circles represent calculations using the RI derived from Mie iterations ~~for the accumulation mode~~; diamonds represent calculations using RI derived from composition data from filter samples assuming internal mixing (4 samples). For the ~~full~~ FULL PSD with the iterated RI, the same accumulation mode RI is extended to the coarse mode. For the filters RI, size-specific RI is used for the accumulation mode and the full PSD (as given in ~~Table 6~~Table 7).

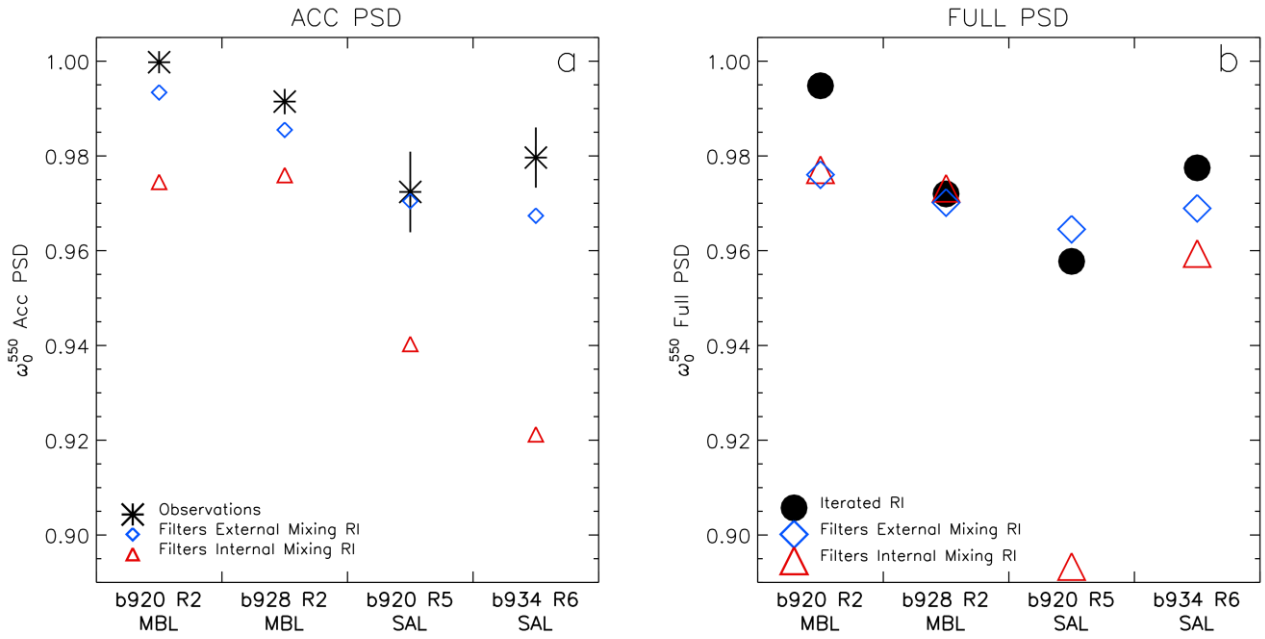

Figure 14: ~~**Comparison of SSAs for the accumulation mode, showing observations from the nephelometer and PSAP, and calculated SSA using RI derived from filter samples assuming internal and external mixing.**~~**Comparison of SSAs calculated using different RI methods for (a) the ACC PSD; (b) the FULL PSD. Observations are only available for the accumulation mode, shown in (a). SSA is calculated using RI derived from filter samples assuming internal and external mixing, or iterated RI.**